Distribution Agreement

In presenting this thesis or dissertation as a partial fulfillment of the requirements for an advanced degree from Emory University, I hereby grant to Emory University and its agents the non-exclusive license to archive, make accessible, and display my thesis or dissertation in whole or in part in all forms of media, now or hereafter known, including display on the world wide web. I understand that I may select some access restrictions as part of the online submission of this thesis or dissertation. I retain all ownership rights to the copyright of the thesis or dissertation. I also retain the right to use in future works (such as articles or books) all or part of this thesis or dissertation.

Signature:

_____ _____

Daniel Collins-Wildman Date

Dynamic Systems for Catalytic Decontamination of Chemical Warfare Agents and Photoanode Stability Studies

By

Daniel Collins-Wildman
Doctor of Philosophy

Chemistry

_____
Craig L. Hill, Ph.D.
Advisor

_____
Tianquan Lian, Ph.D.
Committee Member

_____
Cora MacBeth, Ph.D.
Committee Member

Accepted:

_____
Lisa A. Tedesco, Ph.D.
Dean of the James T. Laney School of Graduate Studies

_____
Date

Dynamic Systems for Catalytic Decontamination of Chemical Warfare Agents and Photoanode Stability Studies

By

Daniel Collins-Wildman
Master of Science, Stony Brook University, 2013

Advisor: Craig L. Hill, Ph.D.

An Abstract of
A dissertation submitted to the Faculty of the
James T. Laney School of Graduate Studies of Emory University
in partial fulfillment of the requirements for the degree of
Doctor of Philosophy
in Chemistry
2020

Abstract

Dynamic Systems for Catalytic Decontamination of Chemical Warfare Agents and Photoanode Stability Studies

By Daniel Collins-Wildman

There is increasing awareness, both scientifically and at a societal level, that anthropogenic activities are having a variety of adverse effects on our planet. There is also an understanding that these negative impacts on the environment will directly affect the quality of life for populations around the globe, and in some cases, pose direct threats to human health and safety. The scientific community is therefore invested in developing technologies to address and overcome these challenges. One of the greatest synthetically generated threats toward humans, are the highly toxic compounds known as chemical warfare agents (CWAs). Although significant efforts have been made in the development of protective materials, there remains a need for fast and truly catalytic systems to remove the two primary classes of CWAs: nerve agents and blister agents.

This dissertation describes two catalytic decontamination systems, one for each class of CWAs. Chapter 2 investigates the use of a Zr-containing polyoxometalate catalyst which effectively hydrolyzes nerve agent simulants to their non-toxic products. The nature of the buffer ions used in the system are shown to dramatically affect the rate of catalysis and speciation of the catalyst. This provides new insights for both enhancing the reactivity and brings increased awareness toward product inhibition. Chapter 3 demonstrates a fast and effective solid catalyst formulation that selectively converts the blister agent, sulfur mustard, to the decontaminated sulfoxide. In addition, this work reveals the dynamic role of copper in this system. Finally, chapter 4 investigates the stability of a photoelectrochemical film, a crucial component in addressing another major global concern, which is the ability to store energy from the sun in the form of chemical fuels.

Dynamic Systems for Catalytic Decontamination of Chemical Warfare Agents and Photoanode Stability Studies

By

Daniel Collins-Wildman
Master of Science, Stony Brook University, 2013

Advisor: Craig L. Hill, Ph.D.

A dissertation submitted to the Faculty of the
James T. Laney School of Graduate Studies of Emory University
in partial fulfillment of the requirements for the degree of
Doctor of Philosophy
in Chemistry
2020

Acknowledgments

First and foremost, I would like to thank my advisor, Dr. Craig Hill. He is a wonderful mentor and has been very generous with his time while working with me on a variety of tasks including writing effective papers and thinking critically as a scientist. My approach to research and ability to communicate results have improved markedly under his tutelage. I will use the many lessons he has taught me for years to come. I would also like to thank Dr. Yurii Geletii for everything that he has taught me, both working in the lab and navigating academia. Much of the way in which I design and conduct experiments in the lab can be attributed to Yurii. In addition, he has a wonderful sense of humor and has always been willing to discuss gardening ideas with me. I would like to thank my two committee members, Dr. Tim Lian and Dr. Cora MacBeth, for their help in honing my skills as a scientist/researcher. I will always appreciate their insightful questions during my annual reports that, while challenging, pushed me to be more thorough and clarify my goals when conducting and presenting my research.

Within the Hill lab there are many people to thank, but along with the scientific lessons I have learned, I want to thank all of them for their kindness and collaborative spirit. I must first thank Dr. Kevin Sullivan. He has been a very dear friend for 12 years now, and I can't wait for our next adventure together. I would also like to thank Ben Yin for being a great training partner and for the many entertaining philosophical discussions that I will miss when I leave. Many thanks to Dr. Elliot Glass and Dr. Jim Vickers for taking me under their wing when I first arrived. I would also like to acknowledge the many other Hill lab members who I appreciated the opportunity to collaborate with: Dr. Sarah Wilkening, Dr. Mooeung Kim, Dr. Marika Wieliczko, Dr. Weiwei Guo, Dr. Hongjin Lv, Yimu Hu, Phillip Zhu, Torie Snider, Xinlin Lu, Ting Cheng, Dr. Masoumeh Chamack, and Natalie Uhlikova. Thank you to Otgoo Altangerel for her hard work as an undergraduate under my instruction.

One of the greatest parts of my time at Emory has been participating the Multi-RAD team collaboration. I would like to thank all the PIs in the group: Dr. John Morris, Dr. Anatoly Frenkel, Dr. Jamal Musaev, Dr. Diego Troya, Dr. Mark Mitchell, and Dr. Wesley Gordon. I would also like to thank Yiyao Tian for all her time processing and discussing data with me. Thank you to the Defense Threat Reduction Agency and the Army Research Office for providing me with funding throughout much of my time at Emory.

Finally, thank you to my family and friends. Thank you to both of my extraordinary parents who are the foundation on which my ability to get through the hard times is built. Thank you to my sister, Elizabeth Collins-Wildman, who has always been an inspiration to me. Thank you to Jen Shriber for being there through it all by pushing me to keep the ball rolling while still having fun adventures on the weekends. I'm looking forward to this next one. Thank you to Greg Vansuch and Roger Park for giving me many much-needed laughs. Thank you to Michael Dugan, Dr. Jeff Schreiber, Jay Schwartz, Alisina Bazrafshan, Brendan Deal, Sean Bresler, Hallie Andrews, Ashley Coenen, Nicky Deak, Forrest Deak, and many others for their friendship and support. I could not have done this without you.

Table of Contents

List of Figures

List of Schemes

List of Tables

List of Abbreviations

AChE	acetylcholinesterase
ALD	atomic layer deposition
BE	bulk electrolysis
CdS-QD	cadmium sulfide quantum dot
CEES	2-chloroethyl ethyl sulfide
CEESO	2-chloroethyl ethyl sulfoxide
CEESO2	2-chloroethyl ethyl sulfone
CV	cyclic voltammogram
CWA	chemical warfare agent
DCB	dichlorobenzene
DFT	density functional theory
DMMP	dimethyl methylphosphonate
DMNP	O,O-dimethyl O-(4-nitrophenyl) phosphate
DMP	dimethyl phosphate
DOSY	diffusion-ordered spectroscopy
DRIFTS	diffuse reflectance infrared Fourier transform spectroscopy
DSSC	dye-sensitized solar cells
EXAFS	extended X-ray absorption fine structure
FFT	fast Fourier transform
FID	flame ionization detector
FTIR	Fourier transform infrared
GB	sarin

GC	gas chromatography
GC-MS	gas chromatography-mass spectrometry
G-type	German-type
HD	bis(2-chloroethyl) sulfide (sulfur mustard)
HP	Hewlett Packard
Hz	hertz
IEF-PCM	integral equation formalism-polarizable continuum model
IFEFFIT	library of XAFS algorithms
IR	infrared
LMCT	ligand-to-metal charge transfer
MCT	mercury cadmium telluride
MeCN	acetonitrile
MOF	metal organic framework
MPA	methyl phosphonic acid
NEM	N-ethylmorpholine
NMR	nuclear magnetic resonance
NSLS	national synchrotron light source
OCP	open circuit potential
OP	organophosphorus
POM	polyoxometalate
ppm	parts per million
PTFE	polytetrafluoroethylene
PZC	point of zero charge

QAS	quick X-ray absorption and scattering
QD	quantum dot
RH	relative humidity
SBU	secondary building unit
SFC	solid formulation catalyst
TBA	tetrabutylammonium
TMA	tetramethylammonium
TW	terawatt
UV-vis	ultraviolet-visible
V-type	venomous-type
WOC	water oxidation catalyst
WWI	World War I
XAFS	X-ray absorption fine structure
XANES	X-ray absorption near edge structure

Chapter 1: Introduction – History and Overview of Chemical Warfare Agent Decontamination

1.1 History of Chemical Warfare

Throughout the course of human history, we have sadly used our understanding of the natural world to develop tools to inflict harm on one another. This began with the design of objects for implementing physical trauma, and over time, through advances in science and technology, led to the development of synthetic compounds with incredibly high toxicity. Today, these compounds that are specifically designed for war are known as chemical warfare agents (CWAs). One of the earliest historical records of chemical agents being used for warfare comes out of the Indian epic *Ramayana*, which describes the use of poisoned arrows around 2000 B.C.E.[1] Archeologists recently found the first physical evidence of ancient chemical warfare where Sassanian forces generated sulfur dioxide to kill 18 Roman soldiers in 256 C.E.[2] During the 19th century the industrial revolution dramatically changed the scale on which toxic chemicals such as chlorine could be manufactured and dispersed on an enemy force. This made world leaders increasingly concerned over the threat of chemical agents being used in warfare. In response to these rising fears many countries signed and ratified a declaration against the use of asphyxiating gases at the 1899 International Peace Conference at the Hague. Interestingly, the United States did not choose to sign.[3]

Despite the best intentions of world leaders in 1899, World War I (WWI) saw the largest deployment of chemical warfare the world has ever seen.[4] The use of chemical agents such as chlorine, phosgene, and sulfur mustard, caused around 100,000 deaths and over 1 million soldier and civilian casualties. Following the war, the world again sought to limit the use of chemical warfare by ratifying the 1925 Geneva Protocol for the Prohibition of the Use in War of Asphyxiating, Poisonous or other Gases, and of Bacteriological Methods of Warfare.[5] Many countries, including the United States, chose to reserve the right to retaliate and did not sign the

treaty until many years later. The United States waited until 1975 to ratify the Geneva Protocol.[6] As a result, chemical warfare agent research continued leading into World War II.[6] During the late 1930s these continued research efforts led German scientists to development the organophosphorus nerve agents, which are considered to be "the most nefarious of synthetic chemical derivatives."[7] While chemical weapons were not deployed in the way that they were during WWI, many nations began stockpiling weapons in preparation to retaliate against potential foreign threats.[5]

Throughout the latter half of the twentieth century there were a number of incidents where chemical warfare agents were used. In 1988 the worst single attack occurred in Halabja, Iraq resulting in at least 5000 deaths most of whom were civilians.[8] In 1993 once again countries around the world came together and signed the Chemical Weapons Convention treaty which prohibited use and production of chemical weapons and mandated the destruction of chemical weapon stockpiles. While this treaty, ratified in 1997, has proved incredibly effective resulting in a 97.5% decrease in global stockpiles to date,[9] the use of chemical warfare agents has unfortunately continued with the 2013 Sarin attack in Damascus, Syria[10] and mostly recently the poisoning of Alexey Navalny[11] among others. The persistence of CWA threats is in part due to the fact that these compounds are relatively simple to produce and therefore readily accessible to those with malicious intent. As a result, treaties alone cannot prevent the use of CWAs and therefore it is the responsibility of the scientific community to develop protective measures to counteract the existing threats. For this reason, there remains great interest in researching and developing protective and decontaminating materials.[7, 12-17]

These protective materials generally neutralize the threat of exposure via one of two distinct pathways. The simplest method is to generate a material to which CWAs will strongly

adsorb. During WWI activated carbon was found to work remarkably well for this purpose and has successfully been used to remove gaseous CWAs through filters in gas masks.[13] Adsorption materials have also been implemented in protective garments. The obvious downside to this approach is that the agent is still intact and active, and thus the filtration media must be disposed of with care.[18] In addition, over time the open sites for physisorption can become saturated lowering the effectiveness of the filter. While there is still some active research in the area of adsorptive materials,[19-21] this work will focus on the more direct approach of chemically converting CWAs into non-toxic forms. The chemistry involved in these processes is informed by the properties of the specific agent(s) to be decontaminated.

1.2 Nerve Agents

The most toxic class of chemical warfare agents are referred to as nerve agents. Their extreme toxicity arises from the ability of these organophosphorus (OP) compounds to dramatically inhibit the activity of the enzyme acetylcholinesterase (AChE).[7] Figure 1.1 shows the structures of some of the most common G-type (German-type for the early agents developed in Germany) and V-type (Venomous-type) agents based on their order of discovery. Each of these compounds shuts down the activity of AChE by irreversibly binding to the active site. In the body, AChE is responsible for catalyzing hydrolysis of the neurotransmitter acetylcholine to choline. This process occurs extremely rapidly with a turnover frequency for AChE of greater than 10^4 s^{-1}.[22] Maintaining proper levels of choline and acetylcholine is critical for allowing proper nerve function. Upon inhibiting the activity of AChE, there is a rapid buildup of acetylcholine causing uncontrolled muscle contraction which can lead to death by asphyxiation.[23]

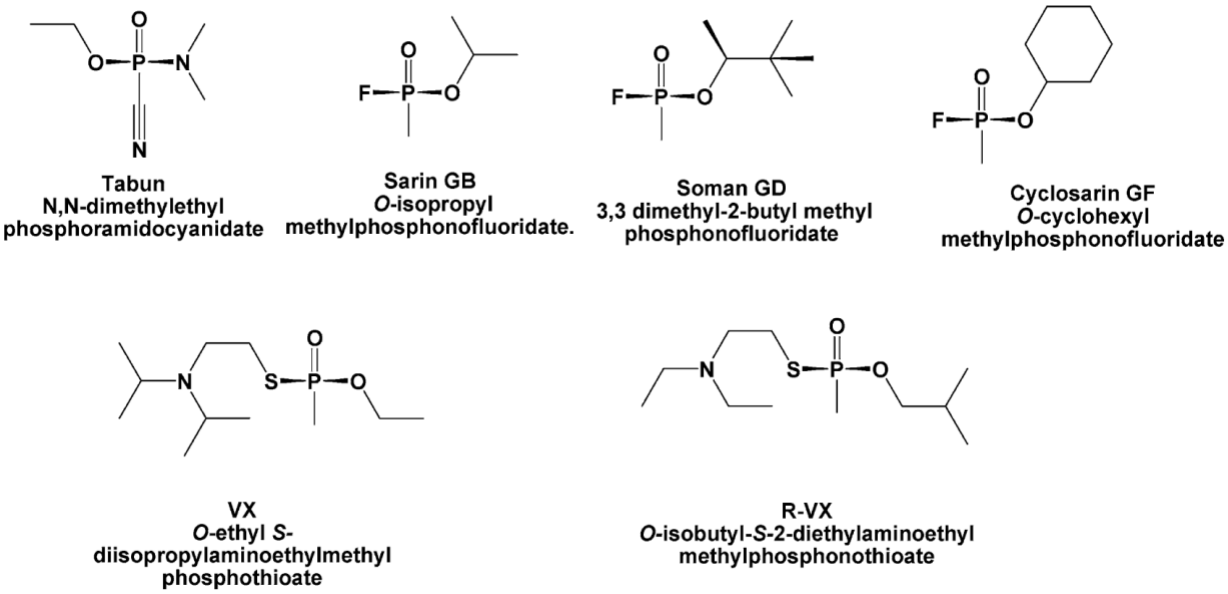

Figure 1.1. The structures and names (common and IUPAC) for G and V-type agents in the order of their discovery. Reprinted with permission from Jang, Y. J.; Kim, K.; Tsay, O. G.; Atwood, D. A.; Churchill, D. G., Update 1 of: Destruction and Detection of Chemical Warfare Agents. *Chem. Rev.* **2015,** *115* (24), PR1-PR76. Copyright (2015) American Chemical Society.

Since the discovery of nerve agents, a variety of methods have been explored for both the disposal/decontamination of these materials. Prior to the Chemical Weapons Convention, chemical weapons munitions were often dumped into the sea. In 1969 the United States thankfully officially abandoned this practice and turned to more rigorously controlled methods.[7] These include incineration with multi-stage burners and hydrolysis in the presence of excess sodium hydroxide.[24] Further methods, such as treatment with hydrogen peroxide, alkoxides, and various halogen containing species such as hypochlorite and hypobromite are all effective decontamination strategies.[25-28] The downside of these systems is that they all employ stoichiometric reagents requiring more material per equivalent of CWA than that of a catalytic system. In addition, many of these compounds are themselves toxic and corrosive making them

incompatible for use in protective equipment such as air filters and protective garments. Further, disposal of these stoichiometric decontaminating agents can be environmentally undesirable. Therefore, the development of a catalytic materials that can be implemented in personal protective equipment is of great interest.

Transition metal-based hydrolysis catalysts including Cu^{2+}, UO_2^{2+}, La^{3+}, VO^{2+}, Fe^{3+}, MoO_2^{2+}, Zr^{4+}, Ti^{4+}, Zn^{2+} among others, show promising nerve agent decontamination activity and fit the above criteria.[29, 30] Figure 1.2 shows the proposed mechanism by which metal centers enhance the rate of reactivity. The first step involves coordination of the OP to the metal center. The low charge density on the metal pulls electron density through oxygen away from the OP phosphorus making it more susceptible to nucleophilic attack. Next, either an aqua ligand bound to the same metal or an adjacent metal acts as the nucleophile and attacks the OP. This is followed by the release of a fluoride for most nerve agents and, in this example, methoxide from dimethyl methyl phosphonate.

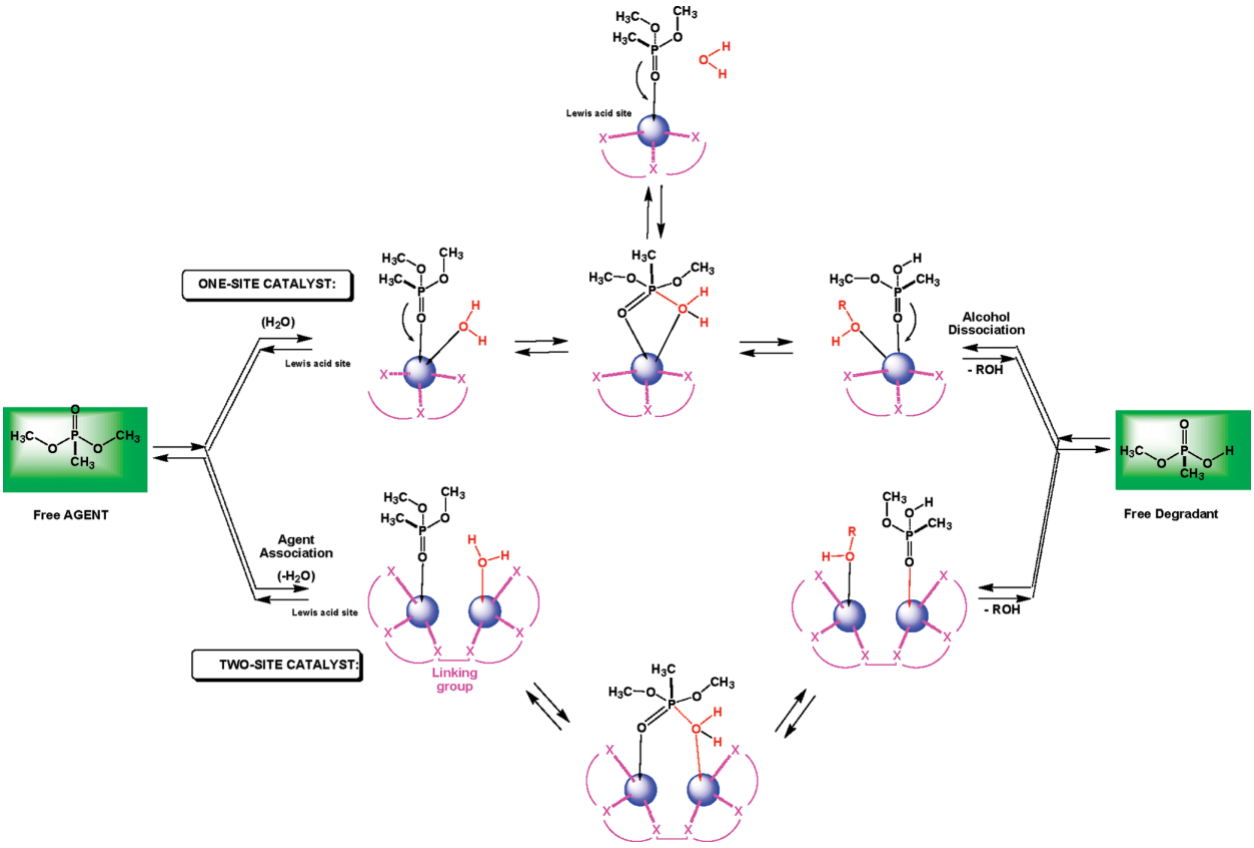

Figure 1.2. Proposed mechanism nerve agent hydrolysis catalyzed by one and two-site metal-based catalysts. This scheme portrays the hydrolysis of the CWA simulant dimethyl methylphosphonate (DMMP). Reprinted with permission from Jang, Y. J.; Kim, K.; Tsay, O. G.; Atwood, D. A.; Churchill, D. G., Update 1 of: Destruction and Detection of Chemical Warfare Agents. *Chem. Rev.* **2015,** *115* (24), PR1-PR76. Copyright (2015) American Chemical Society.

In recent years zirconium containing materials, including metal organic frameworks (MOFs) and amorphous zirconium hydroxide, have garnered significant attention.[13, 31-37] While these materials achieve rapid hydrolysis rates, they suffer from significant product inhibition. The phosphonate hydrolysis product remains strongly bound to the Zr metal centers thus shutting down further catalytic activity (Figure 1.3).[38, 39] There is accordingly great interest in both

investigating the nature of this inhibition and studying methods for addressing it. Chapter 2 explores nerve agent simulant hydrolysis catalyzed by a Zr-containing polyoxometalate and how the system is affected by product inhibition.

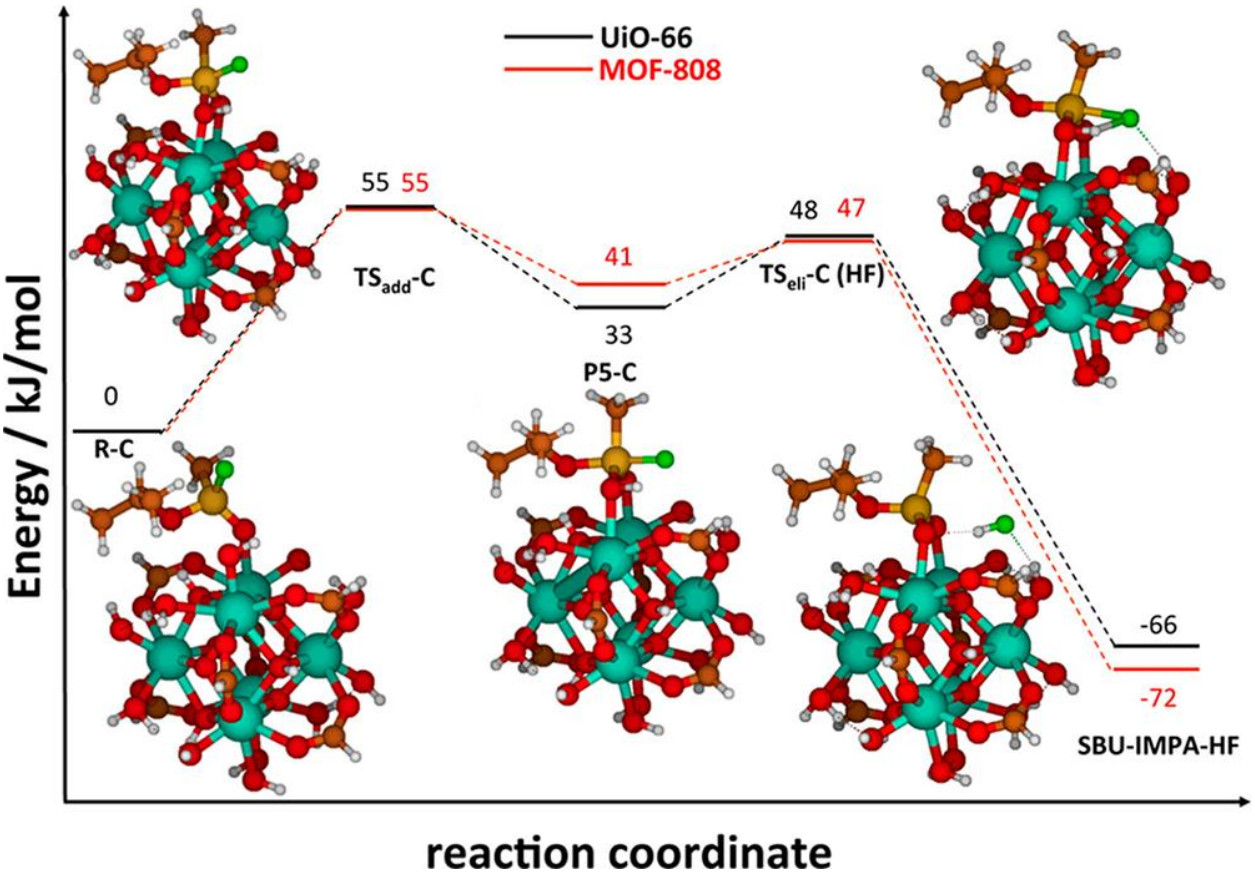

Figure 1.3. The reaction mechanism for hydrolysis of the nerve agent, sarin (GB), catalyzed by Zr-containing MOFs along with potential energies associated with each of the transition states along the reaction coordinate. The black and red curves correspond to energies associated with reactivity with the secondary building units (SBUs) of UiO-66 and MOF-808 respectively. Both of these materials show a deep potential energy well associated with the bidentate bound GB hydrolysis product indicative of product inhibition. Reprinted with permission from Troya, D.,

Reaction Mechanism of Nerve-Agent Decomposition with Zr-Based Metal Organic Frameworks. *J. Phys. Chem. C* **2016,** *120* (51), 29312-29323. Copyright (2016) American Chemical Society.

1.3 HD Sulfur Mustard

One of the highest tonnage chemical warfare agents based on global stockpiles is sulfur mustard, making the decontamination of this specific agent a high priority.[5] Sulfur mustard, bis(2-chloroethyl)sulfide, also known as HD or more commonly mustard gas, is a blister agent with substantially different properties than the nerve agents described previously. Blister agents are vesicants that are both carcinogenic and mutagenic given their strong alkylating ability.[40] In the case of HD, the toxicity is due to the reactivity of a cyclic sulfonium chloride that is in equilibrium with HD.[41] This intermediate forms via an intramolecular nucleophilic attack by the sulfur center cleaving the C-Cl bond and forming the cyclic ethylene sulfonium ion. It then readily alkylates DNA leading to the mutagenic properties of HD (Figure 1.4).[42-44]

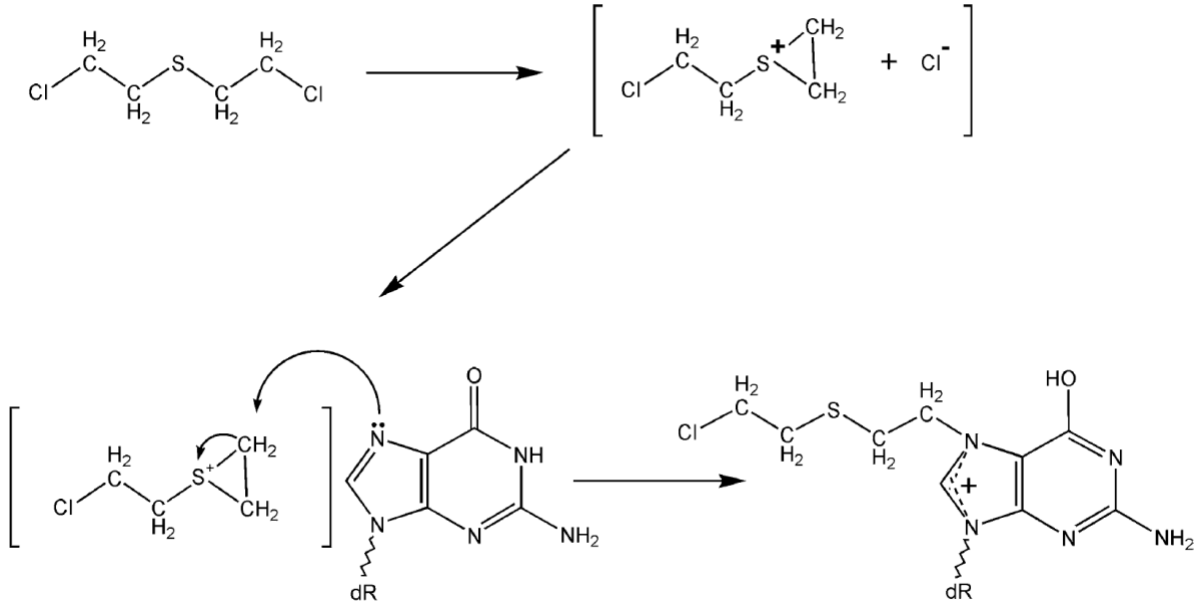

Figure 1.4. The mechanism of DNA alkylation by HD. Initially HD is converted to the ethylene sulfonium complex the via an intramolecular cyclization reaction releasing chloride. This reactive intermediate is then susceptible to attack by nucleophiles such 2-deoxyguanosine as shown. The remaining chloroethyl group can then undergo a similar reaction crosslinking DNA bases or other structures within the cell. Reprinted with permission from Shakarjian, M. P.; Heck, D. E.; Gray, J. P.; Sinko, P. J.; Gordon, M. K.; Casillas, R. P.; Heindel, N. D.; Gerecke, D. R.; Laskin, D. L.; Laskin, J. D., Mechanisms Mediating the Vesicant Actions of Sulfur Mustard after Cutaneous Exposure. *Toxicol. Sci.* **2009,** *114* (1), 5-19. Copyright (2009) Oxford University Press.

By preventing this intermediate from forming, the toxicity of HD can be eliminated. This can be achieved either by oxidation of the sulfur center or by hydrolysis, replacing the chloroethyl with hydroxyethyl groups.[14, 15, 45] While a number of studies have explored hydrolysis reactions, the hydrophobic nature of HD limits this reaction to the interface between phases and consequently proceeds very slowly.[45] As a result, significant effort has been focused

on exploring methods to selectively oxidize the sulfur center.[14, 15, 45-49] Selectivity is critical as the overoxidation product, the sulfone, has significant toxicity.[50] Bis(2-chloroethyl)sulfone rapidly undergoes elimination of HCl to form the divinyl sulfone. The vinyl groups are reactive toward nucleophiles enabling this compound to bind/crosslink DNA and proteins similarly to the sulfonium intermediate.[40] While there are many systems capable of sulfide oxidation most require the use of a stoichiometric oxidants such as hydrogen peroxide or bleach. Truly catalytic systems that utilize air-based oxygen as the oxidant, while retaining a high degree of selectivity for the sulfoxide are therefore ideal candidates for HD decontamination. Chapter 3 explores such a catalytic system which promotes selective aerobic sulfoxidation of HD.

1.4 Polyoxometalates in Decontamination Catalysis

Polyoxometalates (POMs) comprise a group of molecular, metal oxygen anions that have been explored in a wide variety of chemical applications including medicine, catalysis, and materials science.[51-54] This great diversity of application stems from the unique characteristics of POMs including oxidative and thermal stability, in addition to highly tunable physical properties such as redox potential, acidity, size, charge, and solubility in a myriad of solvents.[53] Some of the most common POM structures are shown in Figure 1.5 where each octahedron represents a single metalate, MO_6^{n-} unit. The typical metals found in POMs are V, Mo, W, Nb and Ta. These polyanionic metal-oxide-like clusters can be further modified to generate lacunary structures by removing one or more of the metal centers creating stable compounds that can then coordinate additional transition metals.[51] All told, there are known POMs structures containing a majority of the elements in the periodic table enabling the rational design of catalysts for a wide variety of applications.[53]

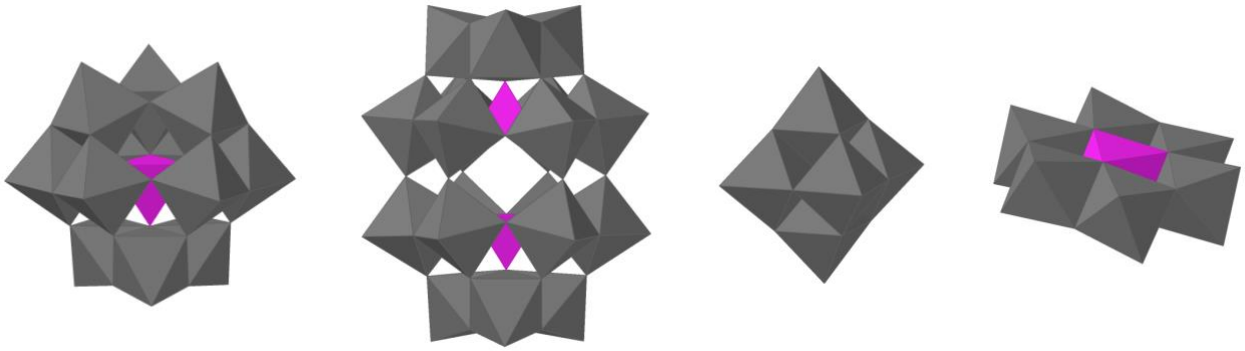

Figure 1.5. Common POM structures. From left to right: Keggin, Wells-Dawson, Lindqvist, and Anderson. Grey octahedra represent MO_6 units where M is V, Mo, W, Nb, or Ta; fuchsia tetrahedra represent XO_4 units where X is most commonly Al, Si, or P.

Many groups have successfully utilized these highly modular properties of POMs for the decontamination of chemical warfare agents. The two classes of chemical warfare agents are generally detoxified via different pathways; hydrolysis for organophosphate nerve agents, and oxidation for sulfide/amine-based blister agents. This results in certain materials being optimized often for one type of agent or the other. For nerve agents, a wide variety of POMs were shown to catalyze hydrolysis including polymolybdates, polyniobates, and polytungstates.[55-60] For these reactions, the electron-rich oxygen centers, as shown via density functional theory calculations on $Cs_8Nb_6O_{19}$,[57] help the POM to act as a general base catalyst. Other studies report enhanced hydrolysis rates by incorporating Lewis acidic centers such as zinc and zirconium, similar to those found in MOFs, either as counter cations or as a part of the POM framework.[61-64] In these systems, the Lewis acid sites activate the phosphorus-oxygen bond, or in some cases phosphorus-sulfur double bond, making the nerve agent more susceptible to nucleophilic attack by water or hydroxide.[7]

On the oxidative side, POMs are well known to catalyze sulfide oxidations in the presence of hydrogen peroxide.[54] While chapter 3 of this work does not utilize a POM-containing catalyst for HD sulfoxidation, a brief description of some POM-based systems are included below for completeness. Several groups have used polymolybdates, polyniobates, and polytungstates in the presence of H_2O_2 to oxidize both sulfur mustard (HD) and its simulant 2-chloroethylethyl sulfide (CEES).[55, 56, 58, 63-68] Further, Buru et. al. incorporated $H_3PW_{12}O_{40}$ into the pores of the MOF NU-1000 creating a heterogeneous POM-MOF material for catalytic sulfoxidation.[69] In an effort to avoid the use of hydrogen peroxide, Hill et. al. explored POM catalyzed oxidation using air-based oxygen to drive the reaction.[46, 70] Finally, given the significant degree of overlap between POMs used for catalyzing both sulfide oxidation and organophosphate hydrolysis, a number of studies have also successfully demonstrated activity with a single material for both reactions.[55, 56, 58, 63, 64] While POMs show some promise in catalytic sulfoxidation, the reactions rates are substantially slower than the catalytic system described in Chapter 3 based on tribromide, nitrate, copper, and acid. The latter system appears to be the fastest aerobic sulfoxidation catalyst known to date.

1.5 Scope of the Current Work

Given the responsibility the scientific community bears for researching and developing chemical warfare agents historically, the responsibility to develop countermeasures must fall to the same community. Many groups have made substantial contributions to this field, however, there remains a need for fast and truly catalytic materials for the decontamination of both nerve agents and blister agents. This dissertation explores two catalytic systems, one for hydrolysis of nerve agents, and another for selective aerobic oxidation of HD to the decontaminated sulfoxide form. An interesting common theme that arises in both of these systems is the dynamic nature of

the catalysts. In both cases there are reversible processes whose equilibrium can be shifted to improve catalytic activity.

Chapter 2 explores how the Zr-containing polyoxometalate (POM), $(Et_2NH_2)_8[\{\alpha\text{-}PW_{11}O_{39}Zr(\mu\text{-}OH)(H_2O)\}_2]\cdot 7H_2O$ (**1**), effectively catalyzes the hydrolysis of nerve agent simulants at near neutral pH. Analogous Zr-containing heterogeneous systems, are much-studied and effective nerve agent hydrolysis catalysts, but due to their heterogeneous nature, it is very challenging to know the exact structure of the catalytic sites during turnover and to clarify at the molecular level the elementary mechanistic processes. Here, under homogeneous conditions, hydrolysis rates of the nerve agent simulant methyl paraoxon catalyzed by **1** are examined as a function of pH, ionic strength, catalyst, and substrate concentrations. In addition, the specific effect of three commonly used buffers is examined revealing that acetate functions as a co-catalyst, phosphate inhibits of hydrolytic activity, and 2-(*N*-morpholino)ethanesulfonic acid (MES) has no effect on the hydrolysis rate. Spectroscopic (^{31}P NMR) and computational studies demonstrate how each of these buffers interacts with the catalyst and offer explanations of their impacts on the hydrolysis rates. The impact of the nerve agent hydrolysis product, methyl phosphonic acid, is also examined, and it is shown to inhibit hydrolysis. These results will aid in the design of future Zr-based hydrolysis catalysts.

Chapter 3 reports the development of a solvent-free, solid, robust catalyst comprising hydrophobic salts of tribromide and nitrate, $Cu(NO_3)_2\bullet 3H_2O$ (Cu(II)) and a solid acid (Nafion^{TM}) for selective sulfoxidation using only ambient air at room temperature. This system is capable of rapid decontamination of sulfur mustard (HD) either as a neat liquid or a vapor. The mechanisms of these aerobic decontamination reactions are complex; studies confirm the reversible formation of a key reaction intermediate, the bromosulfonium ion, and that the role of

Cu(II), unlike other 3d metals, in increasing the turnover rate four-fold is its ability to increase the equilibrium concentration of bromosulfonium during catalysis. Cu(II) also provides a dynamic colorimetric detection capability (in the absence of HD or sulfides, the solid is light green; in their presence, it is dark brown). Bromine K-edge XANES and EXAFS studies confirm the regeneration of tribromide under catalytic conditions. Diffuse reflectance infrared Fourier transform spectroscopy (DRIFTS) shows absorption of live agent HD vapor along with selective conversion to the desired sulfoxide product, HDO, at the gas-solid interface.

Although the primary focus of this dissertation regards the development of catalytic systems for decontamination of chemical warfare agents, additional studies are included in Chapter 4 outlining work toward addressing another key global concern: the development of catalysts for generating solar fuels. While these experiments did not lead to a publication, the collaborations that were established and the general approach of utilizing atomic layer depositing in conjunction with molecular water oxidation catalysts, were instrumental in setting the stage for subsequent Hill Lab studies published in ACS Applied Materials & Interfaces.[71]

Development of carbon-emission-free or carbon-neutral energy sources is one of the most important challenges of the 21st century. Light-driven water splitting to generate hydrogen fuel is an effective solution to this problem. This work explores utilizing conformal metal oxide coatings for the purpose of both protecting delicate semiconductor light absorbers from photocorrosion, as well as providing a novel way of a binding a molecular water oxidation catalyst (WOC) to the surface. The WOC, $[\{RuIV_4(OH)_2(H_2O)_4\}(\gamma\text{-}SiW_{10}O_{34})_2]^{10-}$, is effectively immobilized on TiO_2 nanoparticles by pH adjustment of the solution demonstrating viability of this new binding method. Atomic layer deposition is used to grow metal oxide films of 2, 5, 10, and 50 nm over cadmium sulfide quantum dot (CdS-QD) films. UV-vis

measurements show that a 50 nm coating of TiO_2 successfully stabilizes the CdS-QD film against photocorrosion. The system is limited, however, by the marked insulating effect of the 50 nm thick metal oxide layer. While this layer stabilizes the films, it simultaneously inhibits effective electron transfer across this interface. Nonetheless, future studies will benefit from the knowledge of how to avoid damaging QD films both from heat, during ALD treatment, and photocorrosion. In addition, this newly reported method for immobilizing POMs on metal oxide surfaces will also be beneficial for future work.

1.6 References

1. Kokatnur, V. R., Chemical warfare in Ancient India. *J. Chem. Educ.* **1948,** *25* (5), 268.

2. Afshari, R., Use of Chemical Warfare Agents in Ancient History. A Case of Persians and Romans in Dura-Europos, Modern Syria in 256 CE. *Asia Pacific Journal of Medical Toxicology* **2018,** *7* (3), 54-59.

3. Levie, H. S., A Lookback at the Efforts to Eliminate Chemical Warfare. *Mil. L. & L. War Rev.* **1990,** *29*, 289-290.

4. Ganesan, K.; Raza, S.; Vijayaraghavan, R., Chemical warfare agents. *Journal of pharmacy and bioallied sciences* **2010,** *2* (3), 166.

5. Black, R., CHAPTER 1 Development, Historical Use and Properties of Chemical Warfare Agents. In *Chemical Warfare Toxicology: Volume 1: Fundamental Aspects*, The Royal Society of Chemistry: 2016; Vol. 1, pp 1-28.

6. Malloy, C. D., A History of Biological and Chemical Warfare and Terrorism. *Journal of Public Health Management and Practice* **2000,** *6* (4), 30-37.

7. Jang, Y. J.; Kim, K.; Tsay, O. G.; Atwood, D. A.; Churchill, D. G., Update 1 of: Destruction and Detection of Chemical Warfare Agents. *Chem. Rev.* **2015,** *115* (24), PR1-PR76.

8. Al-Doski, J.; Mansor, S. B.; Shafri, H. Z. M., NDVI differencing and post-classification to detect vegetation changes in Halabja City, Iraq. *IOSR Journal of Applied Geology and Geophysics* **2013,** *1* (2), 01-10.

9. OPCW By the Numbers. https://www.opcw.org/media-centre/opcw-numbers (accessed September 22, 2020).

10. Enserink, M., U.N. Taps Special Labs to Investigate Syrian Attack. *Science* **2013,** *341* (6150), 1050-1051.

11. Schwirtz, M.; Eddy, M., Aleksei Navalny Was Poisoned With Novichok, Germany Says. *The New York Times* September 2, 2020.

12. Munro, N. B.; Talmage, S. S.; Griffin, G. D.; Waters, L. C.; Watson, A. P.; King, J. F.; Hauschild, V., The sources, fate, and toxicity of chemical warfare agent degradation products. *Environ. Health Perspect.* **1999,** *107* (12), 933-974.

13. DeCoste, J. B.; Peterson, G. W., Metal–Organic Frameworks for Air Purification of Toxic Chemicals. *Chem. Rev.* **2014,** *114* (11), 5695-5727.

14. Yang, Y. C.; Baker, J. A.; Ward, J. R., Decontamination of chemical warfare agents. *Chem. Rev.* **1992,** *92* (8), 1729-1743.

15. Smith, B. M., Catalytic methods for the destruction of chemical warfare agents under ambient conditions. *Chem. Soc. Rev.* **2008,** *37* (3), 470-478.

16. Ebrahim, A. M.; Plonka, A. M.; Tian, Y.; Senanayake, S. D.; Gordon, W. O.; Balboa, A.; Wang, H.; Collins-Wildman, D. L.; Hill, C. L.; Musaev, D. G.; Morris, J. R.; Troya, D.; Frenkel, A. I., Multimodal Characterization of Materials and Decontamination Processes for Chemical Warfare Protection. *ACS Appl. Mater. Interfaces* **2019**.

17. Grissom, T. G.; Plonka, A. M.; Sharp, C. H.; Ebrahim, A. M.; Tian, Y.; Collins-Wildman, D. L.; Kaledin, A. L.; Siegal, H. J.; Troya, D.; Hill, C. L.; Frenkel, A. I.; Musaev, D. G.; Gordon, W. O.; Karwacki, C. J.; Mitchell, M. B.; Morris, J. R., Metal–Organic Framework- and Polyoxometalate-Based Sorbents for the Uptake and Destruction of Chemical Warfare Agents. *ACS Appl. Mater. Interfaces* **2020**.

18. Sundarrajan, S.; Chandrasekaran, A. R.; Ramakrishna, S., An Update on Nanomaterials-Based Textiles for Protection and Decontamination. *J. Am. Ceram. Soc.* **2010,** *93* (12), 3955-3975.

19. Wilson, C.; Main, M. J.; Cooper, N. J.; Briggs, M. E.; Cooper, A. I.; Adams, D. J., Swellable functional hypercrosslinked polymer networks for the uptake of chemical warfare agents. *Polymer Chemistry* **2017,** *8* (12), 1914-1922.

20. Cojocaru, B.; Neaţu, Ş.; Pârvulescu, V. I.; Şomoghi, V.; Petrea, N.; Epure, G.; Alvaro, M.; Garcia, H., Synergism of Activated Carbon and Undoped and Nitrogen-doped TiO2 in the Photocatalytic Degradation of the Chemical Warfare Agents Soman, VX, and Yperite. *ChemSusChem* **2009,** *2* (5), 427-436.

21. Sullivan, P. D.; Stone, B. R.; Hashisho, Z.; Rood, M. J., Water adsorption with hysteresis effect onto microporous activated carbon fabrics. *Adsorption* **2007,** *13* (3), 173-189.

22. Quinn, D. M., Acetylcholinesterase: enzyme structure, reaction dynamics, and virtual transition states. *Chem. Rev.* **1987,** *87* (5), 955-979.

23. Bigley, A. N.; Raushel, F. M., Catalytic mechanisms for phosphotriesterases. *Biochimica et Biophysica Acta (BBA) - Proteins and Proteomics* **2013,** *1834* (1), 443-453.

24. *Recommendations for the disposal of chemical agents and munitions*. National Academy Press: Washington, D.C., 1994.

25. Epstein, J.; Demek, M. M.; Rosenblatt, D. H., Notes - Reaction of Paraoxon with Hydrogen Peroxide in Dilute Aqueous Solution. *The Journal of Organic Chemistry* **1956,** *21* (7), 796-797.

26. Yang, Y.-C.; J. Berg, F.; L. Szafraniec, L.; T. Beaudry, W.; A. Bunton, C.; Kumar, A., Peroxyhydrolysis of nerve agent VX and model compounds and related nucleophilic reactions. *Journal of the Chemical Society, Perkin Transactions 2* **1997,** (3), 607-614.

27. Epstein, J.; Bauer, V. E.; Saxe, M.; Demek, M. M., The chlorine-catalyzed hydrolysis of isopropyl methylphosphonofluoridate (sarin) in aqueous solution. *J. Am. Chem. Soc.* **1956,** *78* (16), 4068-4071.

28. Simanenko, Y. S.; Savelova, V. A.; Prokop'eva, T. M.; Mikhailov, V. A.; Turovskaya, M. K.; Karpichev, E. A.; Popov, A. F.; Gillitt, N. D.; Bunton, C. A., Bis(dialkylamide)hydrogen Dibromobromate Precursors of Hypobromite Ion in Reactions with Nerve and Blister Agent Simulants. *The Journal of Organic Chemistry* **2004,** *69* (26), 9238-9240.

29. Courtney, R. C.; Gustafson, R. L.; Westerback, S. J.; Hyytiainen, H.; Chaberek, S. C.; Martell, A. E., Metal Chelate Compounds as Catalysts in the Hydrolysis of Isopropyl Methylphosphonofluoridate and Diisopropylphosphorofluoridate1. *J. Am. Chem. Soc.* **1957,** *79* (12), 3030-3036.

30. Melnychuk, S. A.; Neverov, A. A.; Brown, R. S., Catalytic Decomposition of Simulants for Chemical Warfare V Agents: Highly Efficient Catalysis of the Methanolysis of Phosphonothioate Esters. *Angew. Chem. Int. Ed.* **2006,** *45* (11), 1767-1770.

31. Balow, R. B.; Lundin, J. G.; Daniels, G. C.; Gordon, W. O.; McEntee, M.; Peterson, G. W.; Wynne, J. H.; Pehrsson, P. E., Environmental Effects on Zirconium Hydroxide

Nanoparticles and Chemical Warfare Agent Decomposition: Implications of Atmospheric Water and Carbon Dioxide. *ACS Appl. Mater. Interfaces* **2017,** *9* (45), 39747-39757.

32. Li, P.; Moon, S.-Y.; Guelta, M. A.; Lin, L.; Gómez-Gualdrón, D. A.; Snurr, R. Q.; Harvey, S. P.; Hupp, J. T.; Farha, O. K., Nanosizing a Metal–Organic Framework Enzyme Carrier for Accelerating Nerve Agent Hydrolysis. *ACS Nano* **2016**.

33. Katz, M. J.; Mondloch, J. E.; Totten, R. K.; Park, J. K.; Nguyen, S. T.; Farha, O. K.; Hupp, J. T., Simple and Compelling Biomimetic Metal–Organic Framework Catalyst for the Degradation of Nerve Agent Simulants. *Angew. Chem. Int. Ed.* **2014,** *53* (2), 497-501.

34. Moon, S.-Y.; Liu, Y.; Hupp, J. T.; Farha, O. K., Instantaneous Hydrolysis of Nerve-Agent Simulants with a Six-Connected Zirconium-Based Metal–Organic Framework. *Angew. Chem. Int. Ed.* **2015,** *54* (23), 6795-6799.

35. Mondloch, J. E.; Katz, M. J.; Isley Iii, W. C.; Ghosh, P.; Liao, P.; Bury, W.; Wagner, G. W.; Hall, M. G.; DeCoste, J. B.; Peterson, G. W.; Snurr, R. Q.; Cramer, C. J.; Hupp, J. T.; Farha, O. K., Destruction of chemical warfare agents using metal–organic frameworks. *Nat Mater* **2015,** *14* (5), 512-516.

36. Bandosz, T. J.; Laskoski, M.; Mahle, J.; Mogilevsky, G.; Peterson, G. W.; Rossin, J. A.; Wagner, G. W., Reactions of VX, GD, and HD with $Zr(OH)_4$: Near Instantaneous Decontamination of VX. *J. Phys. Chem. C* **2012,** *116* (21), 11606-11614.

37. Iordanov, I. O.; Bermudez, V. M.; Knox, C. K., Computational Modeling of the Structure and Properties of $Zr(OH)_4$. *J. Phys. Chem. C* **2018,** *122* (10), 5385-5400.

38. Troya, D., Reaction Mechanism of Nerve-Agent Decomposition with Zr-Based Metal Organic Frameworks. *J. Phys. Chem. C* **2016,** *120* (51), 29312-29323.

39. Wang, G.; Sharp, C.; Plonka, A. M.; Wang, Q.; Frenkel, A. I.; Guo, W.; Hill, C.; Smith, C.; Kollar, J.; Troya, D.; Morris, J. R., Mechanism and Kinetics for Reaction of the Chemical Warfare Agent Simulant, DMMP(g), with Zirconium(IV) MOFs: An Ultrahigh-Vacuum and DFT Study. *J. Phys. Chem. C* **2017,** *121* (21), 11261-11272.

40. Ghabili, K.; Agutter, P. S.; Ghanei, M.; Ansarin, K.; Panahi, Y.; Shoja, M. M., Sulfur mustard toxicity: History, chemistry, pharmacokinetics, and pharmacodynamics. *Critical Reviews in Toxicology* **2011,** *41* (5), 384-403.

41. Bae, S. Y.; Winemiller, M. D., Mechanistic Insights into the Hydrolysis of 2-Chloroethyl Ethyl Sulfide: The Expanded Roles of Sulfonium Salts. *The Journal of Organic Chemistry* **2013,** *78* (13), 6457-6470.

42. Elmore, D. T.; Gulland, J. M.; Jordan, D. O.; Taylor, H. F. W., The reaction of nucleic acids with mustard gas. *Biochem. J.* **1948,** *42* (2), 308-316.

43. Chauhan, S.; Chauhan, S.; D'Cruz, R.; Faruqi, S.; Singh, K. K.; Varma, S.; Singh, M.; Karthik, V., Chemical warfare agents. *Environ. Toxicol. Pharmacol.* **2008,** *26* (2), 113-122.

44. Shakarjian, M. P.; Heck, D. E.; Gray, J. P.; Sinko, P. J.; Gordon, M. K.; Casillas, R. P.; Heindel, N. D.; Gerecke, D. R.; Laskin, D. L.; Laskin, J. D., Mechanisms Mediating the Vesicant Actions of Sulfur Mustard after Cutaneous Exposure. *Toxicol. Sci.* **2009,** *114* (1), 5-19.

45. Wagner, G. W.; Yang, Y.-C., Rapid Nucleophilic/Oxidative Decontamination of Chemical Warfare Agents. *Ind. Eng. Chem. Res.* **2002,** *41* (8), 1925-1928.

46. Rhule, J. T.; Neiwert, W. A.; Hardcastle, K. I.; Do, B. T.; Hill, C. L., $Ag_5PV_2Mo_{10}O_{40}$, a Heterogeneous Catalyst for Air-Based Selective Oxidation at Ambient Temperature. *J. Am. Chem. Soc.* **2001,** *123* (48), 12101-12102.

47. Hong Le, N.; Han, Y.-h.; Jung, H.; Cho, J., Catalytic reaction system for rapid selective oxidation of alkyl sulphide. *J. Hazard. Mater.* **2019,** *379*, 120830.

48. Luo, Z.; Geletii, Y. V.; Hillesheim, D. A.; Wang, Y.; Hill, C. L., Mechanistic Studies of O2-Based Sulfoxidations Catalyzed by NOx/Br Systems. *ACS Catalysis* **2011,** *1* (10), 1364-1370.

49. Buru, C. T.; Li, P.; Mehdi, B. L.; Dohnalkova, A.; Platero-Prats, A. E.; Browning, N. D.; Chapman, K. W.; Hupp, J. T.; Farha, O. K., Adsorption of a Catalytically Accessible Polyoxometalate in a Mesoporous Channel-type Metal–Organic Framework. *Chem. Mater.* **2017,** *29* (12), 5174-5181.

50. Anslow, W. P.; Karnofsky, D. A.; Val Jager, B.; Smith, H. W., The Intravenous, Subcutaneous and Cutaneous Toxicity of Bis(β-chloroethyl) Sulfide (Mustard Gas) and of Various Derivatives. *J. Pharmacol. Exp. Ther.* **1948,** *93* (1), 1-9.

51. Long, D.-L.; Tsunashima, R.; Cronin, L., Polyoxometalates: Building Blocks for Functional Nanoscale Systems. *Angew. Chem. Int. Ed.* **2010,** *49* (10), 1736-1758.

52. Pope, M. T.; Müller, A., Polyoxometalate Chemistry: An Old Field with New Dimensions in Several Disciplines. *Angewandte Chemie International Edition in English* **1991,** *30* (1), 34-48.

53. Hill, C. L., Introduction: PolyoxometalatesMulticomponent Molecular Vehicles To Probe Fundamental Issues and Practical Problems. *Chem. Rev.* **1998,** *98* (1), 1-2.

54. Kozhevnikov, I. V., Catalysis by Heteropoly Acids and Multicomponent Polyoxometalates in Liquid-Phase Reactions. *Chem. Rev.* **1998,** *98* (1), 171-198.

55. Dong, J.; Lv, H.; Sun, X.; Wang, Y.; Ni, Y.; Zou, B.; Zhang, N.; Yin, A.; Chi, Y.; Hu, C., A Versatile Self-Detoxifying Material Based on Immobilized Polyoxoniobate for

Decontamination of Chemical Warfare Agent Simulants. *Chemistry – A European Journal* **2018,** *24* (72), 19208-19215.

56. Li, X.; Dong, J.; Liu, H.; Sun, X.; Chi, Y.; Hu, C., Recoverable amphiphilic polyoxoniobates catalyzing oxidative and hydrolytic decontamination of chemical warfare agent simulants in emulsion. *J. Hazard. Mater.* **2018,** *344*, 994-999.

57. Wang, Q.; Chapleski, R. C.; Plonka, A. M.; Gordon, W. O.; Guo, W.; Nguyen-Phan, T.-D.; Sharp, C. H.; Marinkovic, N. S.; Senanayake, S. D.; Morris, J. R.; Hill, C. L.; Troya, D.; Frenkel, A. I., Atomic-Level Structural Dynamics of Polyoxoniobates during DMMP Decomposition. *Scientific Reports* **2017,** *7* (1), 773.

58. Dong, J.; Hu, J.; Chi, Y.; Lin, Z.; Zou, B.; Yang, S.; Hill, C. L.; Hu, C., A Polyoxoniobate–Polyoxovanadate Double-Anion Catalyst for Simultaneous Oxidative and Hydrolytic Decontamination of Chemical Warfare Agent Simulants. *Angew. Chem. Int. Ed.* **2017,** *56* (16), 4473-4477.

59. Guo, W.; Lv, H.; Sullivan, K. P.; Gordon, W. O.; Balboa, A.; Wagner, G. W.; Musaev, D. G.; Bacsa, J.; Hill, C. L., Broad-Spectrum Liquid- and Gas-Phase Decontamination of Chemical Warfare Agents by One-Dimensional Heteropolyniobates. *Angew. Chem. Int. Ed.* **2016,** *55* (26), 7403-7407.

60. Mizrahi, D. M.; Saphier, S.; Columbus, I., Efficient heterogeneous and environmentally friendly degradation of nerve agents on a tungsten-based POM. *J. Hazard. Mater.* **2010,** *179* (1), 495-499.

61. Tian, Y.; Plonka, A. M.; Ebrahim, A. M.; Palomino, R. M.; Senanayake, S. D.; Balboa, A.; Gordon, W. O.; Troya, D.; Musaev, D. G.; Morris, J. R.; Mitchell, M. B.; Collins-Wildman, D. L.; Hill, C. L.; Frenkel, A. I., Correlated Multimodal Approach Reveals

Key Details of Nerve-Agent Decomposition by Single-Site Zr-Based Polyoxometalates. *J. Phys. Chem. Lett.* **2019**, 2295-2299.

62. Collins-Wildman, D. L.; Kim, M.; Sullivan, K. P.; Plonka, A. M.; Frenkel, A. I.; Musaev, D. G.; Hill, C. L., Buffer-Induced Acceleration and Inhibition in Polyoxometalate-Catalyzed Organophosphorus Ester Hydrolysis. *ACS Catalysis* **2018,** *8* (8), 7068-7076.

63. Hou, Y.; An, H.; Zhang, Y.; Hu, T.; Yang, W.; Chang, S., Rapid Destruction of Two Types of Chemical Warfare Agent Simulants by Hybrid Polyoxomolybdates Modified by Carboxylic Acid Ligands. *ACS Catalysis* **2018,** *8* (7), 6062-6069.

64. Hou, Y.; An, H.; Chang, S.; Zhang, J., Versatile catalysts constructed from hybrid polyoxomolybdates for simultaneously detoxifying sulfur mustard and organophosphate simulants. *Catalysis Science & Technology* **2019,** *9* (10), 2445-2455.

65. Reza, H., Use of Giant Nano-Polyoxotungstate as a Heterogeneous Catalyst for Green Selective Oxidation of Chemical Warfare Agent Simulants with Aqueous Hydrogen Peroxide. *Current Catalysis* **2017,** *6* (2), 97-104.

66. Giles, S. L.; Lundin, J. G.; Balow, R. B.; Pehrsson, P. E.; Wynne, J. H., Comparative roles of Zr4+ and Ni2+ Wells-Dawson hetero-metal substituted polyoxometalates on oxidation of chemical contaminants. *Applied Catalysis A: General* **2017,** *542*, 306-310.

67. Wu, K. H.; Yu, P. Y.; Yang, C. C.; Wang, G. P.; Chao, C. M., Preparation and characterization of polyoxometalate-modified poly(vinyl alcohol)/polyethyleneimine hybrids as a chemical and biological self-detoxifying material. *Polym. Degrad. Stab.* **2009,** *94* (9), 1411-1418.

68. Sharma, A.; Singh, B.; Saxena, A., Polyoxometalate impregnated carbon systems for the in situ degradation of sulphur mustard. *Carbon* **2009,** *47* (8), 1911-1915.

69. Buru, C. T.; Li, P.; Mehdi, B. L.; Dohnalkova, A.; Platero-Prats, A. E.; Browning, N. D.; Chapman, K. W.; Hupp, J. T.; Farha, O. K., Adsorption of a Catalytically Accessible Polyoxometalate in a Mesoporous Channel-type Metal–Organic Framework. *Chem. Mater.* **2017**.

70. Johnson, R. P.; Hill, C. L., Polyoxometalate oxidation of chemical warfare agent simulants in fluorinated media. *J. Appl. Toxicol.* **1999,** *19* (S1), S71-S75.

71. Lauinger, S. M.; Piercy, B. D.; Li, W.; Yin, Q.; Collins-Wildman, D. L.; Glass, E. N.; Losego, M. D.; Wang, D.; Geletii, Y. V.; Hill, C. L., Stabilization of Polyoxometalate Water Oxidation Catalysts on Hematite by Atomic Layer Deposition. *ACS Appl. Mater. Interfaces* **2017,** *9* (40), 35048-35056.

Chapter 2: Buffer-Induced Acceleration and Inhibition in Polyoxometalate-Catalyzed Organophosphorus Ester Hydrolysis

2.1 Introduction

The removal of toxic organophosphorus nerve agents and pesticides remains a significant and general goal. Ideally, this would be accomplished by materials that can either sequester or catalytically transform OP substances into nontoxic forms.[1-3] The primary route for decomposition of OP chemical warfare agents (CWAs) is hydrolysis.[4] While strong bases can be used to hydrolyze and destroy large stockpiles of these nerve agents, the development of personal protective equipment requires a material, preferably a catalytic one, that can be integrated into masks and garments.[2, 5]

Metal oxides, metal hydroxides, and metal organic frameworks (MOFs) have been studied extensively as potential materials for such protective equipment.[3, 6-14] The Lewis acidic sites of these materials coordinate the phosphoryl (P=O) oxygen of the nerve agent and activate the phosphorus oxygen bond making it more susceptible to nucleophilic attack thereby accelerating the hydrolysis rate.[3] Recent studies have further interrogated the reactions of CWAs and simulants with MOF systems using synchrotron-based spectroscopic techniques (X-ray absorption near-edge structure, extended X-ray absorption fine structure, X-ray photoelectron spectroscopy, X-ray powder diffraction, and Raman spectroscopy) along with complementary computation.[15-17] Despite the use of these advanced methods, the heterogeneous nature of these materials continues to generate challenges in determining the exact mechanism of the reactions, including the nature of substrate/product interactions with the active site.

An in-depth understanding of the mechanism and governing factors of metal-catalyzed CWA decomposition is vital for optimizing catalyst performance. Therefore, the study of a molecular metal-based Lewis acid catalyst, would directly complement the existing body of research on heterogeneous hydrolysis catalysts. Techniques amenable to molecular systems, such

as solution-phase nuclear magnetic resonance (NMR), would help facilitate the elucidation of mechanistic details of the CWA decontamination. One such compound is the zirconium containing polyoxometalate (POM), $(Et_2NH_2)_8[\{\alpha\text{-}PW_{11}O_{39}Zr(\mu\text{-}OH)(H_2O)\}_2]\cdot 7H_2O$ (**1**),[18] which is known to be an effective peptide and RNA hydrolysis catalyst.[19-24]

POMs are a class of highly modifiable, molecular transition-metal oxygen-anions that can function as oxidation, reduction, and hydrolysis catalysts.[25-33] They are capable of forming complexes with many elements across the periodic table[34] and can act as ligands for the strongly Lewis acidic metal ions including Zr(IV)[18, 35-37] and Ce(IV).[38] Over the past decade, Parac-Vogt and co-workers have studied the POM-catalyzed hydrolysis of a number of compounds including polypeptides and organophosphate RNA analogues.[39-44] They have demonstrated that Lewis acidic metal centers, including Zr(IV), activate phosphorus-oxygen bonds and enhance the rate of phosphate hydrolysis.[41] In addition, they have thoroughly examined several factors that affect the hydrolysis of organophosphorus compounds including ionic strength, pH, temperature, and catalyst concentration.[19-21, 41, 42, 45-47]

Given that most nerve agent hydrolysis products, such as methylphosphonic acid (MPA), are acidic, and that hydrolysis is an inherently pH-dependent process, it is vital to have a buffer to maintain constant pH.[3, 48, 49] Furthermore, an analysis of the existing literature shows that the impact of buffers on the reaction outcome can be significant.[50-52] Herein, we report the considerable and diverse impact of common buffers on hydrolysis of the OP ester nerve agent simulant, methyl-paraoxon or *O,O*-dimethyl *O*-(4-nitrophenyl) phosphate (DMNP) catalyzed by the Zr-POM, **1**, (Scheme 2.1) and suggest a possible mechanism for the observed effects. This compound, **1,** was chosen as its speciation in solution has been well characterized and it is one of the most active Zr-substituted POM hydrolysis catalysts. We report the specific effects of

different buffer anions on Lewis acid-catalyzed OP ester hydrolysis while carefully controlling the pH, ionic strength, catalyst concentration, and substrate concentration. Together these results mark significant progress toward a full mechanistic understanding of homogeneous CWA hydrolysis by electrophilic zirconium centers and serve as insightful homogeneous models for heterogeneous Zr-based catalysts.

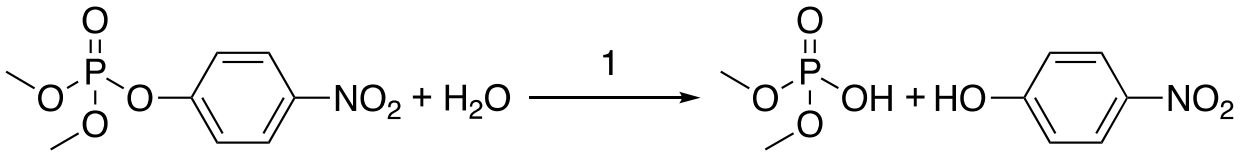

Scheme 2.1. The hydrolysis of O,O-dimethyl O-(4-nitrophenyl) phosphate (DMNP) in the presence of the POM catalyst **1**.

2.2 Experimental

2.2.1 Materials and General Methods

All chemicals were of commercial quality unless otherwise specified. Buffers were made by dissolving the desired concentration of acid in water, followed by adjustment to the desired pH by concentrated sodium hydroxide. This was done using volumetric glassware conducting the pH adjustment with most of the desired volume present before filling to the mark once the desired pH was reached. All pH measurements were done using an Orion 230A pH meter.

2.2.2 Catalyst Preparation and Characterization

Synthesis of $(Et_2NH_2)_8[\{\alpha\text{-}PW_{11}O_{39}Zr(\mu\text{-}OH)(H_2O)\}_2]\cdot 7H_2O$ ***(1)***. The Zr-containing POM, $(Et_2NH_2)_8[\{\alpha\text{-}PW_{11}O_{39}Zr(\mu\text{-}OH)(H_2O)\}_2]\cdot 7H_2O$ (**1**), was prepared via a modified version of literature procedures.[18, 19] Phosphotungstic acid (19.76 g) was dissolved in 100 mL of deionized water (solution A). Sodium bicarbonate solution (1 M) was added until a pH of 5.25 was reached. The volume of the solution was increased to 200 mL through the addition of

deionized water. Zirconyl chloride hydrate (1.024 g) was added to the solution and was stirred for 5 minutes. Hydrochloric acid (4 mL of a 1 M solution) was added dropwise followed by stirring of the solution for 30 minutes. In a separate container, additional zirconyl chloride hydrate (1.024 g) was dissolved in 16 mL of hydrochloric acid (1 M) (solution B). Solution B was added to A dropwise and then stirred for another 30 minutes. During this time, a small amount of precipitate forms. This precipitate was removed via centrifugation for 10 minutes at 4500 rpm. A rotary evaporator (bath at 40˚C) was used to reduce the volume to ~80 mL. This solution was heated at 90˚C for one minute in a glycerol bath. Diethylammonium chloride (10 g) was added to the solution followed by stirring for 5 minutes. The solution was cooled to room temperature and continuously stirred for 2 hours. The white powder was collected via centrifugation. This powder was then washed once with ethanol, and three times with diethyl ether. A glass stirring rod was used to agitate the powder in the washing solvent before being recollected via centrifugation. The resulting product was then dried in a vacuum oven.

*Synthesis of $(Et_2NH_2)_{10}[Zr(\alpha\text{-}PW_{11}O_{39})_2]\cdot 7H_2O$ (**2**).* The Zr-containing POM, $(Et_2NH_2)_{10}[Zr(\alpha\text{-}PW_{11}O_{39})_2]\cdot 7H_2O$ (**2**), was prepared by reacting a 2:1 molar ratio of $[\alpha\text{-}PW_{12}O_{40}]^{3-}$ with $ZrCl_2O\cdot 8H_2O$ in an aqueous Na_2CO_3 solution, followed by the addition of excess amounts of solid Et_2NH_2Cl as described in published procedures.[35]

*Synthesis of $K_7[\alpha\text{-}PW_{11}O_{39}]\bullet 14H_2O$ (**7**).* The monolacunary phosphotungstate, $K_7[\alpha\text{-}PW_{11}O_{39}]\cdot 14H_2O$, was prepared via a modified version of literature procedures.[53, 54] Phosphotungstic acid (4.8 g) was dissolved in 10 mL of deionized water. The pH was adjusted to 5.3 by adding a sodium bicarbonate solution (1 M). Potassium chloride (4 g) was added to the solution to precipitate the POM. The resulting precipitate was collected on a medium glass frit and air dried overnight.

Characterization Methods. Fourier transform infrared (FTIR) spectra were collected on a Nicolet 6700 FTIR spectrometer for samples **1**, **2**, and **7** (Figures 2.1-2.3). Samples were prepared as KBr pellets using FTIR-grade KBr and 1-2% sample by weight. ^{31}P NMR spectra of **1** and **2** were collected on a Bruker 600 (Figures 2.4-2.6). Instead of running experiments in a deuterated solvent such as D_2O, NMR tube inserts filled with D_2O were added to each tube to maintain the lock throughout data acquisition and allow the pH of the solution to be precisely controlled. For speciation studies, POMs were dissolved and the pH adjusted, and the samples were then immediately taken to the NMR instrument for characterization. For each spectrum, 1024 scans were taken with a delay time of 2 s. Determination of phase purity of solid samples of **1** was done using powder X-ray diffraction. The data were collected using a Rigaku Ultima-IV diffractometer equipped with Cu Kα radiation within a range of $5° \leq 2\theta \leq 40°$ (scanning rate: 1°/min). The unit cell parameters of ZrPOM were refined with LeBail fitting using the Jana2006 software, where peak shapes were refined with pseudo-Voigt function and peak asymmetry corrected with a Simpson function (Figure 2.7, Table 2.1).[55] The background was modeled manually using 50 points.

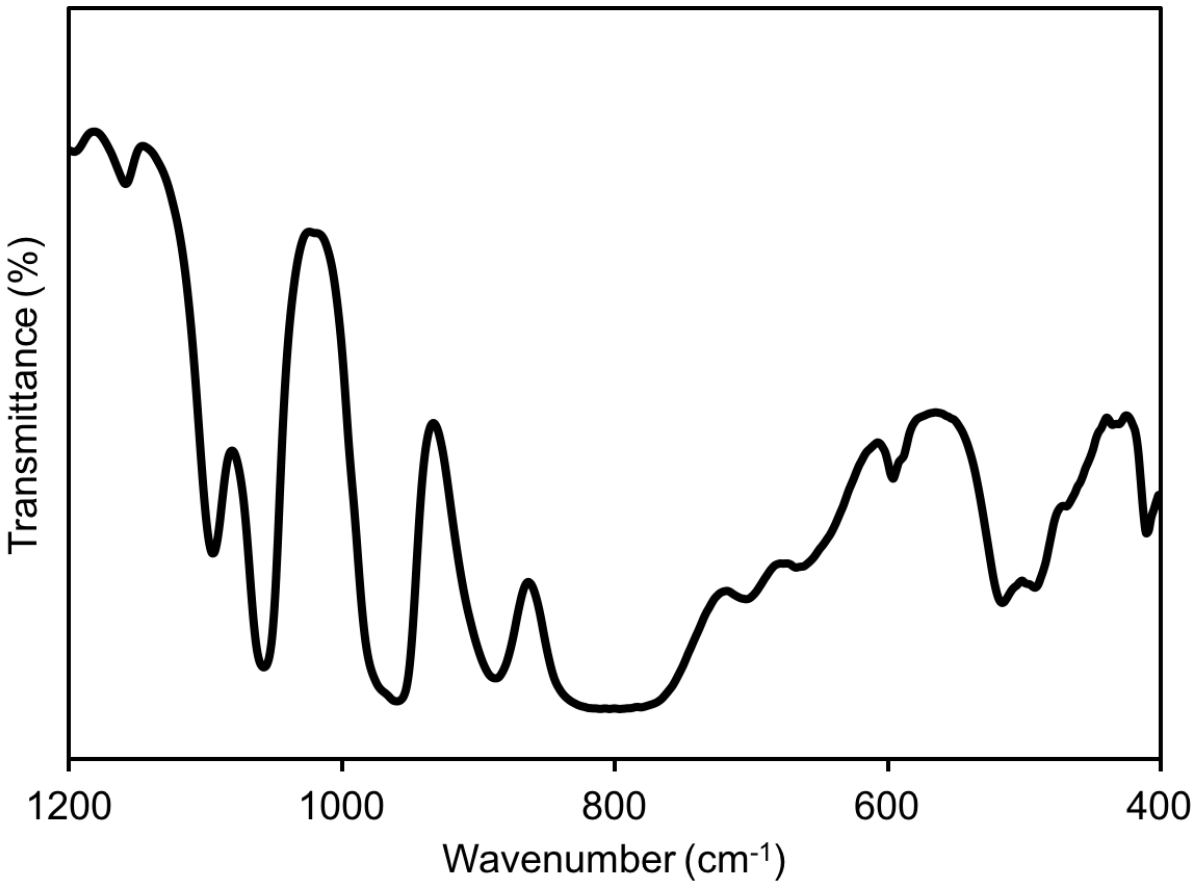

Figure 2.1. FTIR spectrum of $(Et_2NH_2)_8[\{\alpha\text{-}PW_{11}O_{39}Zr(\mu\text{-}OH)(H_2O)\}_2]\bullet 7H_2O$ (**1**).

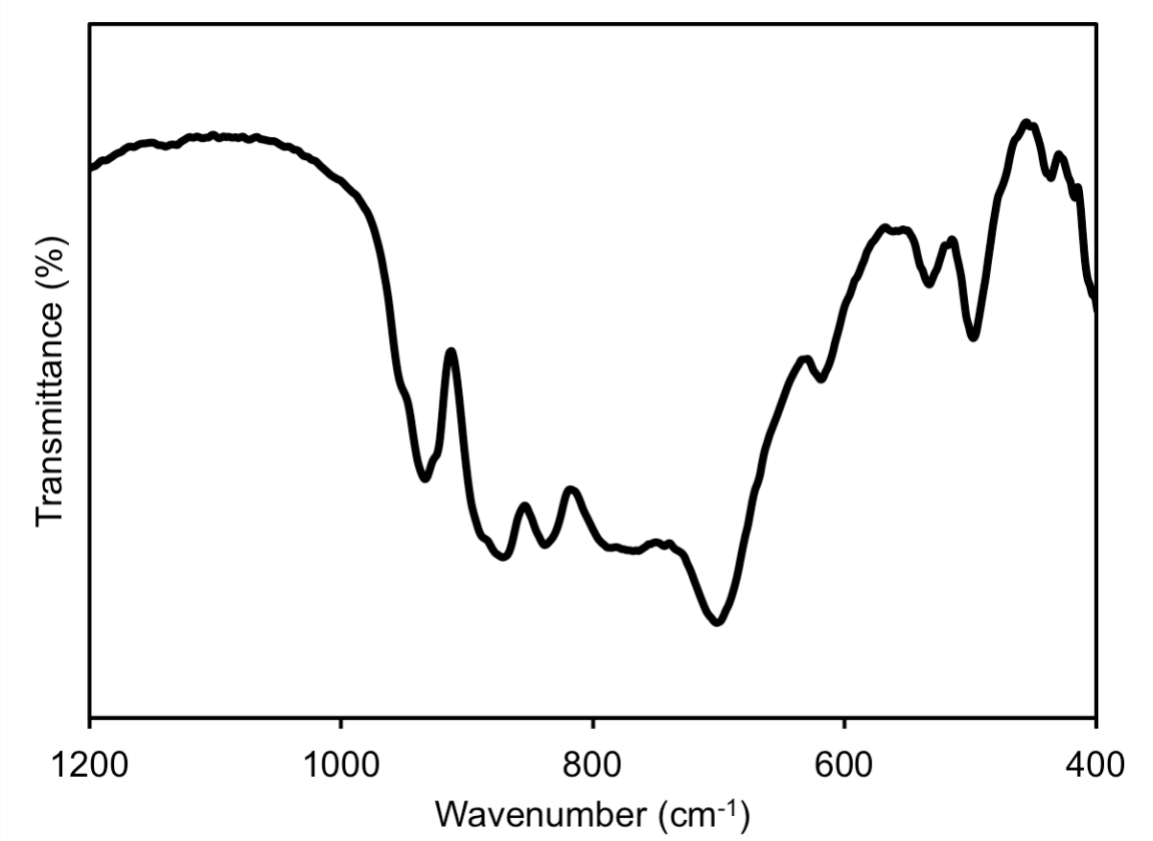

Figure 2.2. FTIR spectrum of $(Et_2NH_2)_{10}[Zr(\alpha\text{-}PW_{11}O_{39})_2]\bullet 7H_2O$ (**2**).

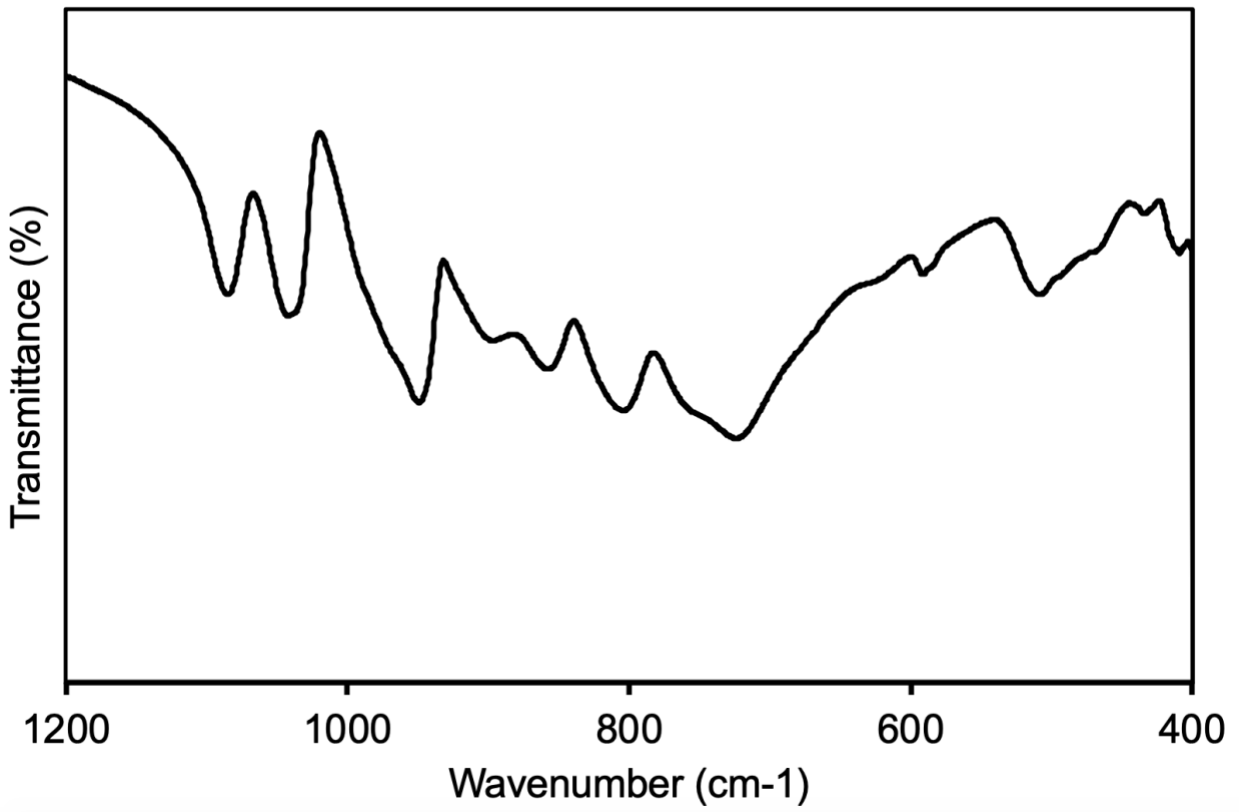

Figure 2.3. FTIR spectrum of $K_7[\alpha\text{-}PW_{11}O_{39}]\bullet 14H_2O$ (**7**).

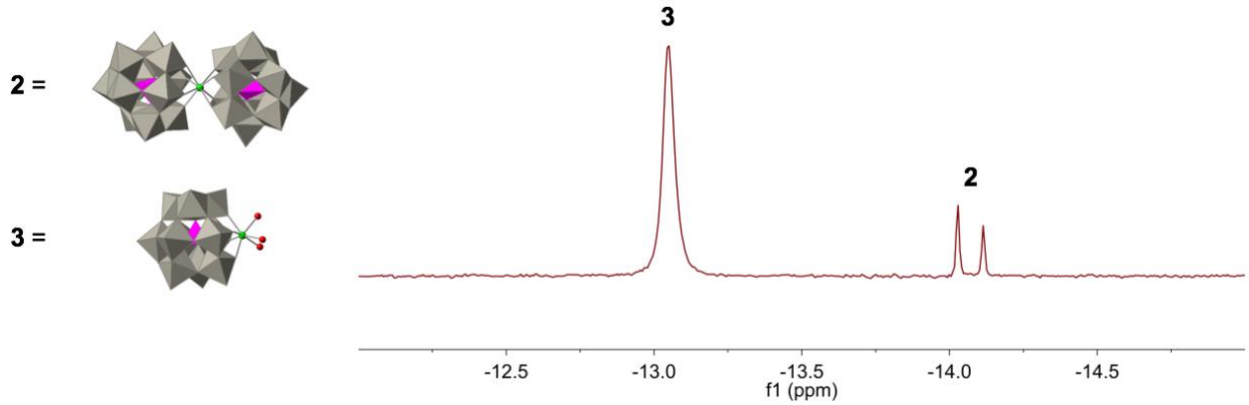

Figure 2.4. ^{31}P NMR spectrum of 2.5 mM **1** in deionized water at pH 4.8. Upon dissolution of **1** and subsequent pH adjustment to pH 4.8, species **2** and **3** are spontaneously generated. Solutions were pH adjusted with NaOH (600 MHz NMR, 1024 scans, 85% H_3PO_4). Polyhedral representation **2** is based on a known crystal structure while **3** is a cartoon of the likely structure present in solution.

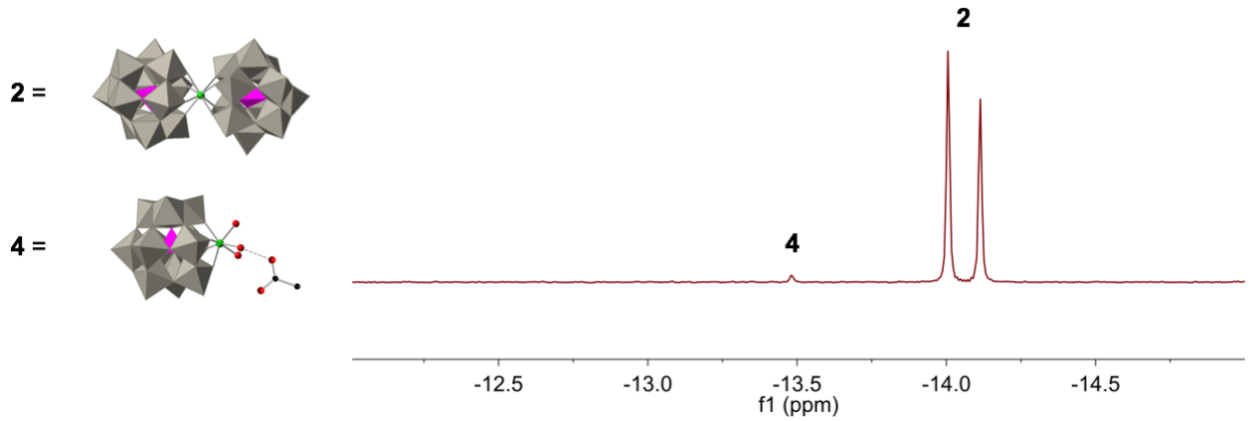

Figure 2.5. ^{31}P NMR spectrum of 2.5 mM **2** in 0.5 M NaAc buffer at pH 4.8. While **2** is the primary species present upon dissolution, a small amount of **4** is present. Solutions were pH adjusted with NaOH (600 MHz NMR, 1024 scans, 85% H_3PO_4). Polyhedral representation **2** is based on a known crystal structure while **4** is a cartoon of the likely structure present in solution.

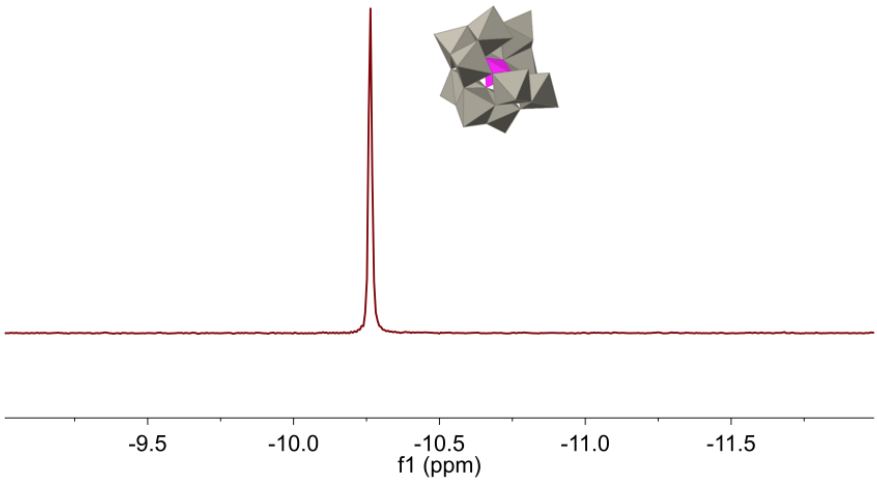

Figure 2.6. ^{31}P NMR spectrum of $K_7[\alpha\text{-}PW_{11}O_{39}]\cdot 14H_2O$ at pH 4.8. Solutions were pH adjusted with NaOH (600 MHz NMR, 1024 scans, 85% H_3PO_4).

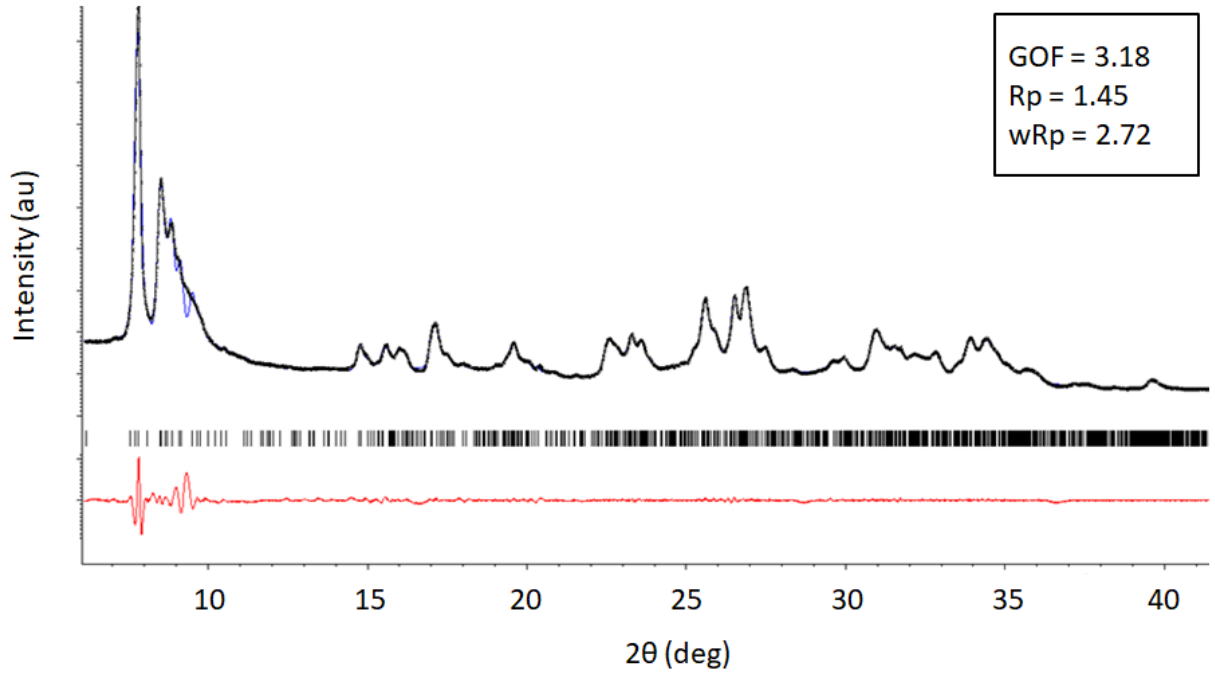

Figure 2.7. Powder X-ray diffraction of **1**. Results of Le Bail fit: the black trace is the observed pattern; the blue trace is the calculated profile; and the red trace is the difference.

sample	a (Å)	b (Å)	c (Å)	α(º)	β(º)	γ(º)	T (K)
ZrPOM	11.562(1)	20.601(2)	23.085(3)	79.53(5)	79.20(5)	90.43(5)	300

Table 2.1. Unit cell parameters obtained from Le Bail fit.

2.2.3 Hydrolysis Studies

The pK_a of *p*-nitrophenol is 6.7, and when deprotonated it exhibits a strong absorption band at 401 nm with an extinction coefficient of 18,390 $M^{-1}\cdot cm^{-1}$; in contrast, the protonated form is colorless.[56] Product formation during DMNP hydrolysis was therefore followed by measuring the strong absorption band of the hydrolysis product *p*-nitrophenolate on an Agilent 8453 UV-visible spectrophotometer. The initial rates were then determined from the slope of *p*-nitrophenolate formation vs. time. Given that the reactions were conducted at pH values well below the pK_a of *p*-nitrophenol, small aliquots of the reaction solution were diluted by addition of 3 mL of pH 10, 0.45 M sodium borate buffer. This gave an appropriate concentration for absorption measurements and ensured the product *p*-nitrophenol was well above its pK_a, yielding quantitative results. Full reaction conversion was confirmed by ^{31}P NMR (Figure 2.8).

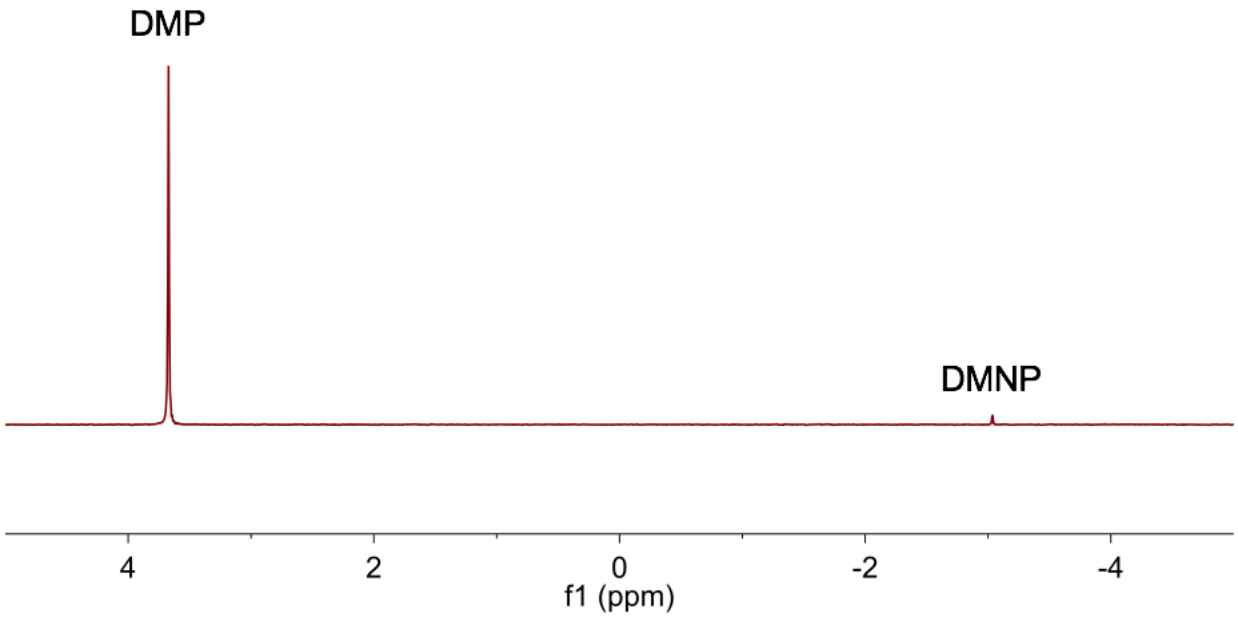

Figure 2.8. ^{31}P NMR spectrum of the substrate, *O,O*-dimethyl *O*-(4-nitrophenyl) phosphate (DMNP), and product, dimethyl phosphate (DMP), post catalysis. Starting conditions: 2.5 mM **1** at pH 4.8 with 4.3 mM DMNP. The solution was pH adjusted with NaOH (600 MHz NMR, 1024 scans, 85% H_3PO_4).

Example Hydrolysis Procedure. Stock solutions of **1** (5 mM) and DMNP (20.6 mM) were prepared 20 minutes prior to beginning the kinetic experiments in an acetic acid/acetate buffer (0.5 M) at pH 4.8. Hydrolysis of DMNP in the buffer is sufficiently slow relative to the catalyst that product formation during this step is negligible, however, fresh stock solutions were prepared before each set of experiments. In a scintillation vial 2.5 mL of each solution were combined and a timer started. Every ten minutes 200 µL of the mixture was removed, added to 3 mL of pH 10 borate buffer (0.45 M), swirled vigorously and immediately poured into a quartz cell where the absorption was measured. The quartz cell was rinsed 3 times with deionized water between measurements.

For all hydrolysis experiments, separate solutions of POM and DMNP were prepared and then combined to start the reaction. Reported concentrations are based on the combined volume of the two starting solutions. DMNP solutions were prepared at least 20 min prior to the start of the reaction because DMNP does not dissolve immediately in aqueous solution. During this time, negligible hydrolysis occurs as seen in the control reaction (Figure 2.11). The pH was adjusted after the dissolution of the POM but before the addition of DMNP to the solution, preventing product formation during pH adjustment. The timer was started upon addition of DMNP. The pH was measured again after the last absorption measurement was taken.

2.2.4 Computational Methods

Geometry of the presented polyanions was optimized in implicit water solution, with no geometry (or symmetry) constraints, at their ground singlet electronic states. In these calculations, we used the DFT method (M06L functional)[57] in conjunction with the split-valence 6-31G(d,p) basis sets for O, C, H, P, Na and lanl2dz basis sets and associated ECPs for the W and Zr atoms.[58-60] The solvent effects were approximated by the polarizable continuum model (CPCM).[61-63] All calculations were carried out with the Gaussian 09 software package.[64]

2.3 Results and Discussion

Extensive studies by Parac-Vogt and co-workers on RNA analogue hydrolysis catalyzed by **1**, established that there is a complex set of equilibria that govern the speciation of **1** in solution. This speciation is influenced by temperature, pH, ionic strength, catalyst concentration, and substrate concentration.[19-24] At high temperature, ionic strength, catalyst and substrate concentrations, **1** converts to **2** (Scheme 2.2 eq. (1)). In a second equilibrium process, **1**

hydrolyzes to form two equivalents of the monomeric form $[\alpha\text{-}PW_{11}O_{39}Zr(OH)(H_2O)_2]^{4-}$ (**3**) (Scheme 2.2 eq. (2)).

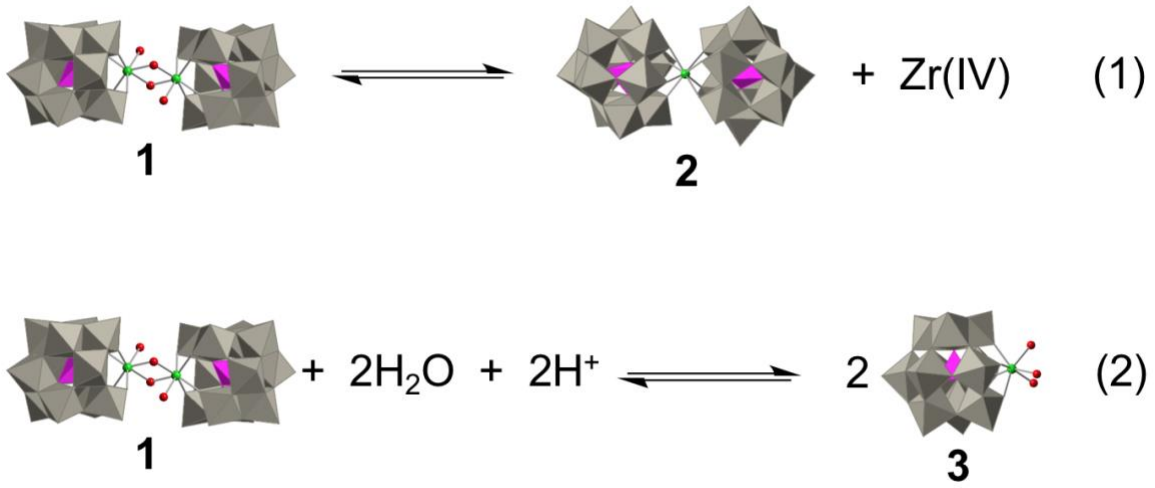

Scheme 2.2. Speciation of **1**: 1) loss of bridging hydroxides and one zirconium center to form the 8-coordinate complex, **2**. 2) hydrolysis of **1** to form **3**. This process is favorable at lower pH. WO_6, grey octahedra; PO_4, purple tetrahedra; Zr, green; O, red.

The pH dependence of this reaction can be monitored by ^{31}P NMR (Figure 2.9). Under acidic conditions, a single resonance is observed at -13.06 ppm while at pH 7 there is a distinct chemical shift further downfield (-12.90). At pH 8 the POMs become unstable, and compounds **1**, **2** and **3** decompose. At middle pH values (4-6), there are broadened peaks between these two resonances consistent with rates for equilibration that are comparable to the NMR timescale.[65] Previous diffusion-ordered spectroscopy (DOSY) NMR studies confirmed the existence of **3** below pH 4 and assigned **1** to the peak further downfield.[22] Given that **3** has multiple aqua ligands and is less sterically encumbered, it is expected to be more active than **1**. Compound **2** is coordinatively saturated, and it is therefore completely inactive.[24] Herein, knowledge of this speciation is used to inform experimental design. When **1** is used for subsequent experiments,

the majority of which are at pH 4.8, it is assumed that the more active form, **3**, is both present and responsible for the majority of the catalytic activity. For pH values where both **1** and **3** are present in solution, only one broadened peak at ~-13 ppm is observed preventing quantification of the relative amounts of both species. Thus, for simplicity, apart from Figure 2.9 where the speciation is specifically examined, the ^{31}P NMR resonance at ~-13 ppm is labeled as the more catalytically active species, **3**.

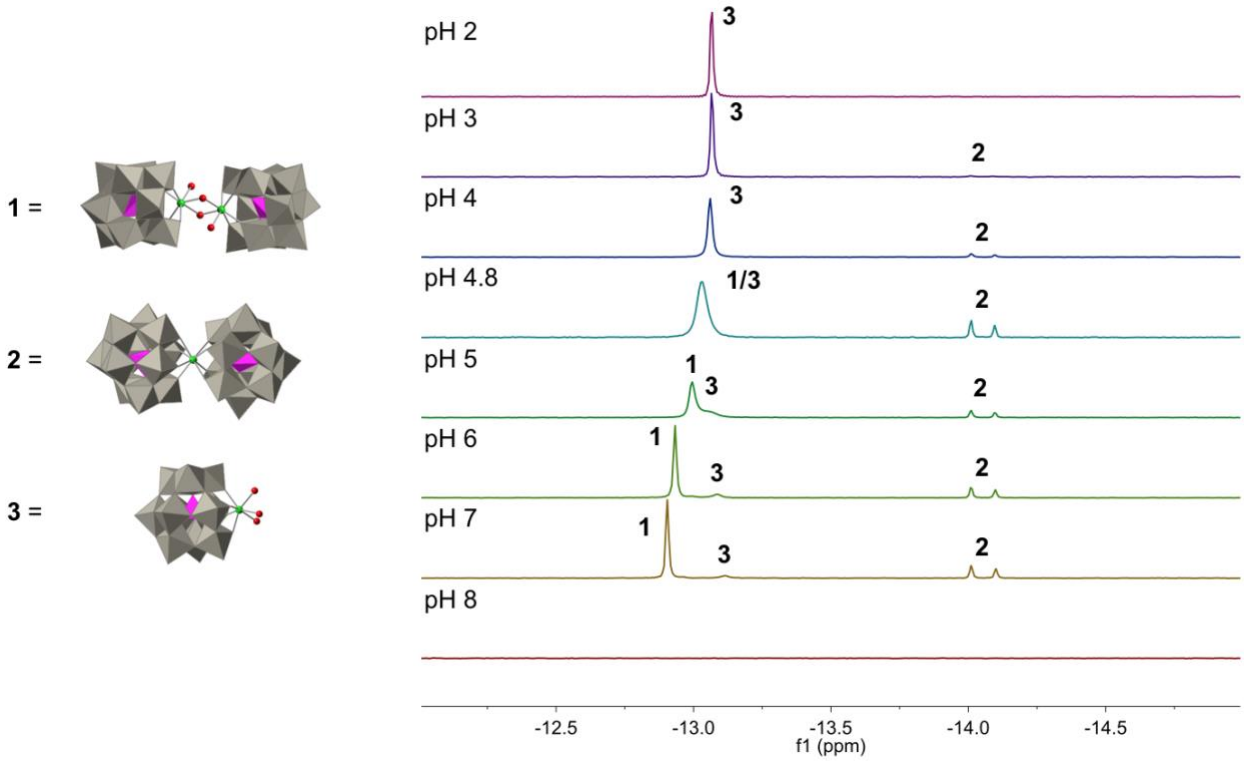

Figure 2.9. ^{31}P NMR of 2.5 mM **1** at varying pH values in deionized water. At pH 8 the lack of peaks for both **1** and **2** indicates they are unstable at this pH and have decomposed into other complexes not identified here. Solutions were pH adjusted with NaOH or $HClO_4$ (600 MHz NMR, 1024 scans, 85% H_3PO_4 internal standard). Polyhedral representations **1** and **2** are based on known crystal structures,[18, 35] while **3** is a cartoon of the likely structure present in solution.

The activity of **1** was established by measuring the rate of hydrolysis of DMNP as a function of the concentration of **1** (Figure 2.10). The initial rates are close to linearly proportional to the starting concentration of **1** indicating the reaction is first order in **1**. Any deviation likely results from the formation of **2** at higher concentrations of **1**.[20] Additionally, the acetic acid/acetate buffered solution containing 6 mM of **1** hydrolyzes DMNP 96 times faster than the control (no catalyst in this buffer), indicating that **1**, as expected, is a DMNP hydrolysis catalyst. Full catalytic conversion of four equivalents of DMNP is achieved at pH 4.8 using a 0.5 M acetic acid/acetate buffer (Figure 2.11). Unbuffered control reactions show that equivalent concentrations of aqueous zirconium exhibit some activity, although substantially less than **1**, while, the monolacunary Keggin, $K_7[\alpha\text{-}PW_{11}O_{39}]\cdot 14H_2O$ (**7**), and counter-cation, Et_2NH_2, both independently evaluated, show negligible activity above the baseline hydrolysis rate (Table 2.2). Varying the concentration of DMNP also shows that the hydrolysis is first order in this substrate (Figure 2.10).

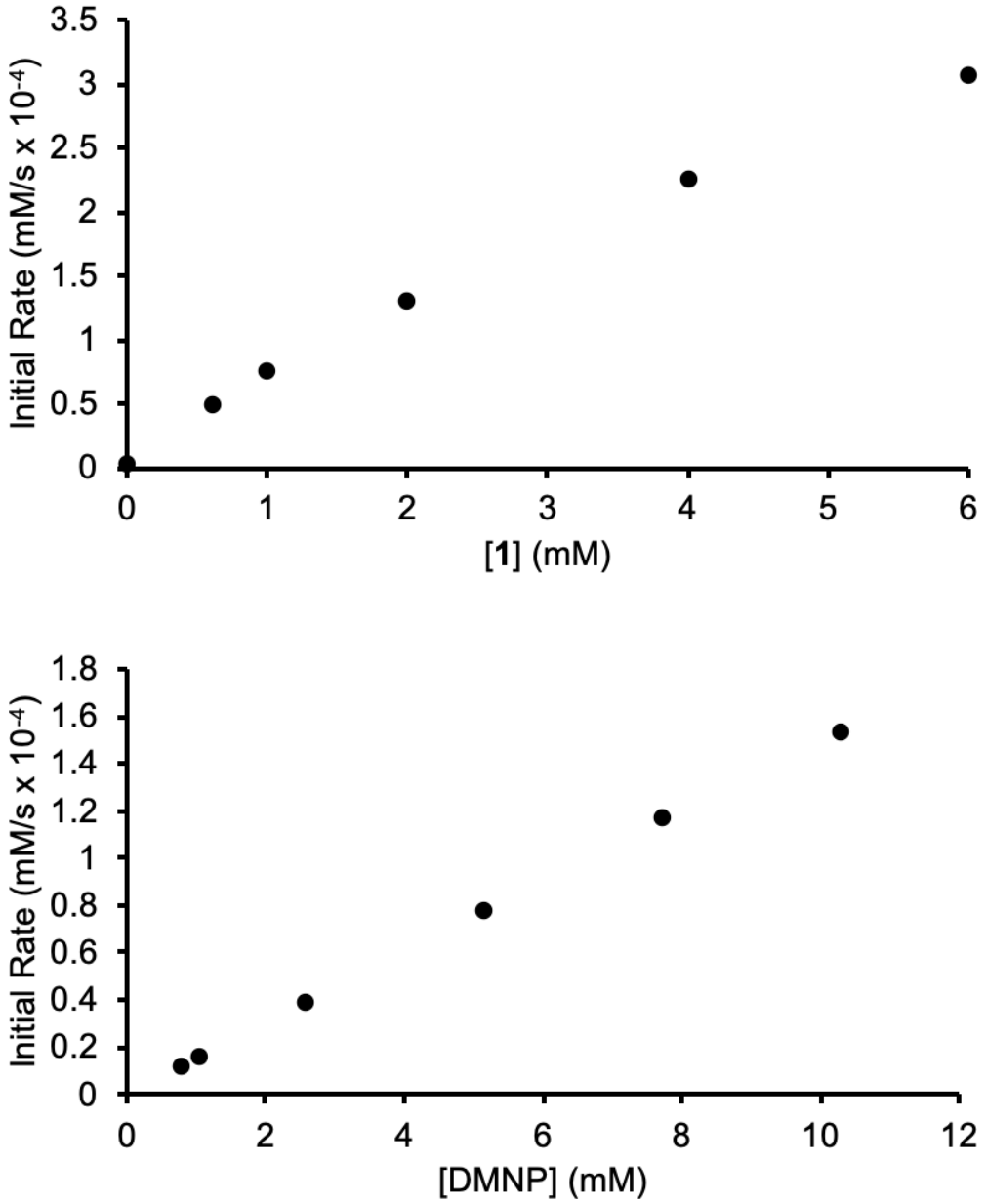

Figure 2.10. Top: Initial rate dependence of DMNP hydrolysis on **1**. Deviations from this nearly linear dependence at higher concentrations result from conversion of **1** to **2**. Conditions: [**1**] varied, 10.3 mM DMNP, pH 4.8, 0.5 M acetic acid/acetate buffer. Bottom: Initial rate dependence of DMNP hydrolysis on [DMNP]. Conditions: [DMNP] varied, 2.5 mM **1**, pH 4.8, 0.5 M acetic acid/acetate buffer.

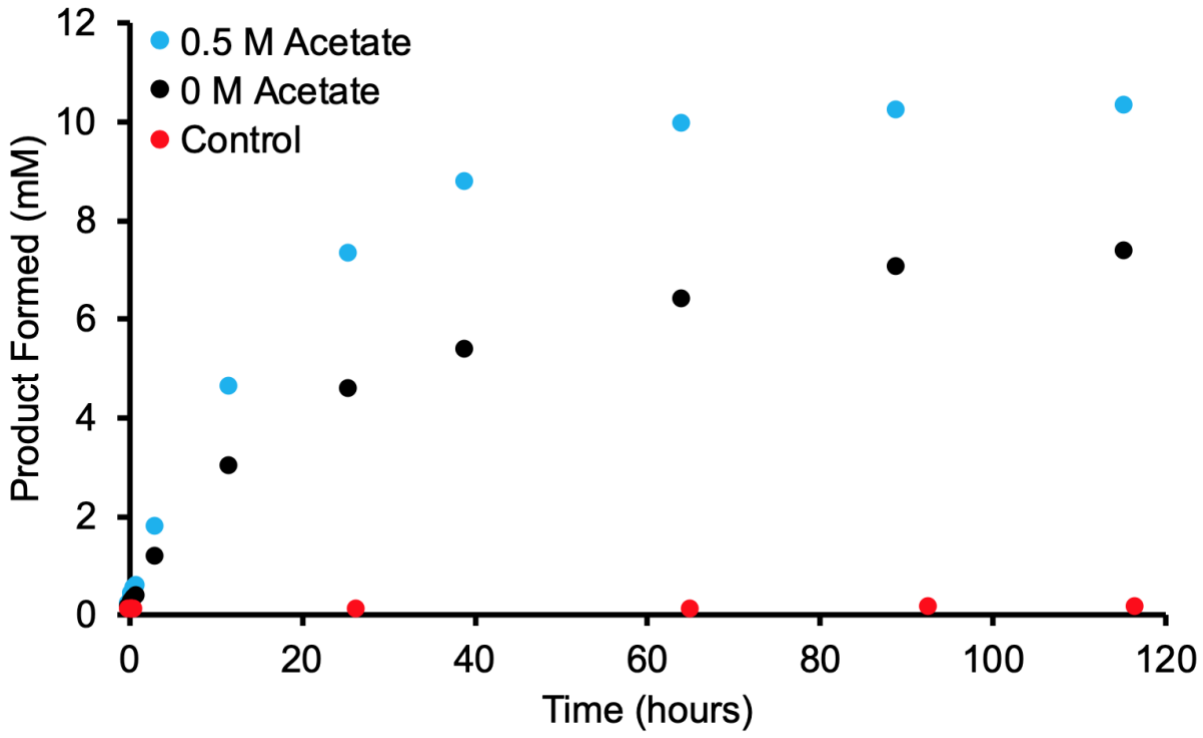

Figure 2.11. Product formation as a function of time for the full conversion of 10.3 mM DMNP. Conditions: pH 4.8, 10.3 mM DMNP, 2.5 mM **1** in the case of blue and black curves and 0 mM in the case of the red no-catalyst curve. An ionic strength was maintained at 0.3 M with 0.5 M acetic acid/acetate buffer (blue), or 0.3 M NaClO4 (black, red), pH adjusted with NaOH.

Conditions	**Initial Rate (nM/s)**
2.5 mM **1**	286
DI water only	0.54
2.5 mM **2**	15
5 mM $K_7[\alpha\text{-}PW_{11}O_{39}]\cdot 14H_2O$	1.2
20 mM Et_2NH_2Cl	1.8
5 mM $ZrOCl_2$	119

Table 2.2. Initial rates of unbuffered hydrolysis of 10.3 mM DMNP at pH 4.8 with no additional electrolyte added, pH adjusted with $HClO_4$ or NaOH.

Previous studies of organophosphate RNA analogue hydrolysis catalyzed by **1** have shown an initial rate dependence on the pH of the solution.[19-21] This pH dependence is particularly important because the hydrolysis product of DMNP, and nerve agent hydrolysis products more broadly, are acidic. The solution pH drops in conjunction with reaction conversion, and the effect is more pronounced in non-buffered media near neutral pH. To test this dependence, the initial rates of DMNP hydrolysis were assessed over a range of pH values from 3 to 7 (Figure 2.12). This study was done without the use of a buffer because no buffer can operate over such a broad range. For measurements of the initial rate, the pH drop from generation of acidic product is minimal.

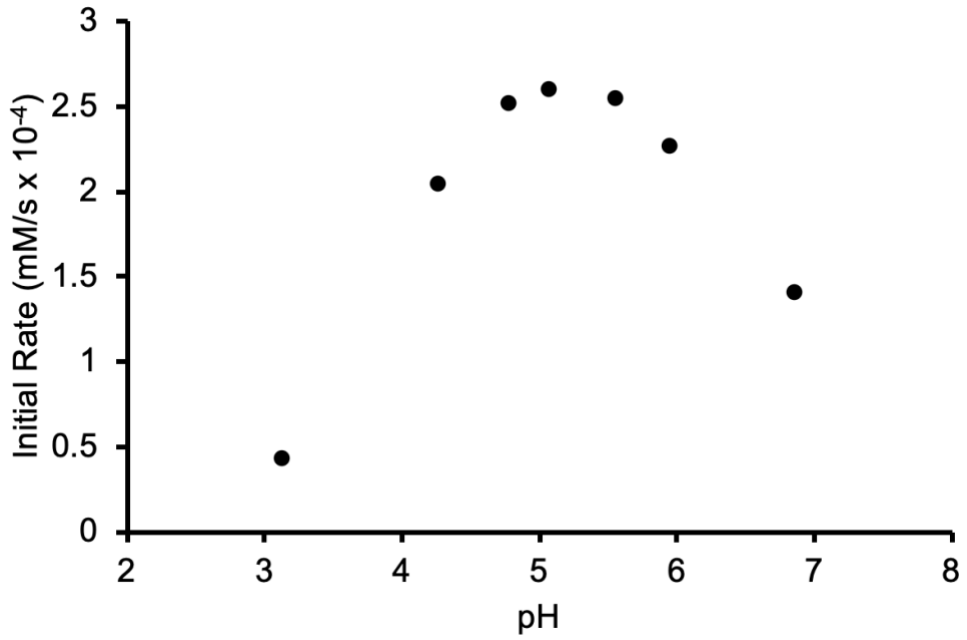

Figure 2.12. Initial rate dependence of DMNP hydrolysis on pH. Conditions: 2.5 mM **1**, 10.3 mM DMNP, pH adjusted with $HClO_4$ or NaOH.

Figure 2.12 shows that the initial rate maximizes at around pH 5, hence further studies were conducted in this pH range. The decrease in rate at lower pH values can be attributed to the

lack of a terminal hydroxide ligand on the zirconium center. Previous studies have shown that at lower pH, the predicted monomeric structure $[\alpha\text{-}PW_{11}O_{39}Zr(OH)(H_2O)_2]^{4-}$ becomes protonated, leaving only aqua ligands on the zirconium atom.[22] Because hydroxide is a better nucleophile, the reaction will proceed slower with water under the proposed mechanism for a single site catalyst.[3] At higher pH, the rate very likely decreases due to formation of the dimeric species, **1**, in solution, which also lacks a terminal hydroxide ligand and is more sterically hindered.[22]

Based on the pH dependence shown above and acidic nature of the hydrolysis product of DMNP, acetic acid-acetate at pH 4.8 was used to buffer many reactions in this study. Acetic acid has a pK_a of 4.76 which matches the pH window in which **1** has the highest activity. While buffering the solution is not essential for initial rate measurements, using a properly buffered solution allows a single system to be studied both at early times and under high turnover conditions.

A 0.5 M solution of acetate buffer at pH 4.8 has a calculated ionic strength of 0.3 M.[66] Before examining catalysis under buffered conditions, the effect of ionic strength was also evaluated using sodium perchlorate, which does not interact with the POM. While maintaining a constant pH, increasing the concentration of $NaClO_4$ decreases the rate of catalytic hydrolysis (Figure 2.13). There are multiple explanations for this observed slowing of the reaction: first, high ionic strength favors the formation of the inactive species **2**; second, there will be a decreased interaction between the partial negative charge on the oxygen of DMNP and the Zr(IV) center in **3**; and third, the increased ionic strength appears to shift the monomer/dimer equilibrium in favor of the dimer, **1**, as indicated by the downfield shift of the ^{31}P NMR peak at ~-13 ppm with increasing ionic strength (Figure 2.14). The NMR spectra also show that as the concentration of $NaClO_4$ increases from 0 to 0.3 M, the percentage of **2** increases from 12% at 0

M $NaClO_4$ to 20% at 0.3 M $NaClO_4$, which represents an 8% decrease in the active species. Interestingly, however, the initial rates drop from 2.9 x 10^{-4} to 1.0 x 10^{-4} M*s^{-1}, which represents a 66% rate decrease. This indicates that formation of **2** is not the sole cause of this rate loss. Instead, the weakened attractive force between the Zr-active site and DMNP or changes to the monomer and dimer equilibrium contribute to the rate decrease.

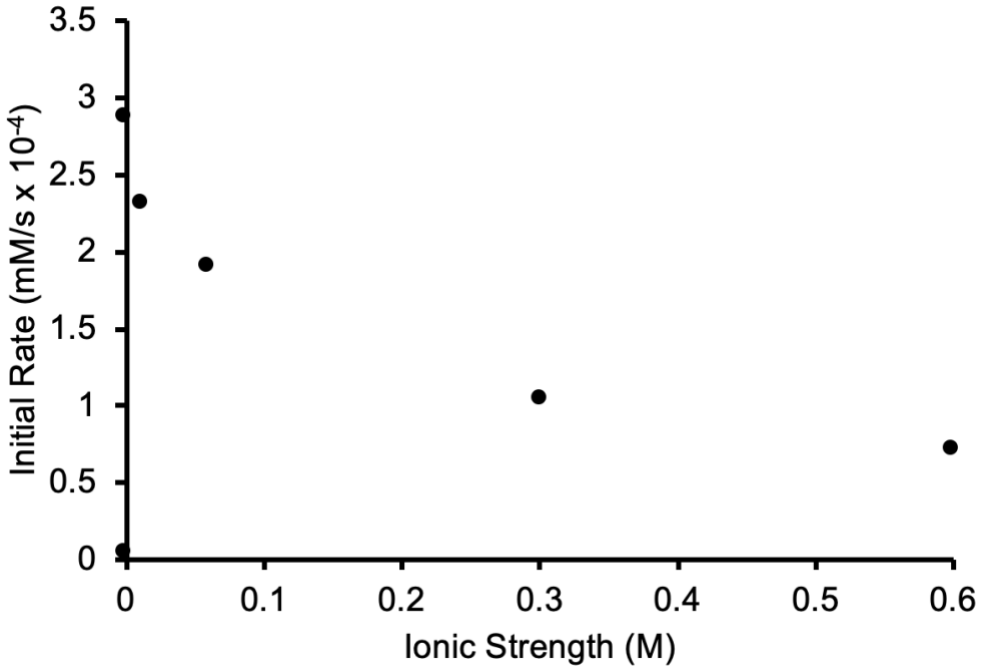

Figure 2.13. Initial rate dependence of DMNP hydrolysis on ionic strength. Higher ionic strength lowers the coulombic attraction between the Zr(IV) center and partial negative on the phosphoryl oxygen resulting in lower reactivity. Conditions: Varied [$NaClO_4$], 2.5 mM **1**, 10.3 mM DMNP, pH 4.8, pH adjusted with NaOH.

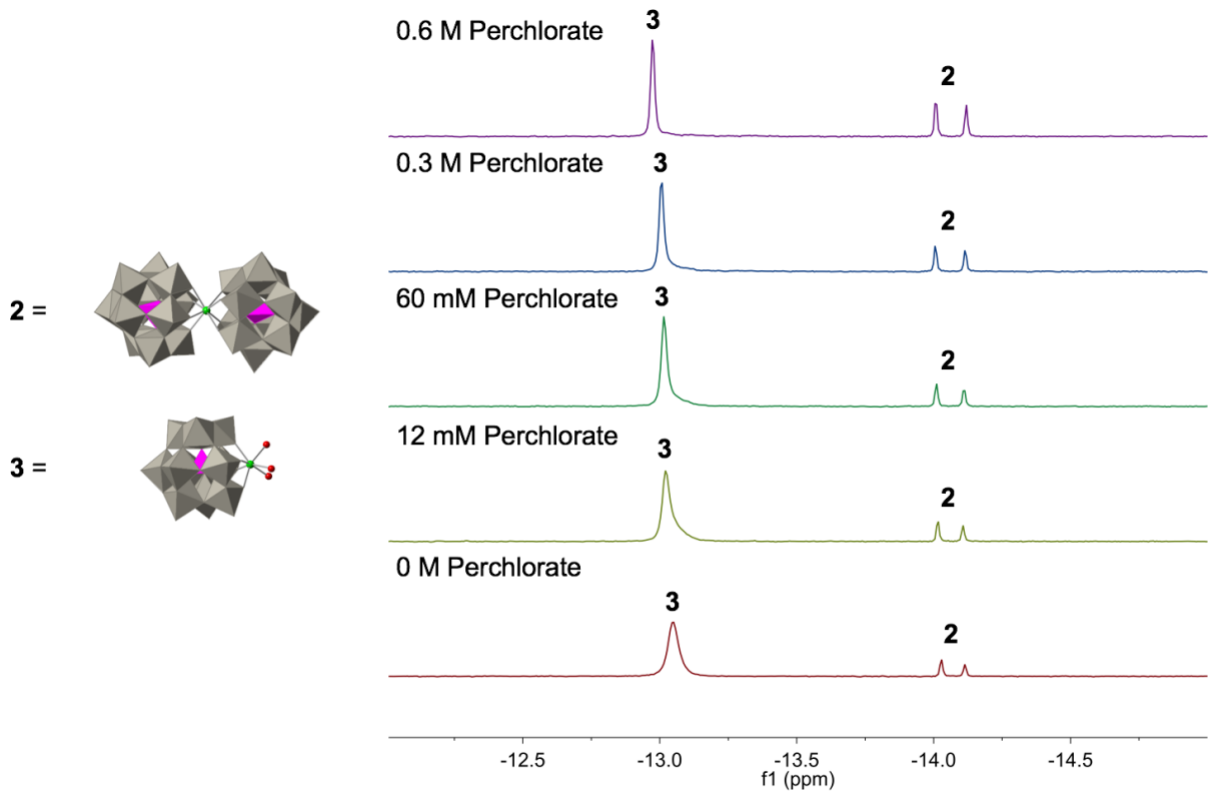

Figure 2.14. ^{31}P NMR spectra of 2.5 mM **1** at pH 4.8 in varying concentrations of $NaClO_4$. Solutions were pH adjusted with NaOH (600 MHz NMR, 1024 scans, 85% H_3PO_4). Polyhedral representation **2** is based on a known crystal structure while **3** is a cartoon of the likely structure present in solution.

To account for effect of ionic strength, buffered and unbuffered catalytic reactions were compared while maintaining a constant ionic strength by adding the appropriate amount of $NaClO_4$. After 115 hours, when the 0.5 M acetate buffered solution had reached 99% conversion of DMNP, the pH was recorded (Table 2.3). As expected, the solution with the highest buffer concentration showed almost no change in pH, while the unbuffered solution dropped appreciably from pH 4.86 to 2.80. Significantly, however, the initial rates were not equal, with the initial rate increasing as a function of buffer concentration (Figure 2.15). To understand this

phenomenon further, the impact of varying concentrations of acetate buffer in the reactions catalyzed by **1** was examined by ^{31}P NMR.

Buffer Conc. (M)	pH Before	pH After
0.5	4.82	4.78
0.2	4.78	4.66
0.05	4.75	4.35
0.01	4.79	3.37
0	4.86	2.80

Table 2.3. Change in pH over the course of full DMNP hydrolysis as a function of buffer concentration with 2.5 mM **1**, 10.3 mM DMNP at pH 4.8. Solutions were pH adjusted using NaOH with an ionic strength of 0.3 M which was maintained by addition of $NaClO_4$.

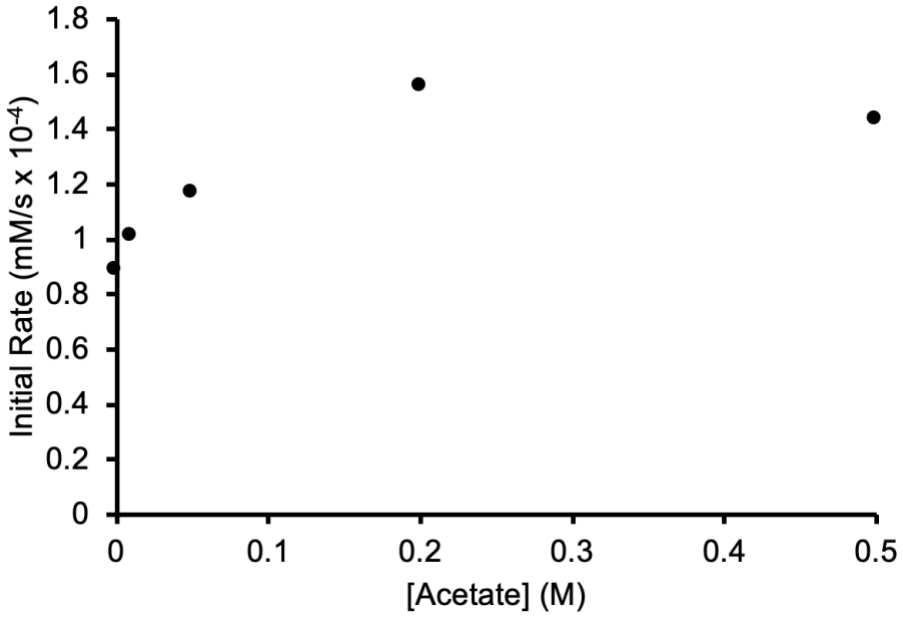

Figure 2.15. Initial rate dependence of DMNP hydrolysis on acetic acid/acetate buffer concentration. Conditions: buffer and $NaClO_4$ concentration varied; ionic strength, 0.3 M (combined effect of acetate and perchlorate ions), 2.5 mM **1**, 10.3 mM DMNP, pH 4.8, pH adjusted with NaOH.

The ^{31}P NMR spectra of **1** show a clear dependence on the acetate buffer concentration present in the solution (Figure 2.16). As the concentration of acetate increases, a new peak grows upfield of the original peak at -13.0 ppm, and the original peak begins to diminish. Both peaks shift upfield concomitant with the increase in acetate concentration. The new peak eventually moves to -13.5 ppm. The formation of this peak is consistent with an acetate ion coordinating to the POM, either by displacing an aqua ligand coordinated to the Zr(IV) center creating a new Zr-acetate species or via hydrogen bonding with one of the zirconium bound water molecules.

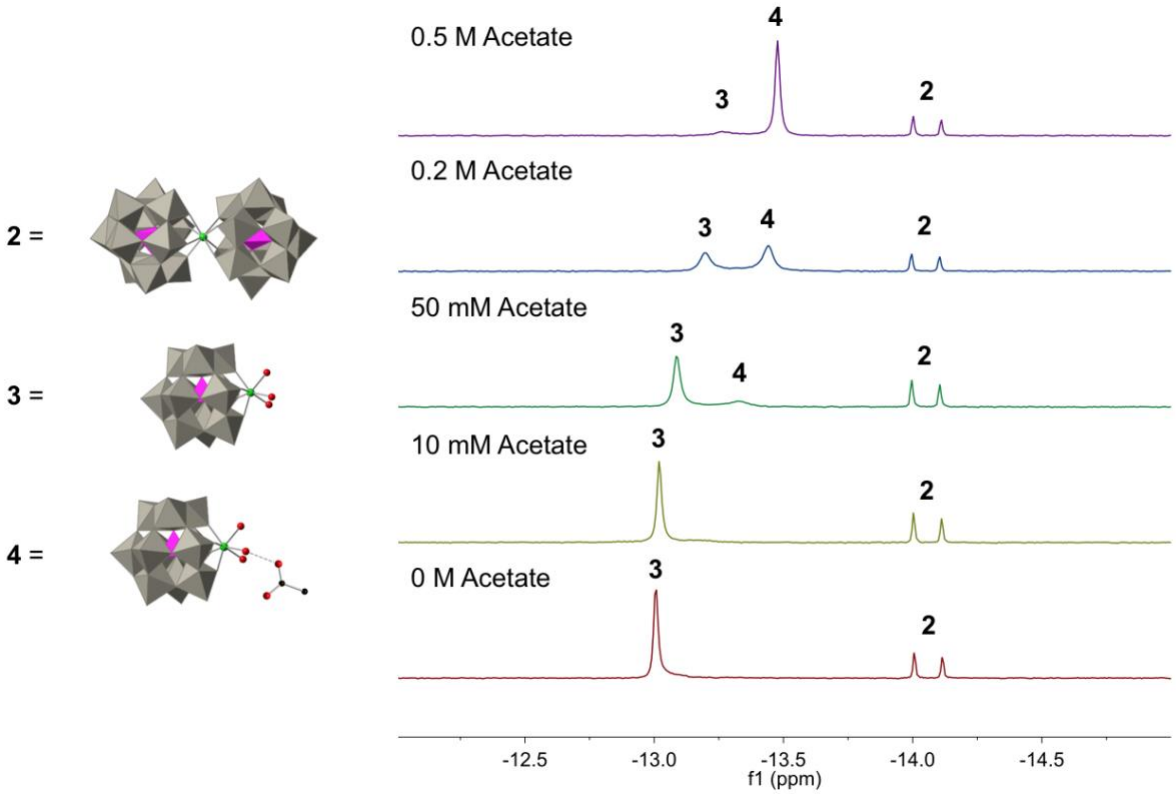

Figure 2.16. ^{31}P NMR spectra of 2.5 mM **1** at pH 4.8 with varying concentrations of acetate buffer. Solutions were pH adjusted with NaOH and maintained at an ionic strength of 0.3 M with $NaClO_4$ (600 MHz NMR, 1024 scans, 85% H_3PO_4 internal standard). Polyhedral

representation **2** is based on a known crystal structure[35] while **3** and **4** are cartoons of the likely structures present in solution.

Two additional lines of evidence indicate that there is coordination between the POM and acetate. First, temperature dependent ^{31}P NMR spectra were collected in 0.2 M acetic acid/acetate where both peaks are present in similar quantities (Figure 2.17). At elevated temperatures the two peaks coalesce into a single peak indicative of a dynamic exchange process occurring at an intermediate rate relative to the NMR timescale.[65] Upon lowering the temperature the two peaks return to their original positions, demonstrating that the reversible change results from a dynamic equilibria rather than a physical change to the material. Second, POM-acetate coordination is further supported by changes to the ^{13}C NMR spectrum of an acetic acid/acetate buffer solution in presence of **1** (Figure 2.18). The carboxylic acid carbon resonance observed at 178.52 in the absence of **1** shifts downfield to 178.64 and broadens from 1.8 to 5.4 Hz, again consistent with a dynamic exchange process. In contrast, the methyl carbon does not shift or broaden appreciably indicating the POM interaction is through the carboxylic acid group.

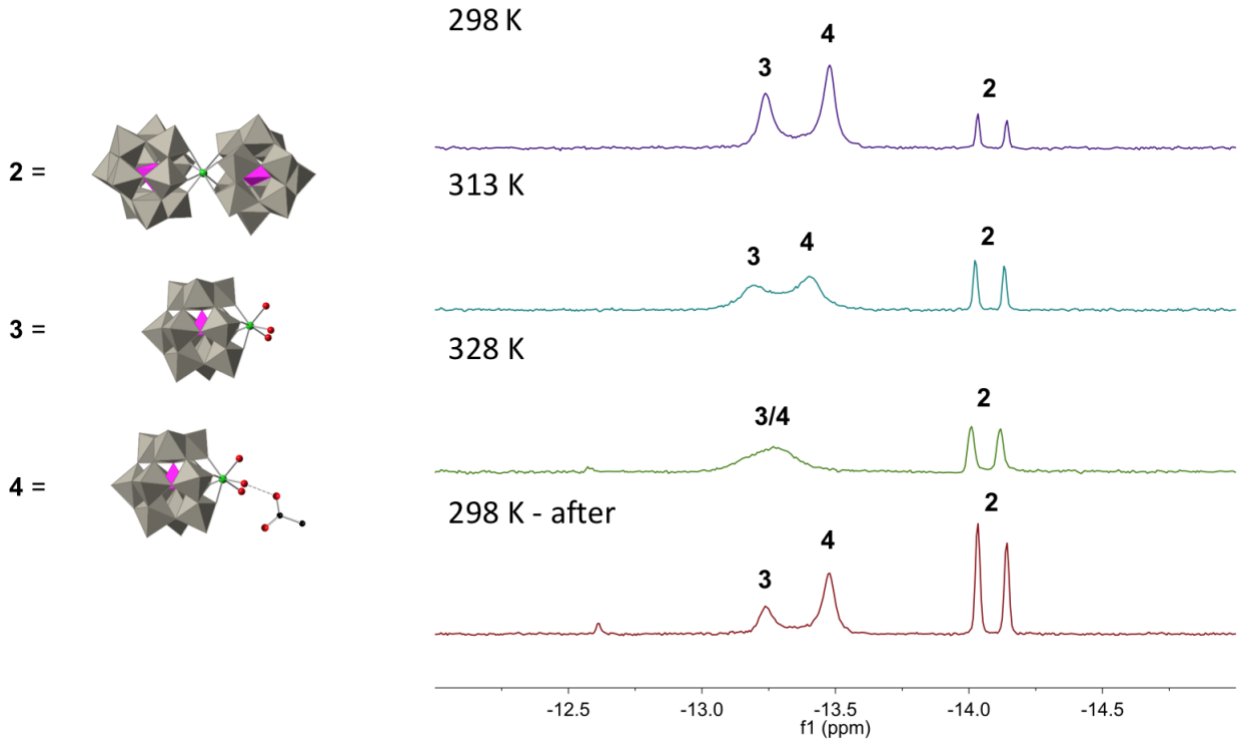

Figure 2.17. ^{31}P NMR spectra of a single solution of 2.5 mM **1** in 0.2 M acetic acid/acetate buffer at different temperatures (600 MHz NMR, 1024 scans, 85% H_3PO_4 internal standard). Spectra are presented in chronological order going from top to bottom. Note the increase in **2** in the last spectrum resulting from prolonged exposure to elevated temperatures used in the previous experiment. Polyhedral representation **2** is based on a known crystal structure[35] while **3** and **4** are cartoons of the likely structures present in solution.

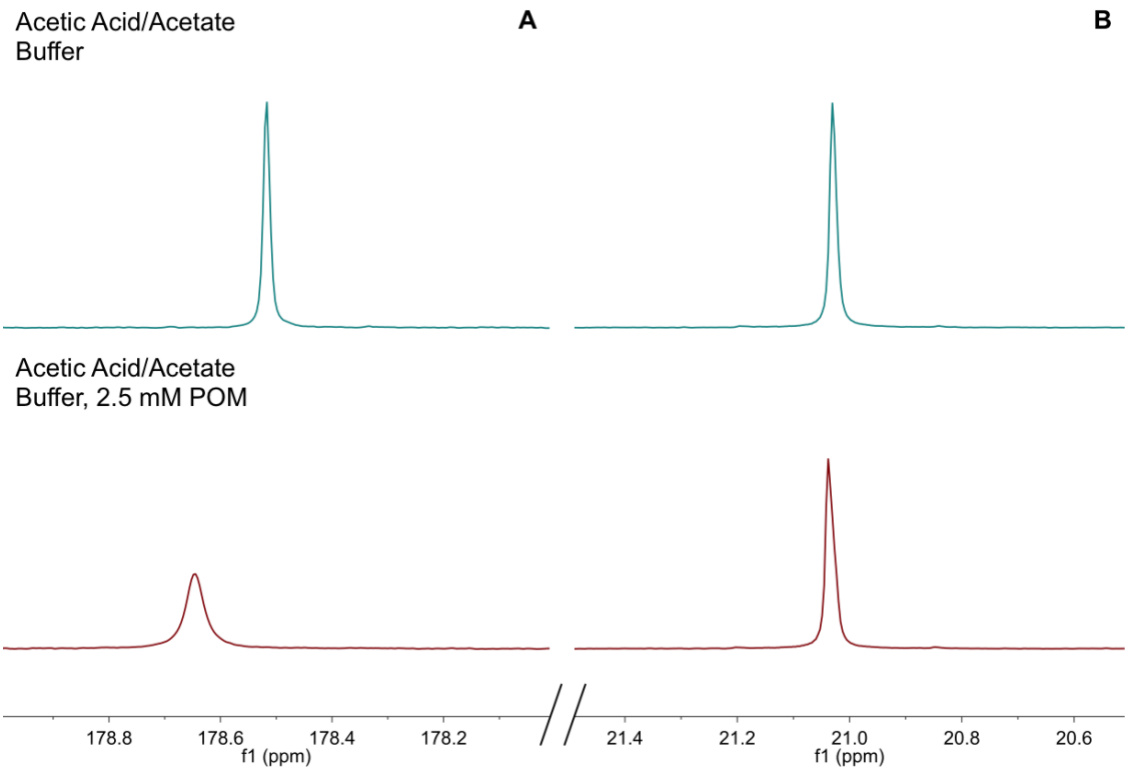

Figure 2.18. ^{13}C NMR of 0.5 M acetic acid/acetate buffer at pH 4.8 (600 MHz NMR, 1024 scans). The downfield region of the spectra (A) corresponds to the carboxylic acid carbon, while the peak around 21 ppm (B) corresponds to the methyl carbon.

In contrast to the NMR resonances corresponding to **3**, the peaks at -14 ppm associated with catalytically-inactive **2** do not shift as a function of acetate concentration. With eight bonds, the Zr center in **2** is coordinatively saturated leaving no open site for binding of an acetate ligand, nor does it have aqua ligands to facilitate hydrogen bonding. Accordingly, there is no chemical shift associated with increasing acetate concentration. To assess catalyst stability in the presence of acetate, ^{31}P NMR spectra were taken of samples aged in acetate buffer both with and without substrate (Figure 2.19). After two weeks, additional **2** forms, however, **3** remains the predominant species. In both the presence and absence of DMNP, **3** shows a similar decrease in

concentration, suggesting that of the presence of DMNP does not affect the speciation or stability of **3** appreciably.

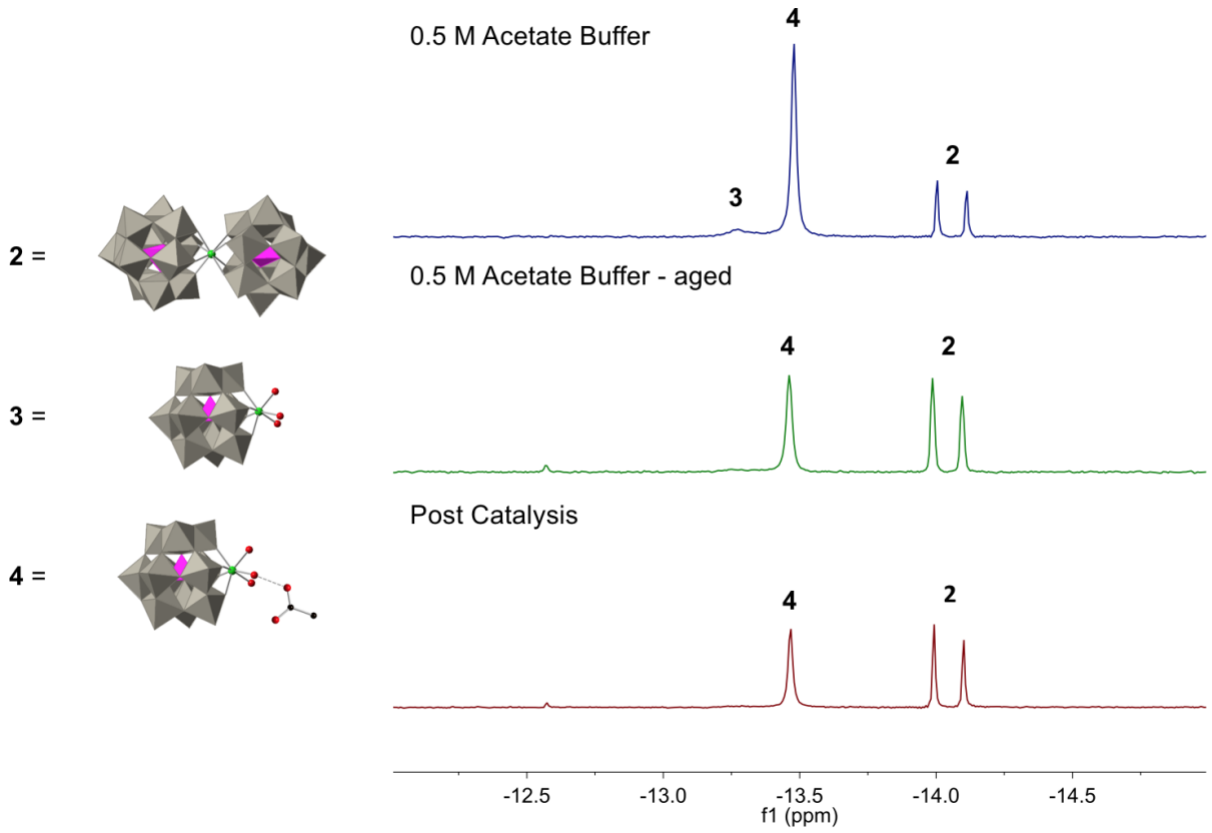

Figure 2.19. ^{31}P NMR spectra of 2.5 mM **1** at pH 4.8 before and after aging for 2 weeks. Solutions were pH adjusted with NaOH. In the post catalysis experiment, 5 mM of DMNP was hydrolyzed (600 MHz NMR, 1024 scans, 85% H_3PO_4). Polyhedral representation **2** is based on a known crystal structure while **3** and **4** are cartoons of the likely structures present in solution.

Based on the interactions between the buffer anion and POM, the observed dependence on the buffer concentration is more easily interpreted. This effect can be attributed to the acetate anion acting as a proximal base making water a more potent nucleophile,[67] or by helping facilitate proton transfer from water to the product in the transition state. In both cases this would lower the barrier for product formation, increasing the reaction rate. To test this

hypothesis, the pH dependence was re-examined while under buffered conditions. Given that the buffer capacity decreases to less than 10% of its maximum at 1 pH unit above or below the pK_a of the buffer, the effect of pH on the reaction rate was examined within this range: pH 3.8 to 5.8. Unlike the unbuffered reaction, here the reaction rate increased with increasing pH (Figure 2.20). This is likely because at the same concentration of buffer there is a higher proportion of acetate anion present at higher pH that can act as a local base. In addition, the presence of acetate bound to zirconium could also affect the pH-dependent dimerization equilibrium, leading to an increased concentration of **3** at higher pH.

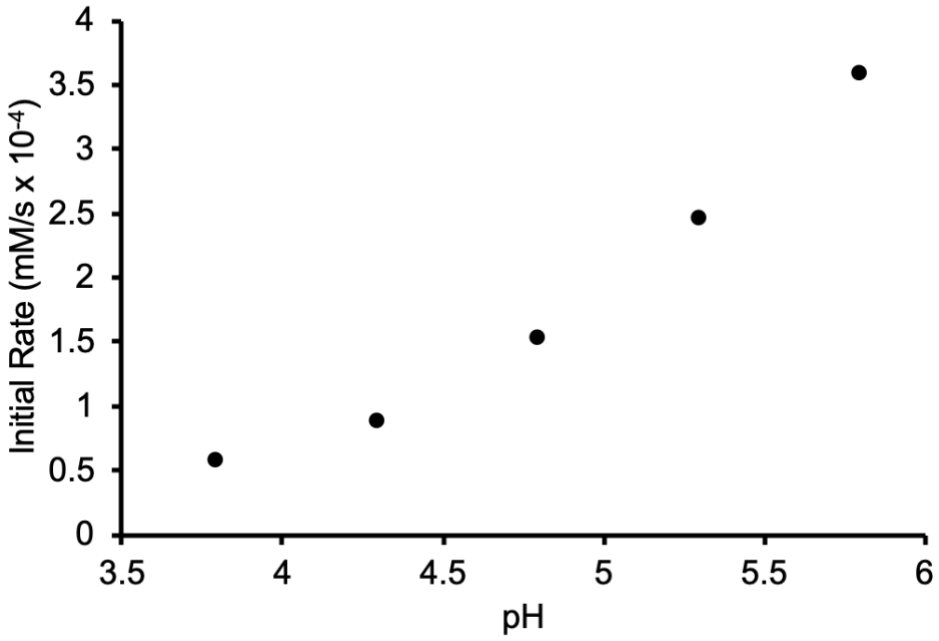

Figure 2.20. Initial catalytic hydrolysis rates as a function of pH. Conditions: 2.5 mM **1** and 10.3 mM DMNP in 0.5 M sodium acetate buffer. Solutions were pH adjusted with NaOH.

With these key findings for the effect of acetate buffer on catalytic hydrolysis by **1**, another buffer, phosphate, was examined as it is a common buffer for POM reactions in aqueous media and for hydrolysis reactions in general. While phosphate does not buffer at pH 4.8,

experiments were carried out at this pH nonetheless to keep POM speciation constant. The ^{31}P NMR spectra show that as with acetate, there is a chemical shift of the POM resonance upfield in the presence of phosphate indicating the formation of a complex with **3** (Figures 2.21 and 2.22). Additional evidence of complexation exists in the phosphate region of the spectrum where a new peak grows in upfield of free phosphate as the POM concentration is increased. The peak is attributed to the phosphate molecules bound to the POM (Figure 2.23). In stark contrast with the acetate-buffered reactions, a solution with 0.3 M phosphate reduced the activity of the catalyst by a factor of 13 relative to 0.5 M acetic acid/acetate (Figures 2.24, 2.25, and Table 2.4). A concentration of 0.3 M phosphate was used, as opposed to the 0.5 M used in the case of acetate, so that an ionic strength of 0.3 M would be maintained. This finding is consistent with a significantly different interaction mode of phosphate versus acetate with Zr(IV). It is likely that monobasic sodium phosphate competes with DMNP for binding to the zirconium center thus slowing reactivity, whereas acetate does not.

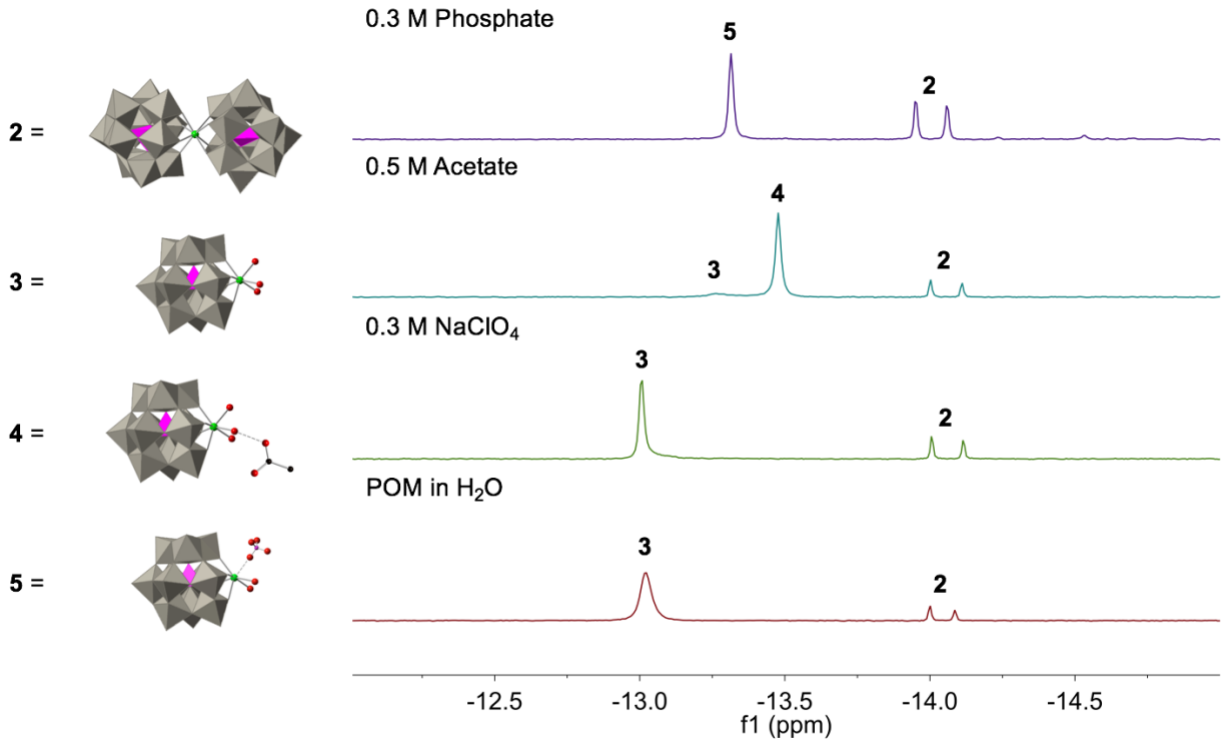

Figure 2.21. ^{31}P NMR spectra of 2.5 mM **1** at pH 4.8 in the presence of different anions. Solutions were pH adjusted with NaOH (600 MHz NMR, 1024 scans, 85% H_3PO_4). Polyhedral representation **2** is based on a known crystal structure while **3**, **4**, and **5** are cartoons of the likely structures present in solution.

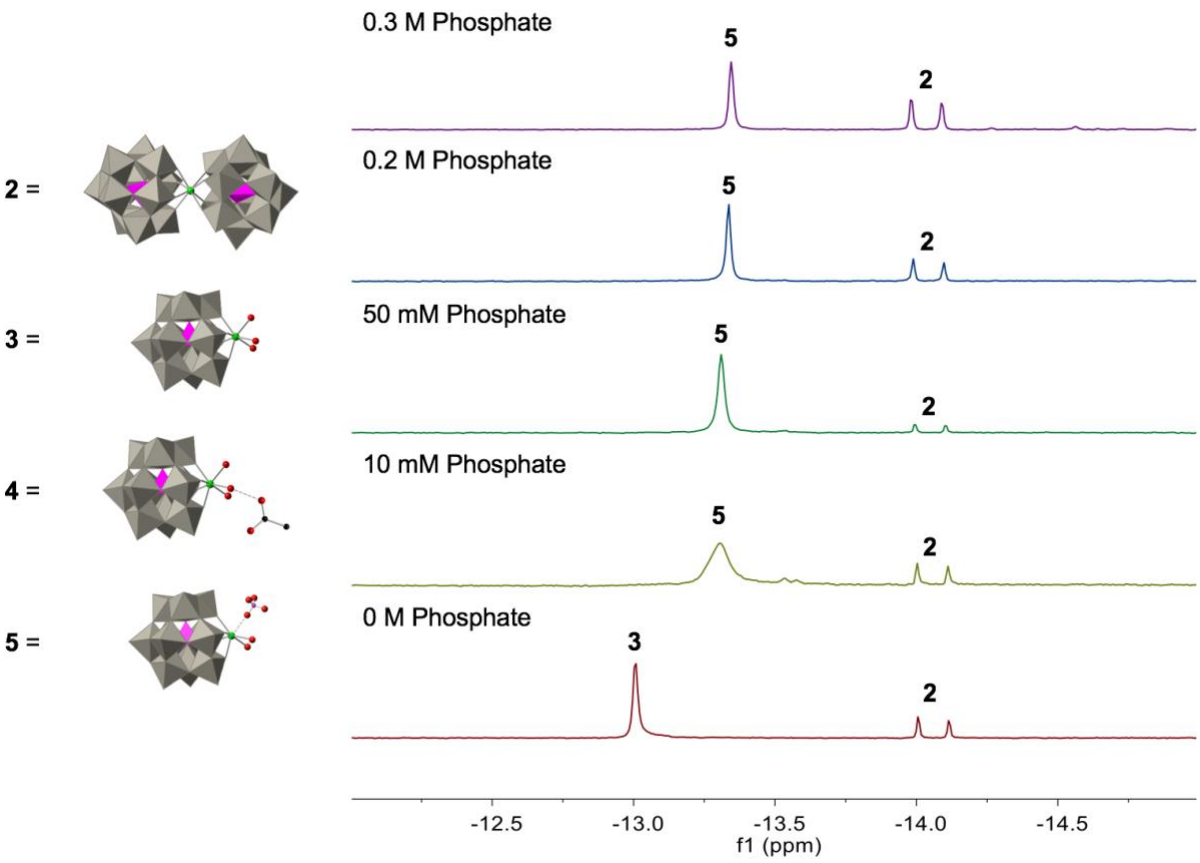

Figure 2.22. ^{31}P NMR spectra of 2.5 mM **1** at pH 4.8 in the presence of varying concentrations of $H_2PO_4^-$. Solutions were pH adjusted with NaOH (600 MHz NMR, 1024 scans, 85% H_3PO_4 internal standard). Polyhedral representation **2** is based on a known crystal structure while **3**, **4**, and **5** are cartoons of the likely structures present in solution.

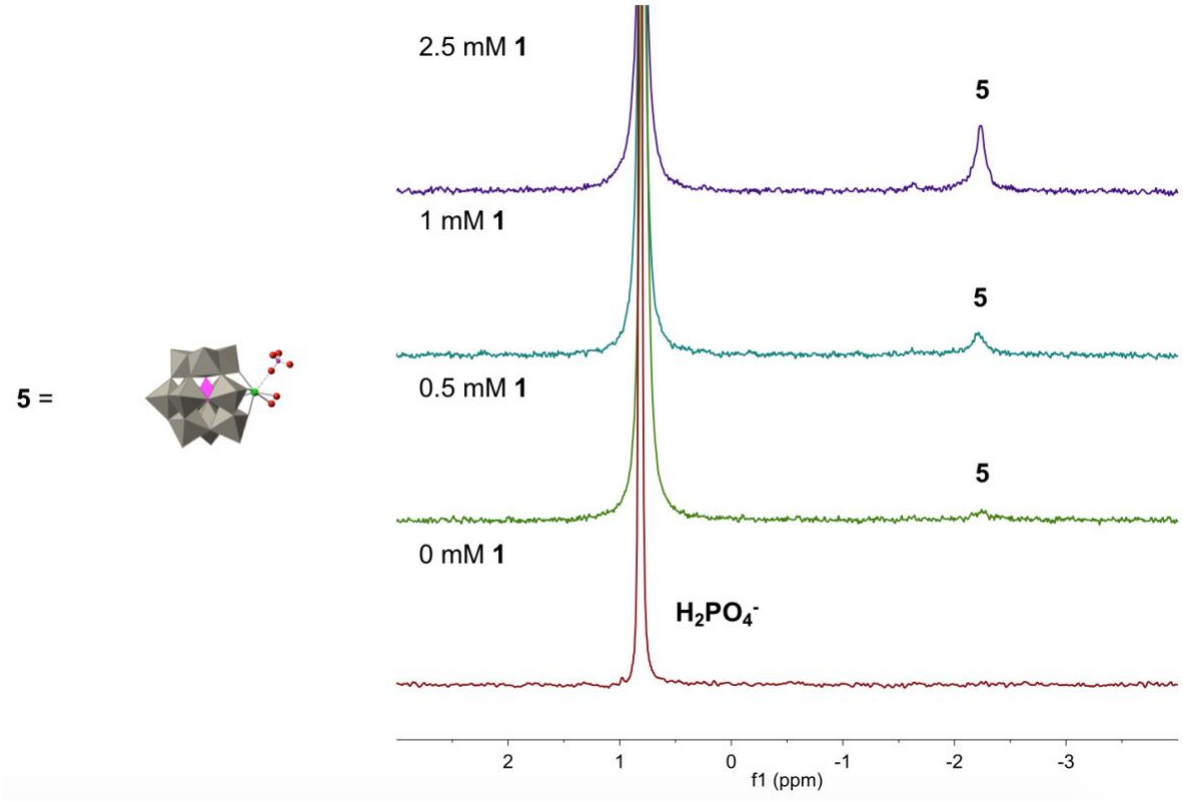

Figure 2.23. ^{31}P NMR of 10 mM NaH_2PO_4 with increasing concentrations of **1**. Solutions were pH adjusted with NaOH (600 MHz NMR, 1024 scans, 85% H_3PO_4 int. std). Polyhedral representation **5** is a cartoon of the likely structure present in solution.

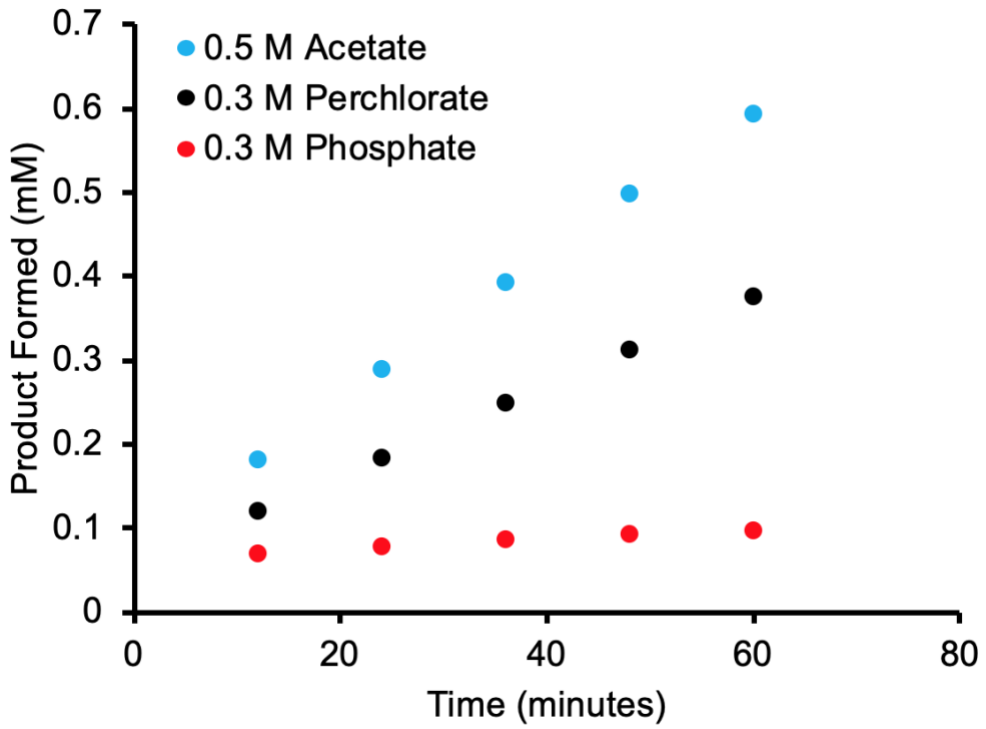

Figure 2.24. Product formation as a function of time in the presence of different anions. Acetate (blue) shows an enhancement over perchlorate (non-coordinating), whereas phosphate (red) exhibits inhibition. Conditions: Ionic strength of 0.3 M, 2.5 mM **1**, 10.3 mM DMNP, pH 4.8, pH adjusted with NaOH.

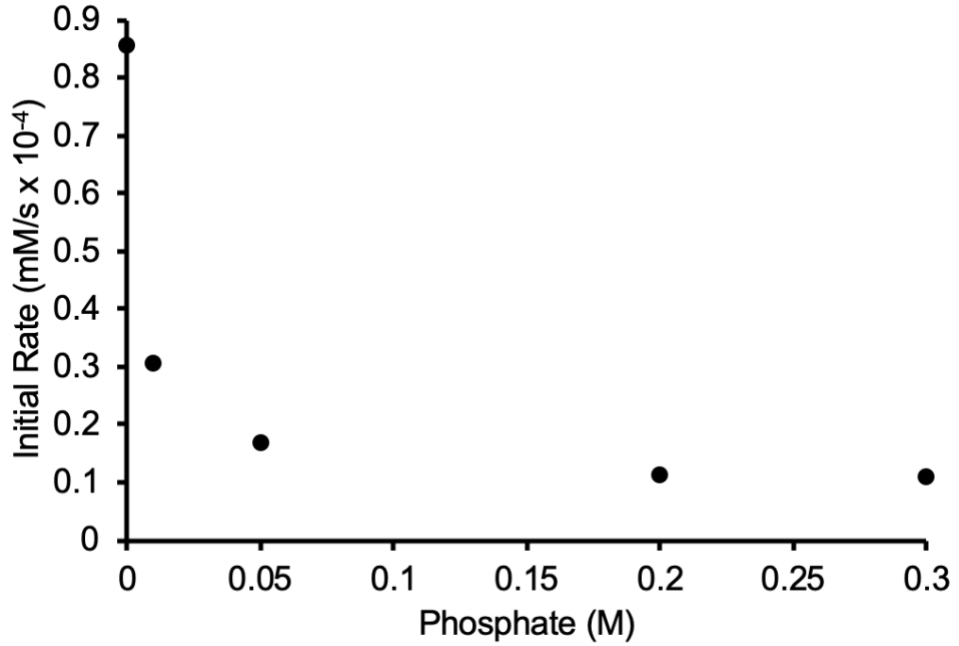

Figure 2.25. Initial catalytic hydrolysis rates as a function of $H_2PO_4^-$ concentration with 2.5 mM **1** and 10.3 mM DMNP at a constant ionic strength of 0.3 M. Solutions were pH adjusted with NaOH.

Conditions	**Initial Rate (nM/s)**
0.3 M $NaClO_4$, 2.5 mM **1**	102
0.5 M Acetate Buffer, 2.5 mM **1**	144
0.5 M Acetate Buffer	3.2
0.3 M $NaH_2PO_4^-$, 2.5 mM **1**	11
0.3 M MPA, 2.5 mM **1**	19.7

Table 2.4. Initial rates of hydrolysis of 10.3 mM DMNP at pH 4.8 with an ionic strength of 0.3 M (buffer or electrolyte), pH adjusted with $HClO_4$ or NaOH.

To support these experimental findings, density functional theory (DFT) computational studies were conducted. DFT studies (see Supporting Information for details) provide clear insight into distinct binding modes and associated energetics of these two widely used buffers for hydrolysis reactions (Figure 2.26). The calculations predict that $H_2PO_4^-$ indeed does bind

directly to the Zr center which explains the loss of activity relative to the non-nucleophilic and non-basic ClO_4^-, which NMR spectra confirm does not interact strongly with the POM (Figure 2.14). In the case of acetate, the zirconium center remains open to substrate binding as acetate is predicted to bind in a non-competitive mode to the POM by hydrogen bonding to a Zr-based aqua ligand. For comparison, direct coordination with the Zr center is higher in energy and thus less favorable (Figure 2.27).

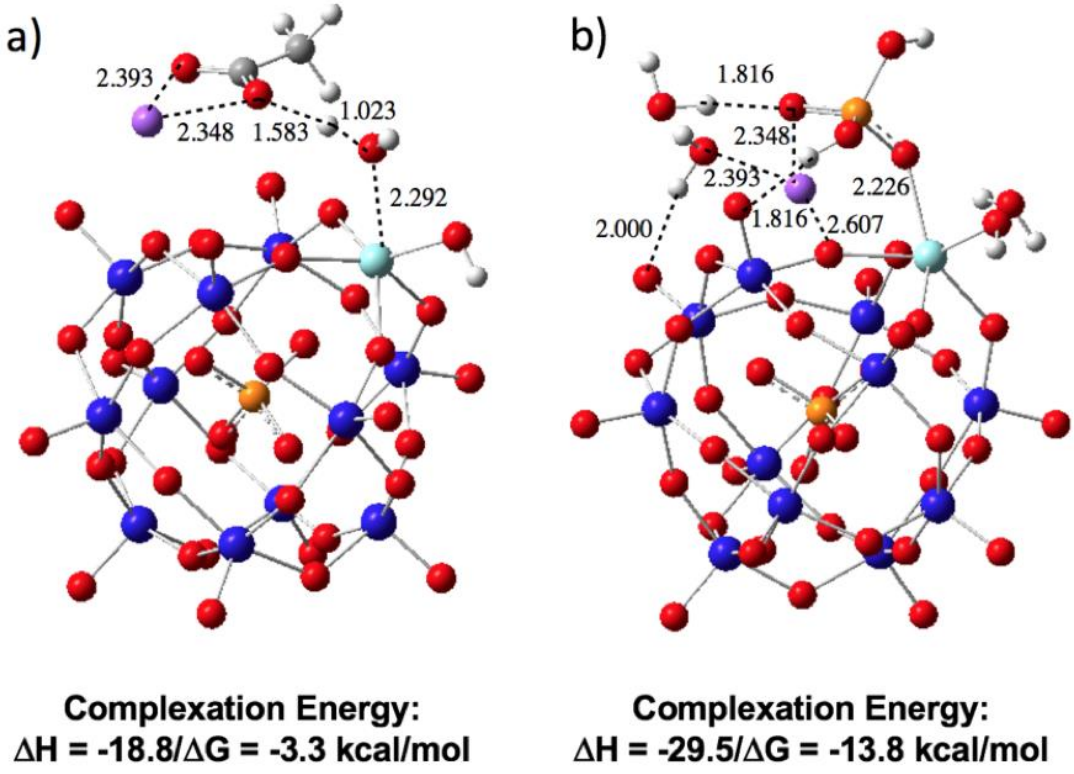

Figure 2.26. Comparison of the complexation energies and geometries between the POM monomer, **3**, and the anions acetate (a), and phosphate (b). W, blue; O, red; Zr, blue-green; Na, purple; C, grey; P, orange; H, white.

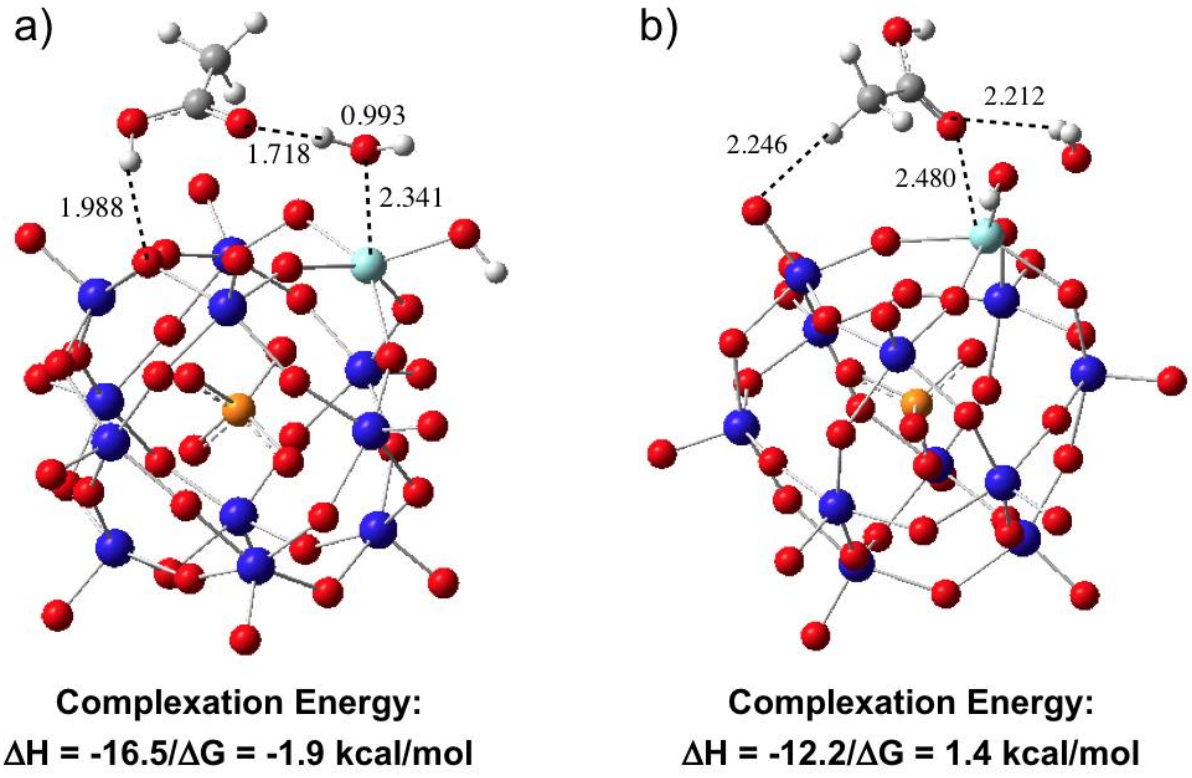

Figure 2.27. Comparison of the complexation energies and geometries between the POM monomer, **3**, and acetate bound indirectly (a) and directly (b). W, blue; O, red; Zr, blue-green; C, grey; P, orange; H, white.

The indirect binding mode of acetate to the catalytically active zirconium likely provides the hydrolysis rate enhancement via both proposed mechanisms described above: acting as a local base and/or shifting the dimerization equilibrium in favor of the more active monomer. Figure 2.26a shows an increase in the O-H bond length of the aqua ligand hydrogen bonded to acetate. For this water molecule one O-H bond distance is 0.969 Å, matching the typical length for a water O-H bond, while the second O-H bond has increased to 1.023 Å. This provides evidence that acetate, through hydrogen bonding with water, can act as a local base by pulling the hydrogen atom away from water making it more hydroxide like, and thus a better

nucleophile. Calculations suggest this occurs when the zirconium center in **3** has both a free coordination position and an aqua ligand (Figure 2.28).

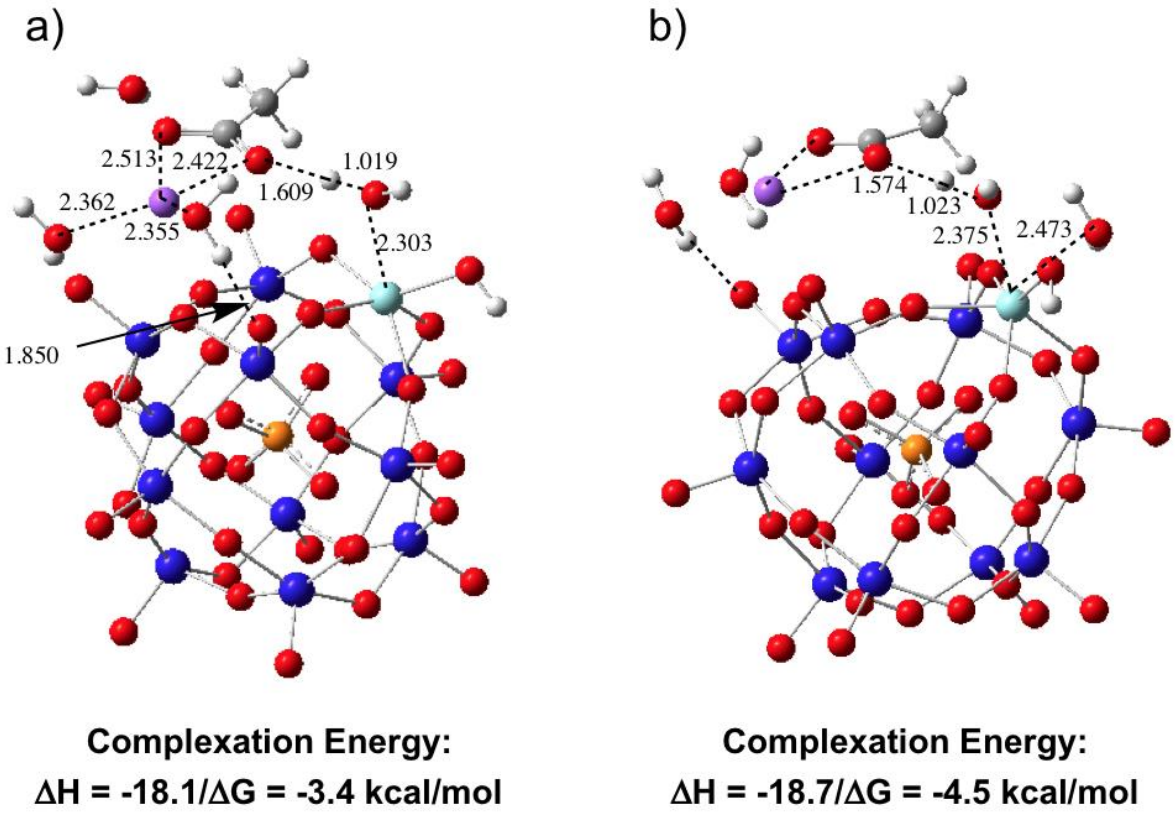

Figure 2.28. Comparison of the complexation energies and geometries between the POM monomer, **3**, and acetate bound through water with an open Zr coordination site (a) and no open coordination site (b). W, blue; O, red; Zr, blue-green; Na, purple; C, grey; P, orange; H, white.

Based on the above understanding of the interaction between **3** and $NaH_2PO_4^-$, a logical next step was to look at catalyst poisoning by the nerve agent hydrolysis product, MPA. Via ^{31}P NMR, we see that, as with both acetate and phosphate, the POM resonance shifts upfield in the presence of MPA (Figure 2.29). The initial rates of hydrolysis as a function of MPA show that, similar to phosphate, there is inhibition of the reaction (Figure 2.30). This suggests that the binding of MPA happens in competition with DMNP, significantly slowing the reaction.

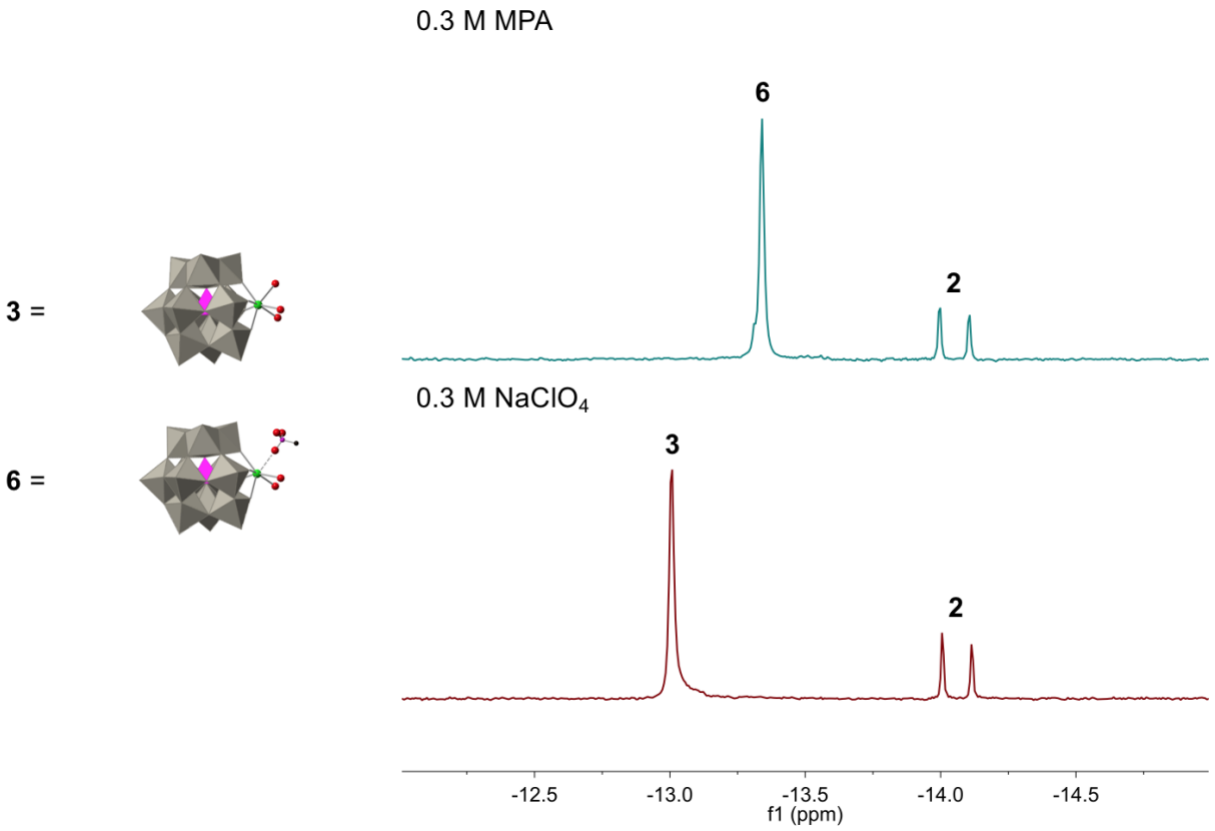

Figure 2.29. ^{31}P NMR of 2.5 mM **1** at pH 4.8 with an ionic strength of 0.3 M. Solutions were pH adjusted with NaOH (600 MHz NMR, 1024 scans, 85% H_3PO_4). Polyhedral representations **3** and **5** are cartoons of the likely structures present in solution. Polyhedral representation **2** is based on a known crystal structure while **6** is a cartoon of the likely structure present in solution.

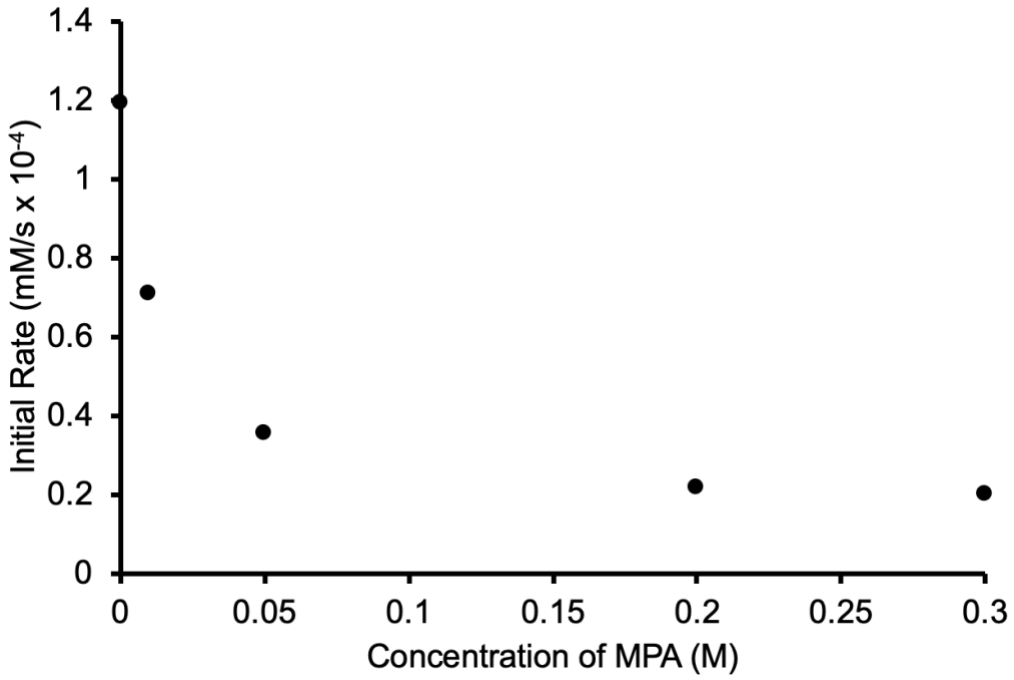

Figure 2.30. Initial rate dependence of DMNP hydrolysis on MPA concentration. Conditions: MPA and $NaClO_4$ concentration varied; ionic strength, 0.3 M (combined effect of MPA and perchlorate ions), 2.5 mM **1**, 10.3 mM DMNP, pH 4.8, pH adjusted with NaOH.

In light of the large number of CWA hydrolysis studies involving N-ethylmorpholine (NEM) as a buffer,[7, 9, 10, 13, 49, 68] the effect of a morpholine based buffer was also examined here. The compound 2-(*N*-morpholino)ethanesulfonic acid (MES) was chosen as it is very similar in structure to NEM, but it has a lower pK_a of 6.16 allowing it to buffer at pH values at which both **1** and **3** will be present in solution. A pH of 5.8 was chosen to maximize both the concentration of **3** and deprotonated MES as a means to probe the effect of a local nucleophile/base in solution. Interestingly, the initial rate of hydrolysis was effectively independent of MES concentration while maintaining a constant ionic strength (Figure 2.31). The ^{31}P NMR shows that in the presence and absence of MES there is no change in the chemical shift of the POM indicating there is little or no interaction with MES (Figure 2.32). Thus, the MES is not involved in the rate

limiting step. Future studies will continue to examine other buffer molecules to further develop the relationship between buffer-catalyst interaction and observed hydrolysis chemistry.

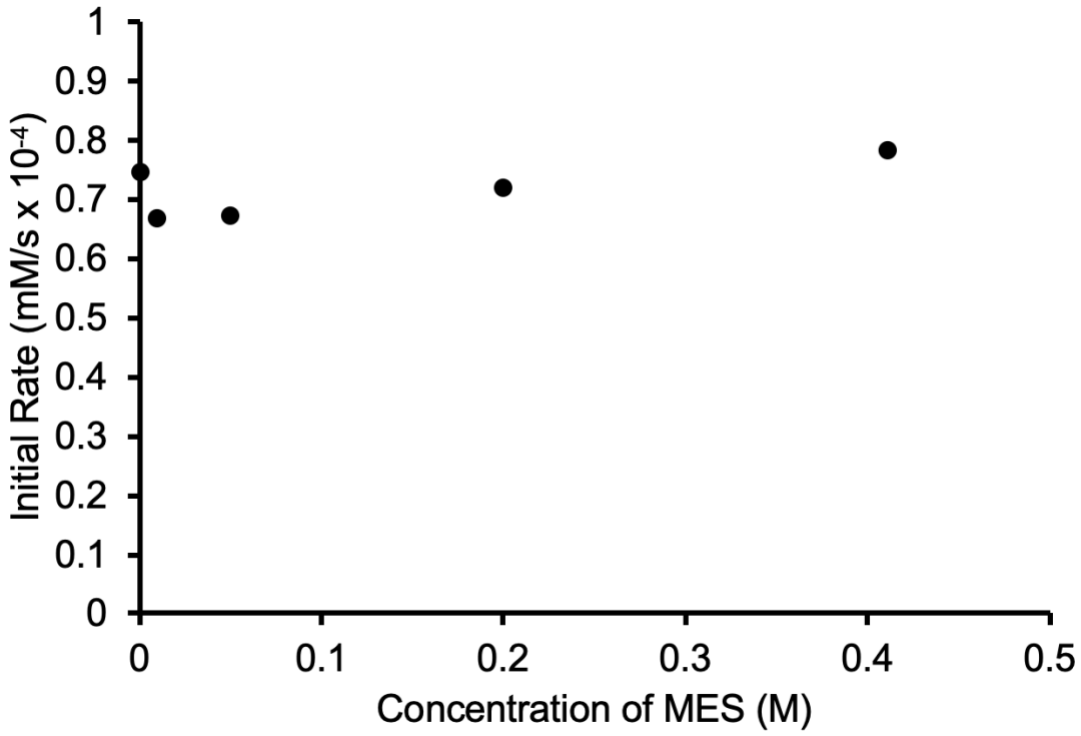

Figure 2.31. Initial rate dependence of DMNP hydrolysis as a function of MES concentration. Conditions: MES and $NaClO_4$ concentration varied; ionic strength, 0.3 M (combined effect of MES and perchlorate ions), 2.5 mM **1**, 10.3 mM DMNP, pH 5.8, pH adjusted with NaOH.

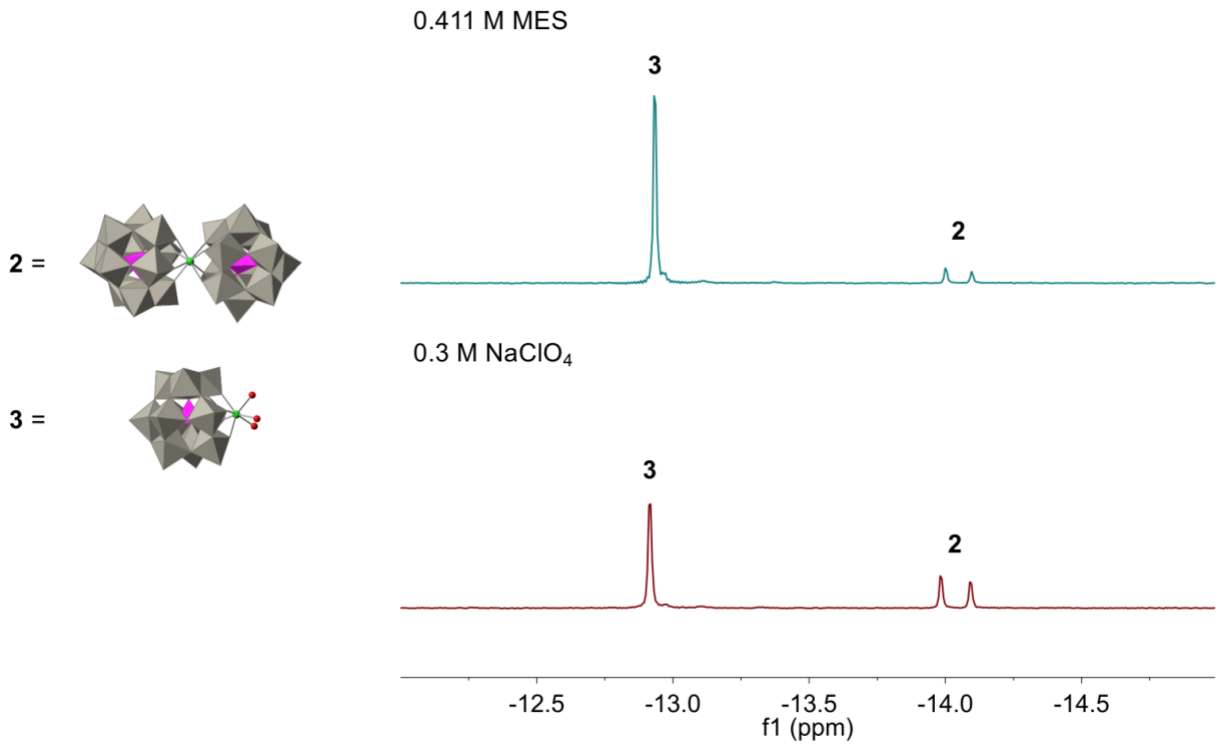

Figure 2.32. ^{31}P NMR of 2.5 mM **1** at pH 5.8 with an ionic strength of 0.3 M. Solutions were pH adjusted with NaOH (600 MHz NMR, 1024 scans, 85% H_3PO_4). Polyhedral representation **2** is based on a known crystal structure while **3** is a cartoon of the likely structure present in solution.

2.4 Conclusions

This is the first report of an electrophilic Zr-substituted POM catalytically hydrolyzing a CWA simulant at near-neutral pH. This study also reveals that buffer anions, often thought to be relatively innocent in CWA hydrolyses, can play key roles in such reactions either accelerating (co-catalyzing) or inhibiting the rate. This effect results from their direct interaction with the catalyst in solution. Other buffer ions, such as MES, that are non-coordinating have no effect on the rate of hydrolysis. Future work will expand on this relationship between buffer-catalyst coordination and its impact on catalyzed hydrolysis rates. Lastly, the nerve agent hydrolysis

product, methyl phosphonic acid (MPA), shows inhibition of **1**-catalyzed hydrolyses. Because this POM has structural similarities to many of the Zr-based heterogeneous systems, which also experience similar product inhibition, this system provides a good means of probing and potentially studying the reversal of such inhibition. This will have important implications on the poisoning and long-term use of all Zr-based CWA hydrolysis catalysts.

2.5 References

1. Yang, Y. C.; Baker, J. A.; Ward, J. R., Decontamination of chemical warfare agents. *Chem. Rev.* **1992,** *92* (8), 1729-1743.

2. Smith, B. M., Catalytic methods for the destruction of chemical warfare agents under ambient conditions. *Chem. Soc. Rev.* **2008,** *37* (3), 470-478.

3. Jang, Y. J.; Kim, K.; Tsay, O. G.; Atwood, D. A.; Churchill, D. G., Update 1 of: Destruction and Detection of Chemical Warfare Agents. *Chem. Rev.* **2015,** *115* (24), PR1-PR76.

4. Kinnan, M. K.; Creasy, W. R.; Fullmer, L. B.; Schreuder-Gibson, H. L.; Nyman, M., Nerve Agent Degradation with Polyoxoniobates. *Eur. J. Inorg. Chem.* **2014,** *2014* (14), 2361-2367.

5. López-Maya, E.; Montoro, C.; Rodríguez-Albelo, L. M.; Aznar Cervantes, S. D.; Lozano-Pérez, A. A.; Cenís, J. L.; Barea, E.; Navarro, J. A. R., Textile/Metal–Organic-Framework Composites as Self-Detoxifying Filters for Chemical-Warfare Agents. *Angew. Chem. Int. Ed.* **2015,** *54* (23), 6790-6794.

6. DeCoste, J. B.; Peterson, G. W., Metal–Organic Frameworks for Air Purification of Toxic Chemicals. *Chem. Rev.* **2014,** *114* (11), 5695-5727.

7. Katz, M. J.; Mondloch, J. E.; Totten, R. K.; Park, J. K.; Nguyen, S. T.; Farha, O. K.; Hupp, J. T., Simple and Compelling Biomimetic Metal–Organic Framework Catalyst for the Degradation of Nerve Agent Simulants. *Angew. Chem. Int. Ed.* **2014,** *53* (2), 497-501.

8. Katz, M. J.; Moon, S.-Y.; Mondloch, J. E.; Beyzavi, M. H.; Stephenson, C. J.; Hupp, J. T.; Farha, O. K., Exploiting parameter space in MOFs: a 20-fold enhancement of phosphate-ester hydrolysis with UiO-66-NH_2. *Chem. Sci.* **2015,** *6* (4), 2286-2291.

9. Mondloch, J. E.; Katz, M. J.; Isley Iii, W. C.; Ghosh, P.; Liao, P.; Bury, W.; Wagner, G. W.; Hall, M. G.; DeCoste, J. B.; Peterson, G. W.; Snurr, R. Q.; Cramer, C. J.; Hupp, J. T.; Farha, O. K., Destruction of chemical warfare agents using metal–organic frameworks. *Nat Mater* **2015,** *14* (5), 512-516.

10. Moon, S.-Y.; Liu, Y.; Hupp, J. T.; Farha, O. K., Instantaneous Hydrolysis of Nerve-Agent Simulants with a Six-Connected Zirconium-Based Metal–Organic Framework. *Angew. Chem. Int. Ed.* **2015,** *54* (23), 6795-6799.

11. Yang, D.; Bernales, V.; Islamoglu, T.; Farha, O. K.; Hupp, J. T.; Cramer, C. J.; Gagliardi, L.; Gates, B. C., Tuning the Surface Chemistry of Metal Organic Framework Nodes: Proton Topology of the Metal-Oxide-Like Zr_6 Nodes of UiO-66 and NU-1000. *J. Am. Chem. Soc.* **2016,** *138* (46), 15189-15196.

12. Moon, S.-Y.; Howarth, A. J.; Wang, T.; Vermeulen, N. A.; Hupp, J. T.; Farha, O. K., A visually detectable pH responsive zirconium metal-organic framework. *Chemical Communications* **2016,** *52* (16), 3438-3441.

13. Islamoglu, T.; Atilgan, A.; Moon, S.-Y.; Peterson, G. W.; DeCoste, J. B.; Hall, M.; Hupp, J. T.; Farha, O. K., Cerium(IV) vs Zirconium(IV) Based Metal–Organic Frameworks for Detoxification of a Nerve Agent. *Chem. Mater.* **2017,** *29* (7), 2672–2675.

14. Balow, R. B.; Lundin, J. G.; Daniels, G. C.; Gordon, W. O.; McEntee, M.; Peterson, G. W.; Wynne, J. H.; Pehrsson, P. E., Environmental Effects on Zirconium Hydroxide Nanoparticles and Chemical Warfare Agent Decomposition: Implications of Atmospheric Water and Carbon Dioxide. *ACS Appl. Mater. Interfaces* **2017,** *9* (45), 39747-39757.

15. Troya, D., Reaction Mechanism of Nerve-Agent Decomposition with Zr-Based Metal Organic Frameworks. *J. Phys. Chem. C* **2016,** *120* (51), 29312-29323.

16. Plonka, A. M.; Wang, Q.; Gordon, W. O.; Balboa, A.; Troya, D.; Guo, W.; Sharp, C. H.; Senanayake, S. D.; Morris, J. R.; Hill, C. L.; Frenkel, A. I., In Situ Probes of Capture and Decomposition of Chemical Warfare Agent Simulants by Zr-Based Metal Organic Frameworks. *J. Am. Chem. Soc.* **2017,** *139* (2), 599-602.

17. Wang, G.; Sharp, C.; Plonka, A. M.; Wang, Q.; Frenkel, A. I.; Guo, W.; Hill, C.; Smith, C.; Kollar, J.; Troya, D.; Morris, J. R., Mechanism and Kinetics for Reaction of the Chemical Warfare Agent Simulant, DMMP(g), with Zirconium(IV) MOFs: An Ultrahigh-Vacuum and DFT Study. *J. Phys. Chem. C* **2017,** *121* (21), 11261-11272.

18. Nomiya, K.; Saku, Y.; Yamada, S.; Takahashi, W.; Sekiya, H.; Shinohara, A.; Ishimaru, M.; Sakai, Y., Synthesis and structure of dinuclear hafnium(IV) and zirconium(IV) complexes sandwiched between 2 mono-lacunary α-Keggin polyoxometalates. *Dalton Trans.* **2009,** (28), 5504-5511.

19. Ly, H. G. T.; Absillis, G.; Parac-Vogt, T. N., Amide bond hydrolysis in peptides and cyclic peptides catalyzed by a dimeric Zr(iv)-substituted Keggin type polyoxometalate. *Dalton Trans.* **2013,** *42* (30), 10929-10938.

20. Luong, T. K. N.; Absillis, G.; Shestakova, P.; Parac-Vogt, T. N., Solution Speciation of the Dinuclear ZrIV-Substituted Keggin Polyoxometalate $[\{\alpha\text{-}PW_{11}O_{39}Zr(\mu\text{-}OH)(H_2O)\}_2]^{8-}$ and

Its Reactivity towards DNA-Model Phosphodiester Hydrolysis. *Eur. J. Inorg. Chem.* **2014,** *2014* (31), 5276-5284.

21. Luong, T. K. N.; Absillis, G.; Shestakova, P.; Parac-Vogt, T. N., Hydrolysis of the RNA model substrate catalyzed by a binuclear ZrIV-substituted Keggin polyoxometalate. *Dalton Trans.* **2015,** *44* (35), 15690-15696.

22. Luong, T. K. N.; Shestakova , P.; Mihaylov, T. T.; Absillis, G.; Pierloot, K.; Parac-Vogt, T. N., Multinuclear Diffusion NMR Spectroscopy and DFT Modeling: A Powerful Combination for Unraveling the Mechanism of Phosphoester Bond Hydrolysis Catalyzed by Metal-Substituted Polyoxometalates. *Chemistry – A European Journal* **2015,** *21* (11), 4428-4439.

23. Luong, T. K. N.; Shestakova, P.; Absillis, G.; Parac-Vogt, T. N., Detailed Mechanism of Phosphoanhydride Bond Hydrolysis Promoted by a Binuclear ZrIV-Substituted Keggin Polyoxometalate Elucidated by a Combination of ^{31}P, ^{31}P DOSY, and ^{31}P EXSY NMR Spectroscopy. *Inorganic Chemistry* **2016,** *55* (10), 4864-4873.

24. Mihaylov, T. T.; Ly, H. G. T.; Pierloot, K.; Parac-Vogt, T. N., Molecular Insight from DFT Computations and Kinetic Measurements into the Steric Factors Influencing Peptide Bond Hydrolysis Catalyzed by a Dimeric Zr(IV)-Substituted Keggin Type Polyoxometalate. *Inorganic Chemistry* **2016,** *55* (18), 9316-9328.

25. Pope, M. T., 4.10 - Polyoxo Anions: Synthesis and Structure A2 - McCleverty, Jon A. In *Comprehensive Coordination Chemistry II*, Meyer, T. J., Ed. Pergamon: Oxford, 2003; pp 635-678.

26. Hill, C. L., Introduction: PolyoxometalatesMulticomponent Molecular Vehicles To Probe Fundamental Issues and Practical Problems. *Chem. Rev.* **1998,** *98* (1), 1-2.

27. Lv, H.; Geletii, Y. V.; Zhao, C.; Vickers, J. W.; Zhu, G.; Luo, Z.; Song, J.; Lian, T.; Musaev, D. G.; Hill, C. L., Polyoxometalate water oxidation catalysts and the production of green fuel. *Chem. Soc. Rev.* **2012,** *41* (22), 7572-7589.

28. Miras, H. N.; Yan, J.; Long, D.-L.; Cronin, L., Engineering polyoxometalates with emergent properties. *Chem. Soc. Rev.* **2012,** *41* (22), 7403-7430.

29. Guo, W.; Lv, H.; Sullivan, K. P.; Gordon, W. O.; Balboa, A.; Wagner, G. W.; Musaev, D. G.; Bacsa, J.; Hill, C. L., Broad-Spectrum Liquid- and Gas-Phase Decontamination of Chemical Warfare Agents by One-Dimensional Heteropolyniobates. *Angew. Chem. Int. Ed.* **2016,** *55* (26), 7403-7407.

30. Proust, A.; Matt, B.; Villanneau, R.; Guillemot, G.; Gouzerh, P.; Izzet, G., Functionalization and post-functionalization: a step towards polyoxometalate-based materials. *Chem. Soc. Rev.* **2012,** *41* (22), 7605-7622.

31. Lauinger, S. M.; Yin, Q.; Geletii, Y. V.; Hill, C. L., Polyoxometalate Multi-Electron Catalysts in Solar Fuel Production. In *Advances in Inorganic Chemistry: Volume 69. Polyoxometallate Chemistry*, 1st ed.; Cronin, L.; Eldik, R. v., Eds. Elsevier, Oxford, UK 2017; pp 117-154.

32. Li, J.; Güttinger, R.; Moré, R.; Song, F.; Wan, W.; Patzke, G. R., Frontiers of water oxidation: the quest for true catalysts. *Chem. Soc. Rev.* **2017,** *46*, 6124-6147.

33. Weinstock, I. A.; Schreiber, R. E.; Neumann, R., Dioxygen in Polyoxometalate Mediated Reactions. *Chem. Rev.* **2017,** *118* (5), 2680–2717.

34. Long, D.-L.; Tsunashima, R.; Cronin, L., Polyoxometalates: Building Blocks for Functional Nanoscale Systems. *Angew. Chem. Int. Ed.* **2010,** *49*, 1736-1758.

35. Kato, C. N.; Shinohara, A.; Hayashi, K.; Nomiya, K., Syntheses and X-ray Crystal Structures of Zirconium(IV) and Hafnium(IV) Complexes Containing Monovacant Wells−Dawson and Keggin Polyoxotungstates. *Inorganic Chemistry* **2006,** *45* (20), 8108-8119.

36. Bassil, B. S.; Dickman, M. H.; Kortz, U., Synthesis and Structure of Asymmetric Zirconium-Substituted Silicotungstates, $[Zr_6O_2(OH)_4(H_2O)_3(\beta\text{-}SiW_{10}O_{37})_3]^{14-}$ and $[Zr_4O_2(OH)_2(H_2O)_4(\beta\text{-}SiW_{10}O_{37})_2]^{10-}$. *Inorganic Chemistry* **2006,** *45* (6), 2394-2396.

37. Carabineiro, H.; Villanneau, R.; Carrier, X.; Herson, P.; Lemos, F.; Ramôa Ribeiro, F.; Proust, A.; Che, M., Zirconium-Substituted Isopolytungstates: Structural Models for Zirconia-Supported Tungsten Catalysts. *Inorganic Chemistry* **2006,** *45* (5), 1915-1923.

38. Iijima, J.; Ishikawa, E.; Nakamura, Y.; Naruke, H., Synthesis and structural investigation of sandwich polyoxotungstates containing cerium (III/IV) and mono-lacunary Keggin tungstophosphate units. *Inorg. Chim. Acta* **2010,** *363* (7), 1500-1506.

39. Lokeren, L. V.; Cartuyvels, E.; Absillis, G.; Willem, R.; Parac-Vogt, T. N., Phosphoesterase activity of polyoxomolybdates: diffusion ordered NMR spectroscopy as a tool for obtaining insights into the reactivity of polyoxometalate clusters. *Chemical Communications* **2008,** (24), 2774-2776.

40. Steens, N.; Ramadan, A. M.; Absillis, G.; Parac-Vogt, T. N., Hydrolytic cleavage of DNA-model substrates promoted by polyoxovanadates. *Dalton Trans.* **2010,** *39* (2), 585-592.

41. Vanhaecht, S.; Absillis, G.; Parac-Vogt, T. N., Hydrolysis of DNA model substrates catalyzed by metal-substituted Wells-Dawson polyoxometalates. *Dalton Trans.* **2012,** *41* (33), 10028-10034.

42. Absillis, G.; Parac-Vogt, T. N., Peptide Bond Hydrolysis Catalyzed by the Wells–Dawson $Zr(\alpha_2\text{-}P_2W_{17}O_{61})_2$ Polyoxometalate. *Inorganic Chemistry* **2012,** *51* (18), 9902-9910.

43. Stroobants, K.; Moelants, E.; Ly, H. G. T.; Proost, P.; Bartik, K.; Parac-Vogt, T. N., Polyoxometalates as a Novel Class of Artificial Proteases: Selective Hydrolysis of Lysozyme under Physiological pH and Temperature Promoted by a Cerium(IV) Keggin-Type Polyoxometalate. *Chemistry – A European Journal* **2013,** *19* (8), 2848-2858.

44. Stroobants, K.; Absillis, G.; Moelants, E.; Proost, P.; Parac-Vogt, T. N., Regioselective Hydrolysis of Human Serum Albumin by ZrIV-Substituted Polyoxotungstates at the Interface of Positively Charged Protein Surface Patches and Negatively Charged Amino Acid Residues. *Chemistry – A European Journal* **2014,** *20* (14), 3894-3897.

45. Luong, T. K. N.; Shestakova, P.; Parac-Vogt, T. N., Kinetic studies of phosphoester hydrolysis promoted by a dimeric tetrazirconium(iv) Wells-Dawson polyoxometalate. *Dalton Trans.* **2016,** *45* (30), 12174-12180.

46. Ly, H. G. T.; Mihaylov, T.; Absillis, G.; Pierloot, K.; Parac-Vogt, T. N., Reactivity of Dimeric Tetrazirconium(IV) Wells–Dawson Polyoxometalate toward Dipeptide Hydrolysis Studied by a Combined Experimental and Density Functional Theory Approach. *Inorganic Chemistry* **2015,** *54* (23), 11477-11492.

47. Ly, H. G. T.; Absillis, G.; Bajpe, S. R.; Martens, J. A.; Parac-Vogt, T. N., Hydrolysis of Dipeptides Catalyzed by a Zirconium(IV)-Substituted Lindqvist Type Polyoxometalate. *Eur. J. Inorg. Chem.* **2013,** *2013* (26), 4601-4611.

48. Moon, S.-Y.; Proussaloglou, E.; Peterson, G. W.; DeCoste, J. B.; Hall, M. G.; Howarth, A. J.; Hupp, J. T.; Farha, O. K., Detoxification of Chemical Warfare Agents Using a Zr6-Based Metal–Organic Framework/Polymer Mixture. *Chemistry – A European Journal* **2016,** *22* (42), 14864-14868.

49. de Koning, M. C.; van Grol, M.; Breijaert, T., Degradation of Paraoxon and the Chemical Warfare Agents VX, Tabun, and Soman by the Metal–Organic Frameworks UiO-66-NH_2, MOF-808, NU-1000, and PCN-777. *Inorganic Chemistry* **2017,** *56* (19), 11804-11809.

50. Anderson, B. M.; Anderson, C. D., The Effect of Buffers on Nicotinamide Adenine Dinucleotide Hydrolysis. *J. Biol. Chem.* **1963,** *238* (4), 1475-1478.

51. Hegg, E. L.; Burstyn, J. N., Hydrolysis of Unactivated Peptide Bonds by a Macrocyclic Copper(II) Complex: Cu([9]aneN_3)Cl_2 Hydrolyzes Both Dipeptides and Proteins. *J. Am. Chem. Soc.* **1995,** *117* (26), 7015-7016.

52. Groves, J. T.; Baron, L. A., Models of zinc-containing proteases. Catalysis of cobalt(III)-mediated amide hydrolysis by a pendant carboxylate. *J. Am. Chem. Soc.* **1989,** *111* (14), 5442-5448.

53. Miura, Y.-k.; Kamiya, Y., Highly Selective Sorption of Small Polar Molecules by a Nonporous Ionic Crystal of a Lacunary Keggin-type Heteropoly Anion and Alkali Metal Cations. *Chem. Lett.* **2012,** *41* (3), 331-333.

54. Contant, R., Relations entre les tungstophosphates apparentés à l'anion PW12O403−. Synthèse et propriétés d'un nouveau polyoxotungstophosphate lacunaire K10P2W20O70•24H2O. *Can. J. Chem.* **1987,** *65* (3), 568-573.

55. Petříček, V.; Dušek, M.; Palatinus, L., Crystallographic Computing System JANA2006: General features. In *Zeitschrift für Kristallographie - Crystalline Materials*, 2014; Vol. 229, p 345.

56. Bowers, G. N.; McComb, R. B.; Christensen, R. G.; Schaffer, R., High-purity 4-nitrophenol: purification, characterization, and specifications for use as a spectrophotometric reference material. *Clinical Chemistry* **1980,** *26* (6), 724-729.

57. Zhao, Y.; Truhlar, D. G., A new local density functional for main-group thermochemistry, transition metal bonding, thermochemical kinetics, and noncovalent interactions. *J. Chem. Phys.* **2006,** *125* (19), 194101.

58. Hay, P. J.; Wadt, W. R., Ab initio effective core potentials for molecular calculations. Potentials for the transition metal atoms Sc to Hg. *J. Chem. Phys.* **1985,** *82* (1), 270-283.

59. Hay, P. J.; Wadt, W. R., Ab initio effective core potentials for molecular calculations. Potentials for K to Au including the outermost core orbitals. *J. Chem. Phys.* **1985,** *82* (1), 299-310.

60. Wadt, W. R.; Hay, P. J., Ab initio effective core potentials for molecular calculations. Potentials for main group elements Na to Bi. *J. Chem. Phys.* **1985,** *82* (1), 284-298.

61. Cancès, E.; Mennucci, B.; Tomasi, J., A new integral equation formalism for the polarizable continuum model: Theoretical background and applications to isotropic and anisotropic dielectrics. *J. Chem. Phys.* **1997,** *107* (8), 3032-3041.

62. Mennucci, B.; Tomasi, J., Continuum solvation models: A new approach to the problem of solute's charge distribution and cavity boundaries. *J. Chem. Phys.* **1997,** *106* (12), 5151-5158.

63. Scalmani, G.; Frisch, M. J., Continuous surface charge polarizable continuum models of solvation. I. General formalism. *J. Chem. Phys.* **2010,** *132* (11), 114110.

64. Frisch, M.; Trucks, G.; Schlegel, H.; Scuseria, G.; Robb, M.; Cheeseman, J.; Scalmani, G.; Barone, V.; Mennucci, B.; Petersson, G., Gaussian 09 Revision D. 01, 2009, Gaussian Inc. *Wallingford CT* **2009,** *93*.

65. Gasparro, F. P.; Kolodny, N. H., NMR determination of the rotational barrier in N,N-dimethylacetamide. A physical chemistry experiment. *J. Chem. Educ.* **1977,** *54* (4), 258.

66. Gutz, I. G. R. CurTiPot – pH and Acid–Base Titration Curves: Analysis and Simulation freeware. http://www.iq.usp.br/gutz/Curtipot_.html.

67. Islamoglu, T.; Ortuño, M. A.; Proussaloglou, E.; Howarth, A. J.; Vermeulen, N. A.; Atilgan, A.; Asiri, A. M.; Cramer, C. J.; Farha, O. K., Presence versus Proximity: The Role of Pendant Amines in the Catalytic Hydrolysis of a Nerve Agent Simulant. *Angew. Chem. Int. Ed.* **2018,** *57* (7), 1949-1953.

68. Sullivan, K. P.; Neiwert, W. A.; Zeng, H.; Mehta, A. K.; Yin, Q.; Hillesheim, D. A.; Vivek, S.; Yin, P.; Collins-Wildman, D. L.; Weeks, E. R.; Liu, T.; Hill, C. L., Polyoxometalate-based gelating networks for entrapment and catalytic decontamination. *Chemical Communications* **2017,** *53* (83), 11480-11483.

Chapter 3: A Solvent-Free Solid Catalyst for the Selective and Color-Indicating Ambient-Air Removal of Sulfur Mustard

with contributions from

Kevin Sullivan, Victoria Snider, Yurii Geletii, Wesley Gordon, Alex Balboa, Yiyao Tian, Rachel Slaugenhaupt, Christopher Karwacki, Anatoly Frenkel, and Craig Hill

3.1 Introduction

The selective conversion of sulfides to sulfoxides without overoxidation to the sulfone is a key synthetic reaction for multiple applications.[1-6] One particularly pressing application is the decontamination of bis(2-chloroethyl) sulfide (sulfur mustard or HD), one of the highest-tonnage chemical warfare agents (CWA) and one that is highly persistent in the environment.[7-12] While HD can be removed, in principle, by either oxidation or hydrolysis, oxidation is generally targeted as the hydrolysis reaction with HD is quite slow.[13] Dioxygen represents an ideal oxidant as it is abundant, inexpensive, and atom economical.[14, 15] For oxidative decontamination, selective oxidation of HD to the sulfoxide (Equation 3.1), is crucial as the sulfoxide is substantially less toxic than the more oxidized sulfone.[9, 10, 13, 16-18] Materials capable of selective O_2-based sulfoxidation are therefore highly desirable.[1, 2, 19, 20] Specifically, there is a need to develop catalytic systems capable of rapid, selective, HD decontamination under ambient conditions.

$$(ClCH_2CH_2)_2S + \tfrac{1}{2}\, O_2 \rightarrow (ClCH_2CH_2)_2SO \qquad (3.1)$$

Given their selective sulfoxidation activity in solution, many studies have explored systems containing bromine (Br_y) and nitrogen oxide (NO_x) species.[21-24] More recently, this type of system was proven effective for sulfoxidation of the HD simulant, 2-chloroethyl ethyl sulfide (CEES), in acetonitrile.[25-27] However, despite promising results, (a) solid formulations of these oxidation catalysts to enable practical applications are unknown, (b) fundamental aspects of the complicated mechanism have eluded researchers, and (c) live agent (HD) studies are lacking. Understanding how this promising system behaves with live agent and in the absence of additional solvent, is crucial to the development of a truly effective material for catalytic aerobic HD removal.

Here, we report the development of such a material working as a solvent-free, solid formulation catalyst (henceforth "**SFC**") for selective air (O_2)-based sulfoxidation of both live agent HD and its simulant, CEES. **SFC,** comprises tetrabutylammonium tribromide ($TBABr_3$), tetrabutylammonium nitrate ($TBANO_3$), copper nitrate trihydrate (Cu(II)), and Nafion^{TM}. We were able to formulate this effective solid material for HD decontamination by first addressing key aspects of the complex proposed reaction mechanism outlined in Scheme 3.1. These insights included demonstration of an equilibrium associated with the formation of a key reactive intermediate and the effects of Cu(II) on the catalytic system. In addition, through the use of X-ray absorption spectroscopy we were able to follow the regeneration of the catalytic component, tribromide, during a solvent-free reaction with CEES.

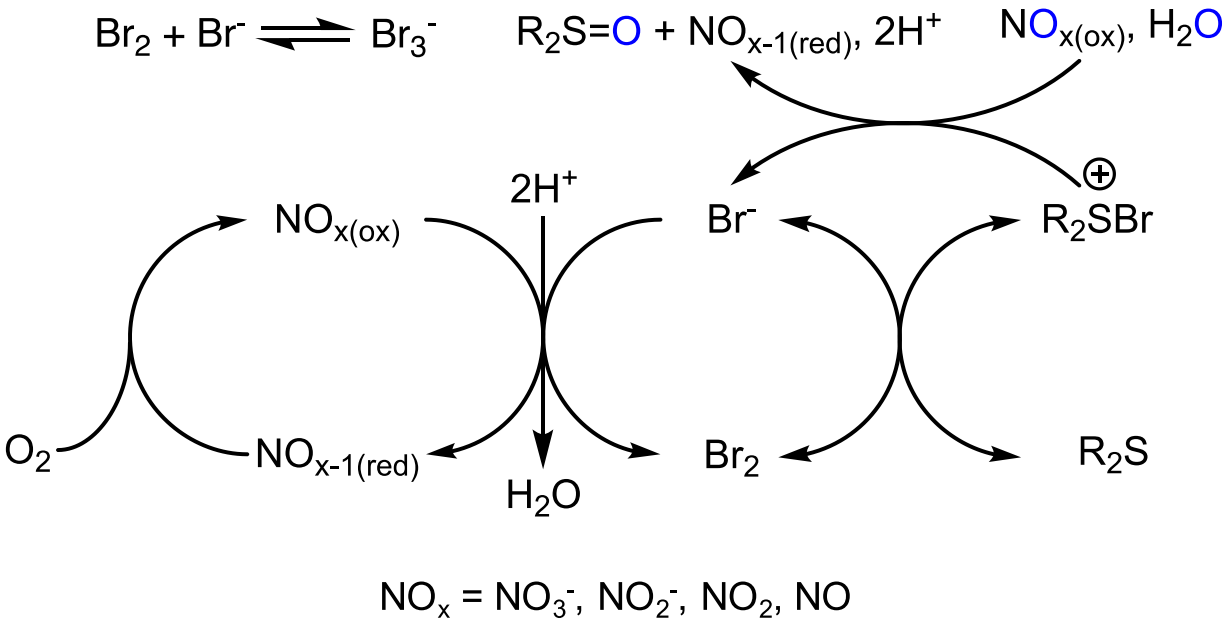

Scheme 3.1. Proposed general reaction scheme for oxygen-based catalytic and selective oxidation of sulfides (R_2S), such as HD, to sulfoxides using Br_3^- and NO_3^-/NO_2^- salts.

3.2 Experimental

3.2.1 Materials and General Methods

All chemicals were reagent grade or higher and were used as received unless otherwise specified. CEES, Nafion™, $TBABr_3$, and $TBANO_3$ were purchased from Sigma-Aldrich and $Cu(NO_3)_2 \cdot 3H_2O$ was purchased from Sargent-Welch VWR.

All measurements were conducted at ambient temperature (22±1 °C).

3.2.2 Synthesis of 2-chloroethyl ethyl sulfoxide (CEESO) standard

The following synthesis is a modification of previous literature reports.[25, 28] CEES (2 mL) was added dropwise to concentrated nitric acid (10 mL) in a 25 mL round bottom flask with stirring. A reflux condenser was used to minimize the loss of gases from the system, and the round bottom flask was placed in a water bath to maintain a constant temperature as the CEES was added. The solution was stirred for 1 hour and then poured over a mixture of ice and water (~50 mL). Once the ice had melted, the product was extracted three times with dichloromethane. These dichloromethane layers were combined, and any remaining acid was neutralized twice with 1M aqueous sodium bicarbonate by shaking the two layers together in a separatory funnel. The dichloromethane layer was then dried with anhydrous magnesium sulfate. The mixture was filtered, and the volume was reduced in a roto-evaporator until only an oil remained, which was the target product, CEESO.

3.2.3 Gas Chromatography Measurements

Gas chromatography (GC) data were collected on an Agilent Hewlett Packard (HP) 6890 GC system with an HP-5 5% phenyl methyl siloxane column and a flame ionization detector (FID).

3.2.4 Solution Oxidation Studies

Stock solutions with concentrations of 50 mM in acetonitrile (MeCN) were prepared for $TBABr_3$, $TBANO_3$, *p*-TsOH, and $Cu(NO_3)_2 \cdot 3H_2O$ (in some cases $Cu(ClO_4)_2 \cdot 6H_2O$). To prepare catalytic reactions, the necessary volumes of each of these stock solutions were added to a 20-mL glass vial fitted with a polytetrafluoroethylene (PTFE) septum followed by addition of H_2O (for experiments including H_2O) and the 1,3-dichlorobenzene (DCB) internal standard (70 mM). MeCN was added to make the total volume equal to 2 mL after addition of all components. Solutions were stirred with PTFE coated stir bars at a rate of 620 rpm. CEES (60 μL, 515 μmol, 103 mM) was added to initiate the reaction. The first time point was taken by GC immediately following the addition of CEES. To keep the partial pressure of O_2 in the headspace constant, the vials were sealed with PTFE septa after the initial time point and oxygen balloons were attached to the vials. As the reaction proceeds, O_2 is consumed lowering the pressure in each vial. The O_2 balloon replaces the lost oxygen thus maintaining constant pressure and composition of the headspace. For each time point, 0.4 μL of the reaction solution was injected on the GC column. Reaction conversion was followed through integration of the CEES peak area relative to that of the 1,3-DCB internal standard. Selectivity was confirmed by ^{13}C NMR.

3.2.5 Solution NMR experiments

Solution ^{13}C NMR spectroscopic measurements were made on a Bruker Ascend™ AVANCE III 600 MHz spectrometer with a broadband cryogenic cooler Prodigy CryoProbe™. Additional ^{13}C NMR measurements were conducted on a Varian INOVA 400 MHz spectrometer using a Varian DM40P5AP04 probe. All NMR tubes used have a 5 mm outer diameter (OD) and were spun at 20 Hz.

3.2.6 Stopped-Flow Studies

Stock solutions (50 mM) were made for all reagents used in the stopped-flow studies with the exception of CEES, and H_2O. The CEES and H_2O were added directly to reaction solutions by micropipette. For each experimental solution, reagents were mixed and diluted to the desired concentration in 20 mL scintillation vials capped with PTFE septa. Glass syringes were used to load sample solutions from vials into the instrument. Each sample was passed through the system 7 times to remove all traces of previous experiments. Kinetic curves were obtained using a HI-TECH Scientific KinetAsyst SF-61sX2 sample-handling unit with a diode array spectrophotometer.

3.2.7 UV-vis Studies

Stock solutions (50 mM) were made for all reagents used in the UV-vis studies with the exception of CEES, and H_2O. The CEES and H_2O were added directly to reaction solutions by micropipette. For each experimental solution, reagents were mixed and diluted to the desired concentration in 20 mL scintillation vials capped with PTFE septa. Aliquots of 15 µL from these solutions were diluted 200 times with MeCN creating a 3 mL total volume and transferred to an airtight 1 cm pathlength quartz cuvette. The dilution allowed accurate measurement of the Br_3^- absorption maximum at 270 nm using an Agilent 8453 UV-visible spectrophotometer. In cases with mixed acetonitrile-water solvent systems, the dilution was done with the same concentration of water to keep this variable constant. In the case where water was removed from the solution, 1.2 g of anhydrous $MgSO_4$ was added to the 5 mL solution of 5 mM $TBABr_3$, 50 mM CEES, and 2% H_2O following a measurement of the UV spectra. The mixture was vigorously swirled to ensure reaction between the solid $MgSO_4$ and H_2O in the solution. After 15 minutes of

equilibration time, the $MgSO_4$ particles were no longer suspended in solution and a 15 µL aliquot was taken and diluted 200 times as described above for the UV measurement.

3.2.8 Solid Formulation Catalyst (SFC) Preparation

Nafion™ (150 mg, 136 mmol equivalents of H^+), $TBABr_3$ (145 mg, 300 mmol), $TBANO_3$ (61 mg, 200 mmol), and $Cu(NO_3)_2 \cdot 3H_2O$ (24 mg, 100 mmol) were mechanically mixed with a mortar and pestle. The green solid was then transferred to an airtight container for storage.

3.2.9 Solid Formulation Catalyst (SFC) Studies

The solid formulation catalyst, **SFC**, (25.3 mg) was added to 5 mL test tubes. CEES (50 µL, 430 µmol) was added directly on top of the solid initiating the reaction. Rubber septa (size 14/20) were used to cap the test tube and O_2 filled balloons were used to maintain the oxygen concentration in the headspace. A stock solution of 215 mM 1,3-DCB (internal standard) in toluene was made for CEES extraction and quantification from the solid-formulation reactions. The CEES in the test tubes was extracted after a few seconds of shaking the test tube with 2 mL of the 1,3-DCB stock solution and then quantified by GC. CEES and the product CEESO are soluble in toluene while other components are not thus shutting down the catalytic cycle once the toluene is added. As a result, each time point required a separate experiment. Selectivity was confirmed by ^{13}C NMR. Coaxial inserts (2mm stem OD) with D_2O were used for the lock to avoid introducing additional carbon peaks or the excessive use of deuterated toluene.

3.2.10 CEES Oxidation with SFC Under Relevant Battlefield Conditions

Hydrocarbons: **SFC** (25 mg) was added to 5 mL test tubes. Octane (40 µL, 240 mmol) and CEES (50 µL, 430 µmol) were added directly on top of the solid catalyst. Rubber septa (size 14/20) were used to cap the test tube. Balloons filled with O_2 were used to maintain the oxygen

concentration in the headspace. A stock solution of 215 mM 1,3-DCB (internal standard) in toluene was made for CEES extraction and quantification.

Carbon dioxide: **SFC** (25 mg) was added to 5 mL test tubes. CEES (50 µL, 430 µmol) was added directly on top of the solid catalyst. Rubber septa (size 14/20) were used to cap the test tube. CO_2 (150 µL, 6 µmol) was injected through the septa into the test tube using a gastight syringe. CO_2 was added in a 1:1 molar ratio with $Cu(NO_3)_2 \cdot 3H_2O$. Balloons filled with O_2 were used to maintain the oxygen concentration in the headspace. A stock solution of 215 mM 1,3-DCB (internal standard) in toluene was made for CEES extraction and quantification.

3.2.11 Live Agent Studies

Liquid HD reaction – The solid formulation catalyst, **SFC** (5 mg), was placed in a sealed vial with a 20 mL syringe filled with O_2 as the gas headspace. HD (5 µL) was applied to the surface of the **SFC**. Exposures were run for 1, 2, 4, 8, 24 and 96 hours. Exposed powder was placed into a 20 mL scintillation vial and 1.5 mL (reagent grade or better) chloroform was added. The slurry was vortexed for ~60 secs and drawn into a 2 mL Luer-slip plastic syringe (National S7510-3) and subsequently filtered through a (0.45 µm x 13 mm diameter) nylon membrane syringe filter into a clear silanized screw-top 2 mL vial (Agilent Technologies Part# 5183-2070). This was then placed in the autosampler of an Agilent 6890N Network GC System with a 5973 Network Mass Selective Detector.

Vapor HD reaction – The catalyst, **SFC**, was placed in the DRIFTS cup and equilibrated under a stream of 2% RH / Zero Air. After equilibration, background spectra were collected with 1024 scans per spectra. Data was collected in the following manner: 1024 scans were collected with a collection length of 726.96 sec. The resolution was kept at 2.000 cm^{-1} with levels of zero filling kept at zero. Each scan consisted of 33056 total points with 32768 fast fourier transform (FFT)

points. The laser frequency utilized was 15798.25 cm^{-1}, and the interferogram peak position was 16384. The apodization was Happ-Genzel and the phase correction was Mertz. The data represents 3735 points between 599.7627 to 4200.2676 with a spacing of 0.964249. The spectrometer is a Nicolet 6700 (Thermo Fisher Scientific Nicolet, Waltham MA), with an IR source, MCT/A detector and a KBr beam splitter. The optical velocity is 3.7974 with an aperture of 65.00 and a sample gain of 2.0. The high pass filter wavenumber is 200.0000 cm^{-1} and the low pass filter wavenumber is 50000.0000 cm^{-1}. After the background spectrum was collected, HD was introduced into the humid Zero Air Stream, and then difference spectra were collected for four hours.

3.2.12 X-ray Absorption Fine Structure (XAFS) experiments

XAFS experiments were performed at National Synchrotron Light Source (NSLS) II, Beamline 7-BM quick X-ray absorption and scattering (QAS). For the solid-liquid CEES exposure (Figure 3.20), 30 mg of **SFC** was exposed to 50 µL of liquid CEES under ambient air in a closed glass vial for 0, 3, and 76 hours. Aliquots of the slurry mixture were loaded in Kapton capillaries for XAFS measurements. For the in situ solid-gaseous CEES exposure (Figure 3.24), 4 mg of **SFC** was loaded in a Kapton capillary with both ends open and the capillary was fixed inside a Nashner-Adler cell, a sealed jar customized for XAFS measurements. Liquid CEES (2 mL) was soaked in the cotton wool placed in a beaker with the volume of 3 mL at the bottom of the cell and produced CEES vapors. The cell was sealed under ambient air. Br K-edge (~13478 eV) XAFS data, collected in transmission mode with 45 seconds per spectrum, were simultaneously measured with Au foil with the L_2-edge at 13734 eV for energy alignment and calibration purposes. Cu K-edge (~8979 eV) XAFS data, collected in fluorescence mode with 45 seconds per spectrum, were simultaneously measured with Cu foil for energy alignment and calibration

purposes. XAFS data were processed and analyzed using Athena and Artemis[29] programs of the IFEFFIT package[30]. Quantitative analysis of Br K-edge EXAFS was performed by fitting theoretical EXAFS spectra to the experimental data in r-space. The fitting model was constructed by adopting a structure of Br_2 and the scattering contribution from a Br-Br bond of 2.301 Å was included. The amplitude factor was fixed to be 0.8. Quantitative analysis of Cu K-edge EXAFS was performed by fitting theoretical EXAFS spectra to the experimental data in r-space. The fitting model for Cu K-edge EXAFS of **SFC** before CEES exposure was constructed by adopting a structure of $Cu(NO_3)_2$ and the scattering contribution from a Cu-O bond of 1.959 Å was included. The fitting model for Cu K-edge EXAFS of **SFC** after CEES exposure for 3 hours was constructed by adopting a structure of $CuBr_2$ and CuS, and the scattering contribution from a Cu-Br bond of 2.420 Å and a Cu-S bond of 2.353 Å were included. The amplitude factor was fixed to be 0.85.

3.3 Results and Discussion

3.3.1 Mechanistic Studies in Acetonitrile.

The combination of tribromide and nitrate effectively catalyzes sulfoxidation reactions including that of the mustard simulant CEES.[25, 27] Studies have shown that transition metals can have significant effects in catalyzing the oxidation of sulfides.[31-35] We demonstrate here a significant acceleration in the rate of sulfoxidation in the presence of Cu(II). The addition of 1 mM Cu(II) to the reaction solution of 5 mM Br_3^- and 10 mM NO_3^- results in an initial rate for aerobic sulfoxidation roughly 4 times faster than without copper (Figure 3.1). This corresponds to the decontamination of 10 equivalents of simulant in under 7 minutes, which represents, to our knowledge, the fastest catalytic system for selective aerobic sulfoxidation. Importantly, the

reaction remains selective in the presence of Cu(II) and quantitatively produces the desired sulfoxide product as confirmed by ^{13}C NMR (Figure 3.2).

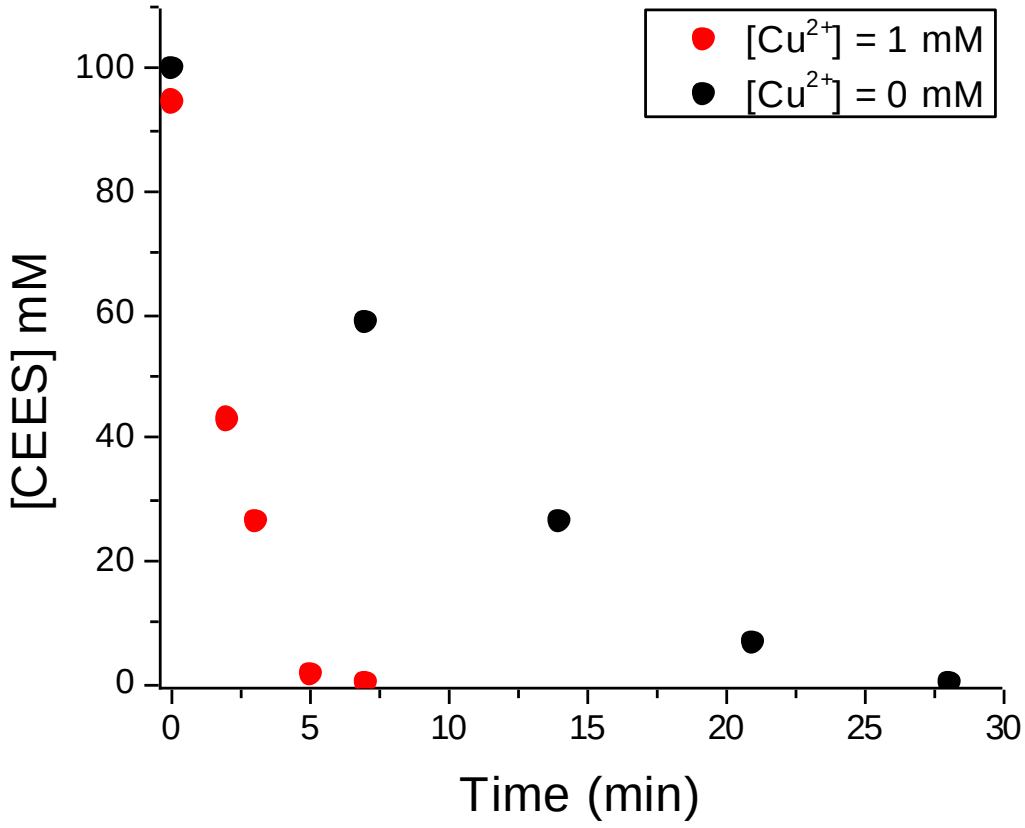

Figure 3.1. Kinetics of CEES oxidation by O_2 catalyzed by Br_3^-/NO_x with and without Cu(II). Conditions: 5 mM $TBABr_3$, 10 mM *p*-TsOH, 10 mM $TBANO_3$, 103 mM CEES, 70 mM 1,3-dichlorobenzene (1,3-DCB) internal standard, in MeCN, 1 atm air, ambient temperature (~22 ^oC). Red curve = 1 mM $Cu(ClO_4)_2 \cdot 6H_2O$, black curve = 0 mM $Cu(ClO_4)_2 \cdot 6H_2O$. These curves represent 10 turnovers based on NO_3^-.

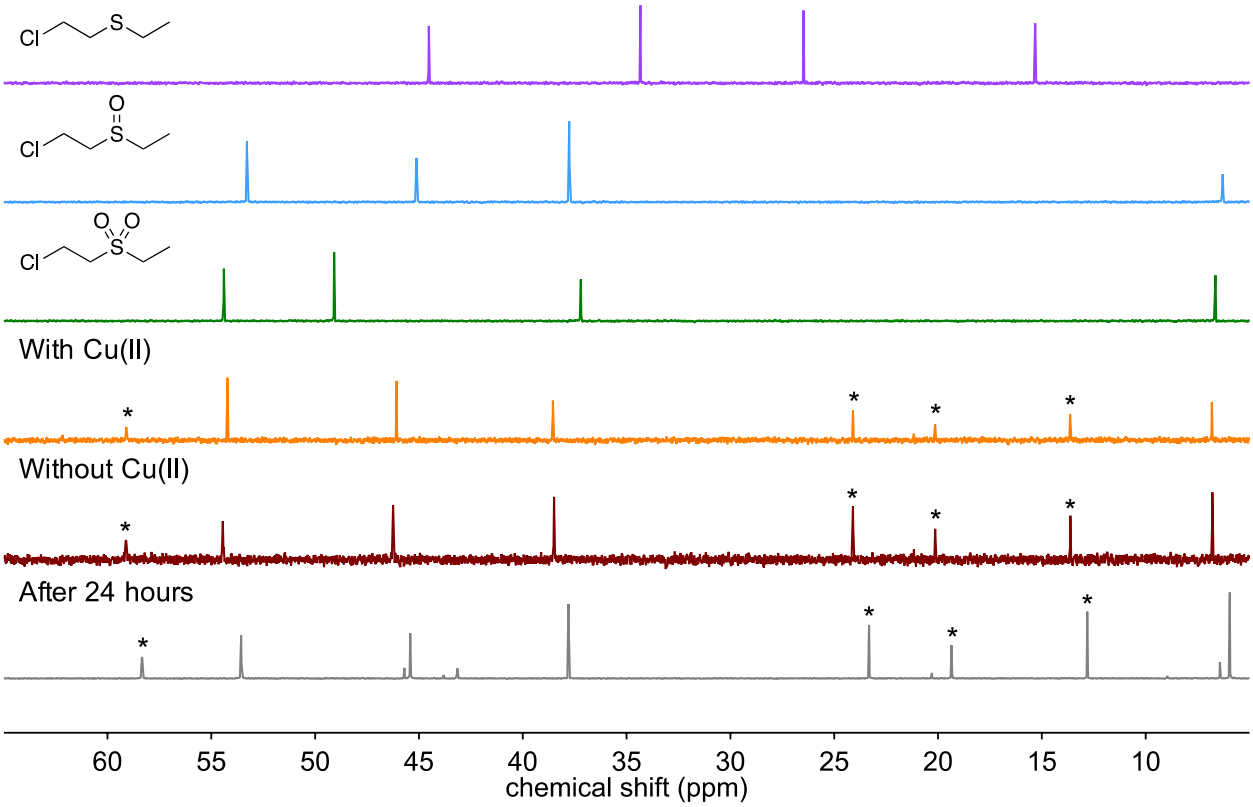

Figure 3.2. ^{13}C NMR of CEES reaction products. Conditions for catalytic trials prior to NMR analysis: 100 mM CEES, 5.0 mM $TBANO_3$, 5.0 mM $TBABr_3$, 10 mM *p*-TsOH, 2% H_2O and 10% CD_3CN (v/v) in MeCN at ambient temperature (22±1 ^oC) under 1 atm of air. Reaction run with copper: $[Cu(ClO_4)_2•6H_2O]$ = 1.5 mM. (*) = TBA counter cations. $CEESO_2$, CEESO and CEES standards were dissolved in CD_3CN (small differences between standard and reaction solution compositions result in slightly different chemical shifts). For the grey curve, the spectrum was taken 24 hours after reaction completion indicating complete oxidative selectivity for the sulfoxide.

To elucidate the role of copper in enhancing the rate of sulfide oxidation, we must first examine certain aspects of the complex proposed catalytic cycle outlined in Scheme 3.1. The

first step involves the reaction between the sulfide, CEES, and bromine to form a bromosulfonium complex that is likely a reaction intermediate (Equation 3.2).[6, 26, 36, 37]

$$R_2S + Br_2 \rightleftharpoons R_2S^+Br + Br^- \quad (3.2)$$

Due to the equilibrium shown in Equation 3.3, tribromide solutions will contain both Br_3^- and some Br_2 and Br^- with reported equilibrium constants of K =17 and 9 x 10^6 M^{-1} in water and in acetonitrile, respectively.[38-40] Solutions of Br_3^- and Br_2 both react with sulfides to form the bromosulfonium intermediate (Figure 3.3). In the case of tribromide it is generally predicted that the Br_3^- ion acts as a reservoir for Br_2 (via the equilibrium in Equation 3.3), which is ultimately the reactive species toward to the sulfide.[25-27]

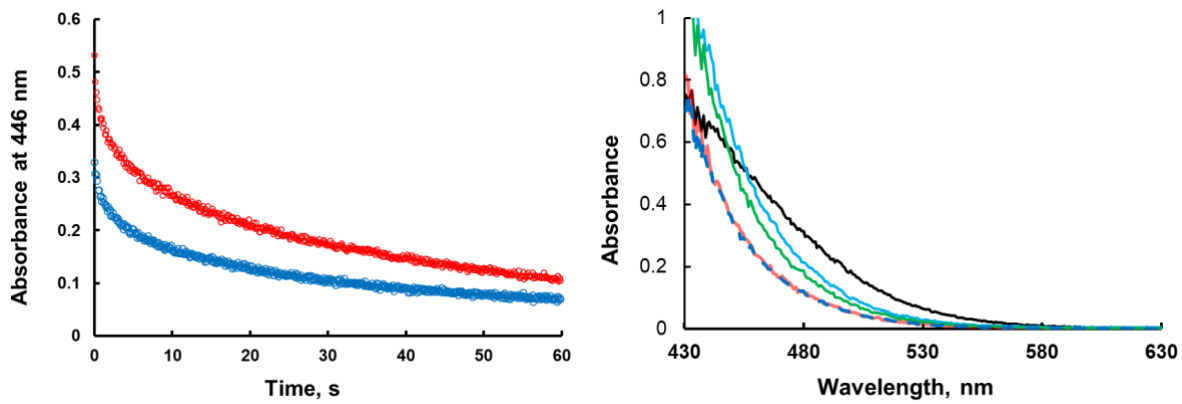

Figure 3.3. Left: Stopped-flow kinetics of 5 mM Br_2 (blue) or 5.0 mM $TMABr_3^-$ (red) consumption in the reaction with 50 mM CEES measured by the decrease of absorbance at 446 nm. Conditions: 2.0 % H_2O (v/v), 17 mM $HClO_4$, T = 22±1 ºC. Right: The spectra of 5 mM Br_2 (black), 5 mM Br_2 + 50 mM CEES (red), 5 mM $TMABr_3$ (blue), 5 mM $TMABr_3$ + 50 mM CEES (green) taken at 5 ms. Dashed blue line is the spectrum of 5 mM $TMABr_3$ (blue) multiplied by a factor 0.65.

$$Br^- + Br_2 \rightleftharpoons Br_3^- \quad (3.3)$$

The bromosulfonium intermediate (Equation 3.2) is proposed to form the sulfoxide via oxidation by NO_3^-.[25, 27] Therefore, shifts in the equilibrium associated with the formation of this bromosulfonium complex will have a significant impact on the overall reaction rate if the bromosulfonium species is prior to or in the rate limiting step. Stopped flow UV-vis measurements at 446 nm (the isosbestic point for Br_2/Br_3^-),[41] allow quantification of the total Br_2/Br_3^- over time. For a solution of 5 mM tribromide and 50 mM CEES, this equilibrium is shifted in favor of the reactants (Br_3^- and sulfide), however, the addition of 1-4% H_2O (v/v) shifts the equilibrium in favor of the bromosulfonium complex (Figure 3.4). After the loss of Br_2/Br_3^- upon reaction with CEES in the presence of H_2O, the desiccant $MgSO_4$ can be added to remove the water in the system. As the water is absorbed by $MgSO_4$, Br_2/Br_3^- are gradually regenerated demonstrating the truly reversible nature of Equation 3.2 (Figure 3.5). Water is likely shifting this equilibrium by slowing the reverse reaction between the bromosulfonium cation and bromide. This leads to higher concentrations of products in the presence of water compared with higher concentrations of reactants in the absence of water.

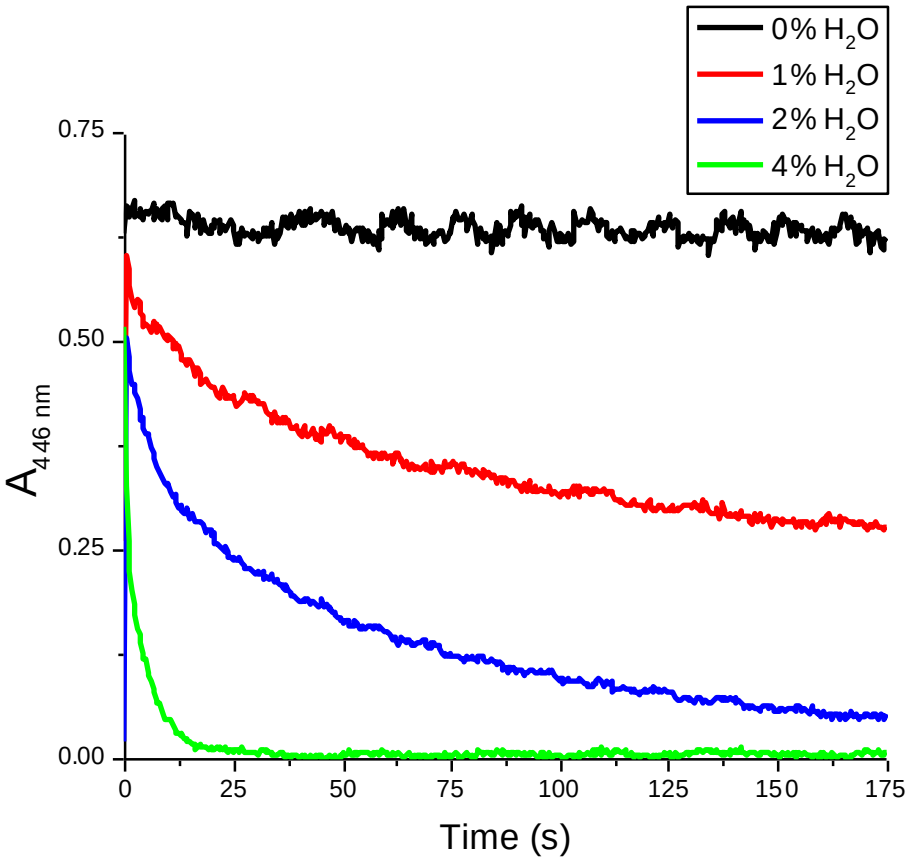

Figure 3.4. Stopped-flow kinetics of CEES reactivity with Br_2/Br_3^- as a function of water content. The reaction is followed by the decrease of the Br_2/Br_3^- isosbestic absorption at 446 nm. Conditions: 5 mM $TBABr_3$, 17 mM $HClO_4$, 50 mM CEES, in MeCN, ambient temperature (~22 ^oC). Varied water percentage (v/v): 0% (black), 1% (red), 2% (blue), 4% (green).

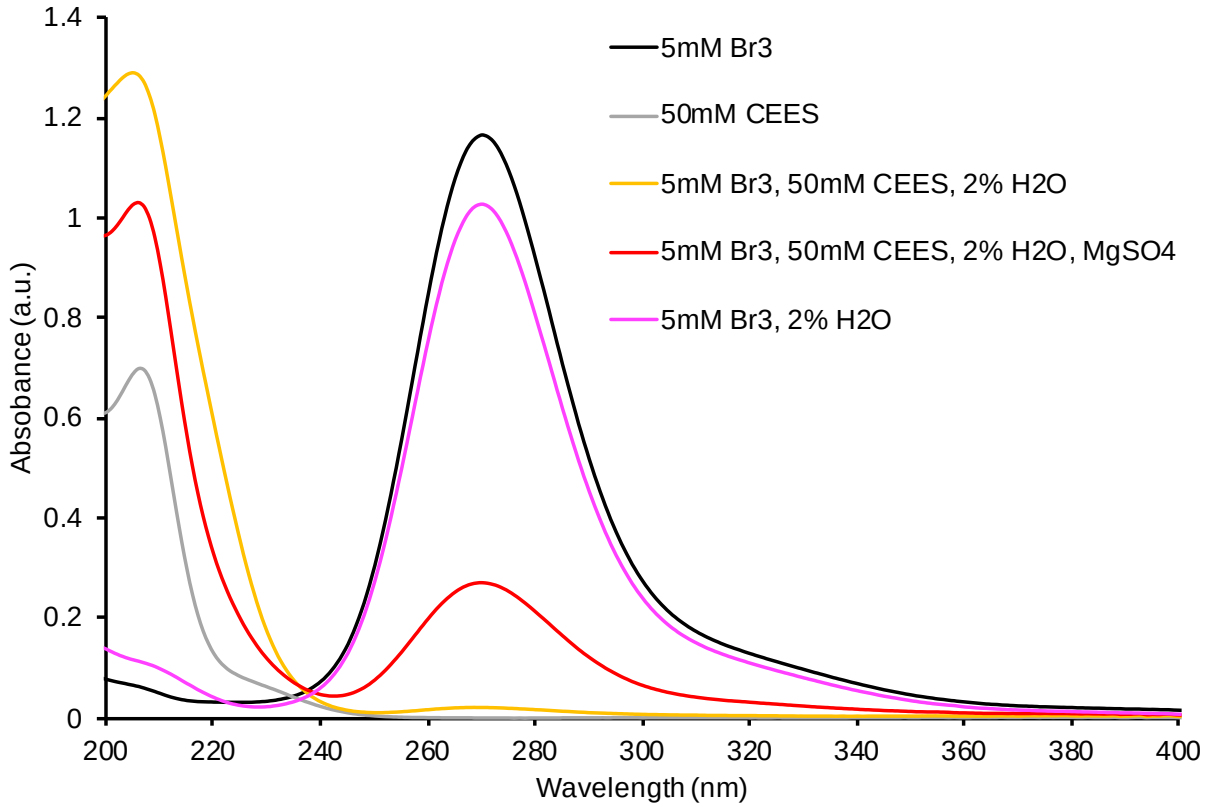

Figure 3.5. UV spectra of Br_3^- absorption (lambda max = 270 nm) with varied water and CEES concentrations. Samples were prepared at stated concentrations in MeCN (5 mL total volume) and then diluted 200x to measure the UV spectra. Black curve = 5 mM $TBABr_3$; grey curve = 50 mM CEES; yellow curve = 5 mM $TBABr_3$, 50 mM CEES, 2% H_2O; red curve = 5 mM $TBABr_3$, 50 mM CEES, 2% H_2O, 1.2 g $MgSO_4$; purple curve = 5 mM $TBABr_3$, 2% H_2O. For the sample with both CEES and Br_3^-, the solution was allowed to equilibrate for 15 minutes before measurement and another 15 minutes after the addition of $MgSO_4$.

Similar to water, addition of $Cu(ClO_4)_2 \cdot 6H_2O$ causes an equilibrium shift in favor of the bromosulfonium complex (Figure 3.6). In this case the reaction is followed by the growth of $CuBr_3^-$, which has a ligand-to-metal charge transfer (LMCT) band at 635 nm.[42, 43] This can be used as an indirect means to monitor the concentration of Br_2/Br_3^- as the Br^- liberated upon the

forward reaction between the sulfide and Br_2/Br_3^- in Equation 3.2 quickly forms complexes with Cu (Equation 3.4).

$$Cu^{2+} + xBr^- \rightleftharpoons (CuBr_x)^{(2-x)} \quad (3.4)$$

Given the lack of absorption at 635 nm in the absence of sulfide (Figure 3.6), the rapid formation of $CuBr_3^-$ directly correlates with the formation of the bromosulfonium intermediate. For copper, the equilibrium in Equation 3.2 again shifts in favor of the bromosulfonium intermediate as the reverse reaction with Br^- is inhibited by the complexation of free Br^- ions by copper. As shown in Figure 3.1 the presence of Cu(II) clearly enhances the overall rate, which is consistent with an increase in concentration of the reactive bromosulfonium intermediate.

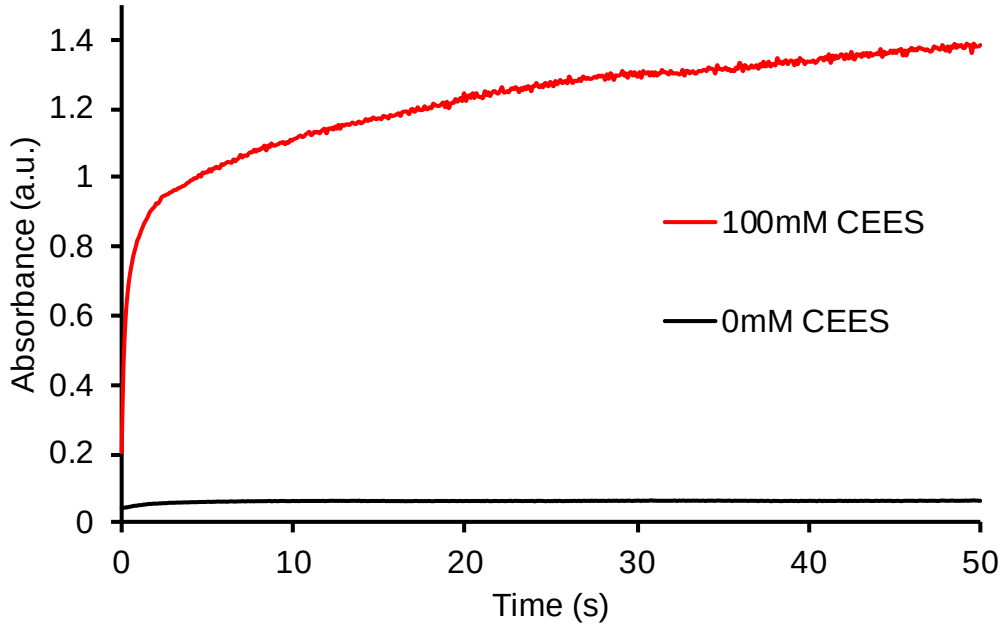

Figure 3.6. Stopped-flow kinetics of $CuBr_3^-$ formation in the presence and absence of CEES. The reaction is followed by the growth of $CuBr_3^-$ absorption at 635 nm. Conditions: 5 mM $TBABr_3$, 1 mM $Cu(ClO_4)_2 \cdot 6H_2O$, in MeCN, ambient temperature (~22 °C). Red curve = 103 mM CEES, black curve = 0 mM CEES.

Given the strong effect of copper, we also examined the effect of Zn(II) ions to see if a similar equilibrium shift would occur. As with copper, zinc readily forms complexes with Br- ions (Equation 3.5).[44]

$$Zn^{2+} + xBr^- \rightleftharpoons (ZnBr_x)^{(2-x)} \quad (3.5)$$

In this case, however, the complexes are colorless allowing the reaction to be followed by the loss of Br_2/Br_3^- at 446 nm. In the presence of 5 mM of $Zn(BF_4)_2$, the majority of the Br_2/Br_3^- is consumed in under 10 seconds indicating a rapid equilibrium shift of Equation 3.2 in favor of the products (Figure 3.7). As with copper this is likely caused by decreasing the rate of the reverse reaction due to the lower concentration of free Br^-. To confirm this, we added 10 mM Br^- to the initial Zn solution mixed with CEES and observed that these additional Br- ions did in fact lessen the effect of Zn (Figure 3.8).

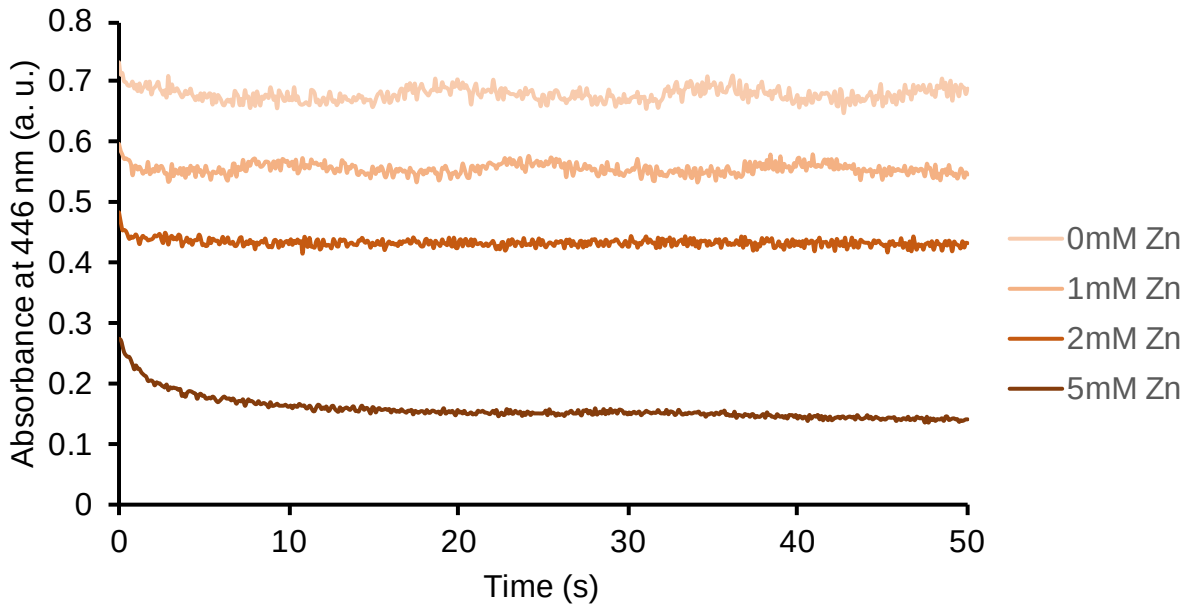

Figure 3.7. Stopped-flow kinetics of CEES reactivity with Br_2/Br_3^- as a function of $[Zn(BF_4)_2]$. The reaction is followed by the decrease of the Br_2/Br_3^- isosbestic absorption at 446 nm. Conditions: 5 mM $TBABr_3$, 103 mM CEES, in MeCN, ambient temperature (~22 ^oC). Varied zinc concentration: 0 mM to 5 mM $Zn(BF_4)_2$ (light to dark maroon respectively).

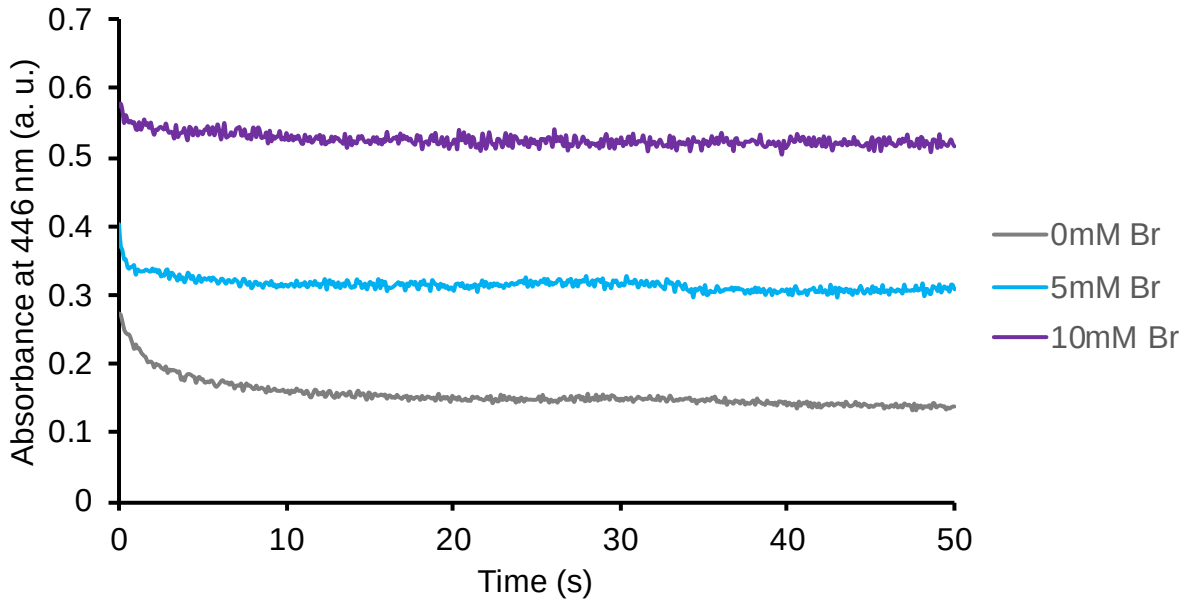

Figure 3.8. Stopped-flow kinetics of CEES reactivity with Br_2/Br_3^-. The reaction is followed by the decrease of the Br_2/Br_3^- isosbestic absorption at 446 nm. Conditions: 5 mM $TBABr_3$, 103 mM CEES, 10 mM $Zn(BF_4)_2$, in MeCN, ambient temperature (~22 ºC), varied concentrations of TBABr: 0 mM (grey), 5 mM (blue), 10 mM (purple).

Interestingly, while Cu(II), Zn(II), and H_2O all shift the initial reaction between Br_2 and sulfide in favor of the bromosulfonium intermediate, only Cu shows an enhancement in the overall rate of catalysis. For reactions containing 1 M water, the overall sulfoxidation is similar to the rate in the absence of water. For reactions containing both copper and water, the presence of 1 M water slows down the reaction (Figure 3.9). In the presence of 5 mM $Zn(BF_4)_2$ the reaction is also slowed. This likely occurs as the presence of water and zinc slow the oxidation of Br^- ions back to Br_2 which completes the catalytic cycle for Br-containing species. One of the anticipated reduced NO_x species formed during the catalytic cycle (Scheme 3.1) is nitrous acid which is known to oxidize Br^- to Br_2 via the following equilibria (Equations 3.6 and 3.7).[45, 46]

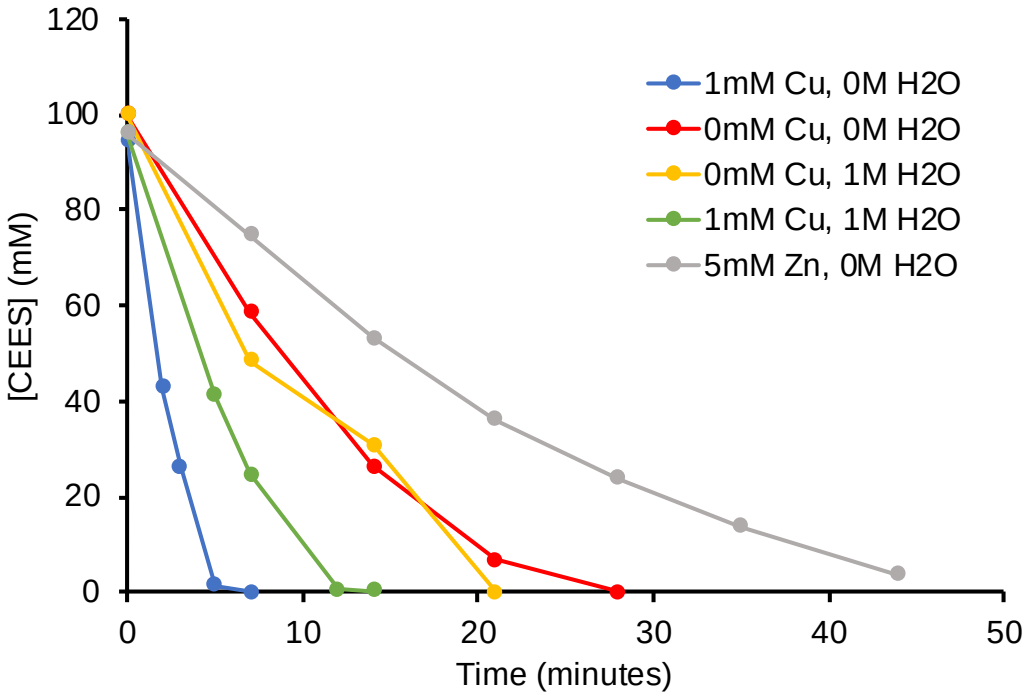

Figure 3.9. Kinetics of CEES oxidation under full catalytic conditions with and without Cu(II), H_2O. Conditions: 5 mM $TBABr_3$, 10 mM *p*-TsOH, 10 mM $TBANO_3$, 103 mM CEES, 70 mM 1,3-dichlorobenzene (1,3-DCB) internal standard, in MeCN, 1 atm air, ambient temperature (~22 ^oC). Blue curve = 1 mM $Cu(ClO_4)_2$, 0 M H_2O; red curve = 0 mM $Cu(ClO_4)_2$, 0 M H_2O; orange curve = 0 mM $Cu(ClO_4)_2$, 1 M H_2O; green curve = 1 mM $Cu(ClO_4)_2$, 1 M H_2O; grey curve = 5 mM $Zn(BF_4)_2$, 0 M H_2O. These curves represent 10 turnovers based on NO_3^-.

$$HNO_2 + Br^- + H^+ \rightleftharpoons NOBr + H_2O \quad (3.6)$$

$$2NOBr \rightleftharpoons 2NO + Br_2 \quad (3.7)$$

Stopped-flow UV-vis measurements show that increasing concentrations of water or zinc greatly inhibit the oxidation of Br^- by nitrous acid (Figures 3.10 and 3.11). In contrast, the oxidation of Br^- to Br_2 proceeds similarly in the presence of Cu(II) ions compared to the control (Figure 3.12). This suggests that copper, unlike water or zinc, is able to shift the equilibrium of

the initial reaction between the sulfide and Br_2/Br_3^- without disrupting other components of the catalytic system thereby affording a net increase in the overall rate.

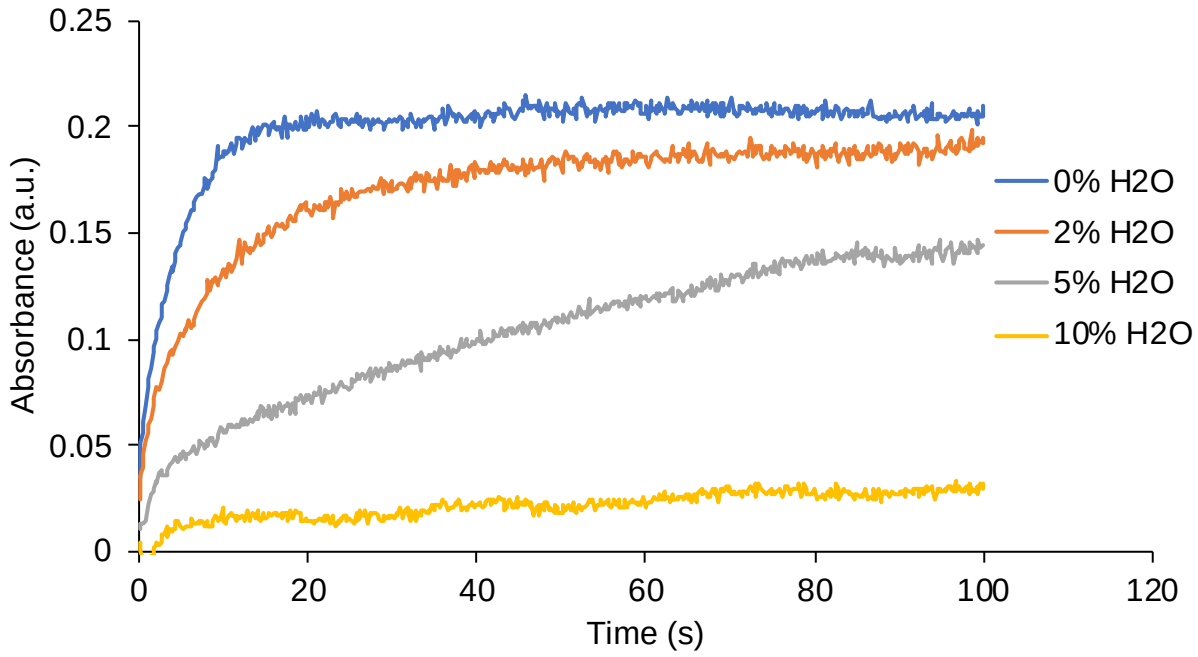

Figure 3.10. Stopped-flow kinetics of Br^- oxidation to form Br_2/Br_3^-. The reaction is followed by the increase of the Br_2/Br_3^- isosbestic absorption at 446 nm. Conditions: 15 mM TBABr, 5 mM $TBANO_2$, 5 mM *p*-TsOH, in MeCN at ambient temperature (~22 ^oC). Varied water percentage v/v: 0% (blue), 2% (orange), 5% (grey), 10% (yellow).

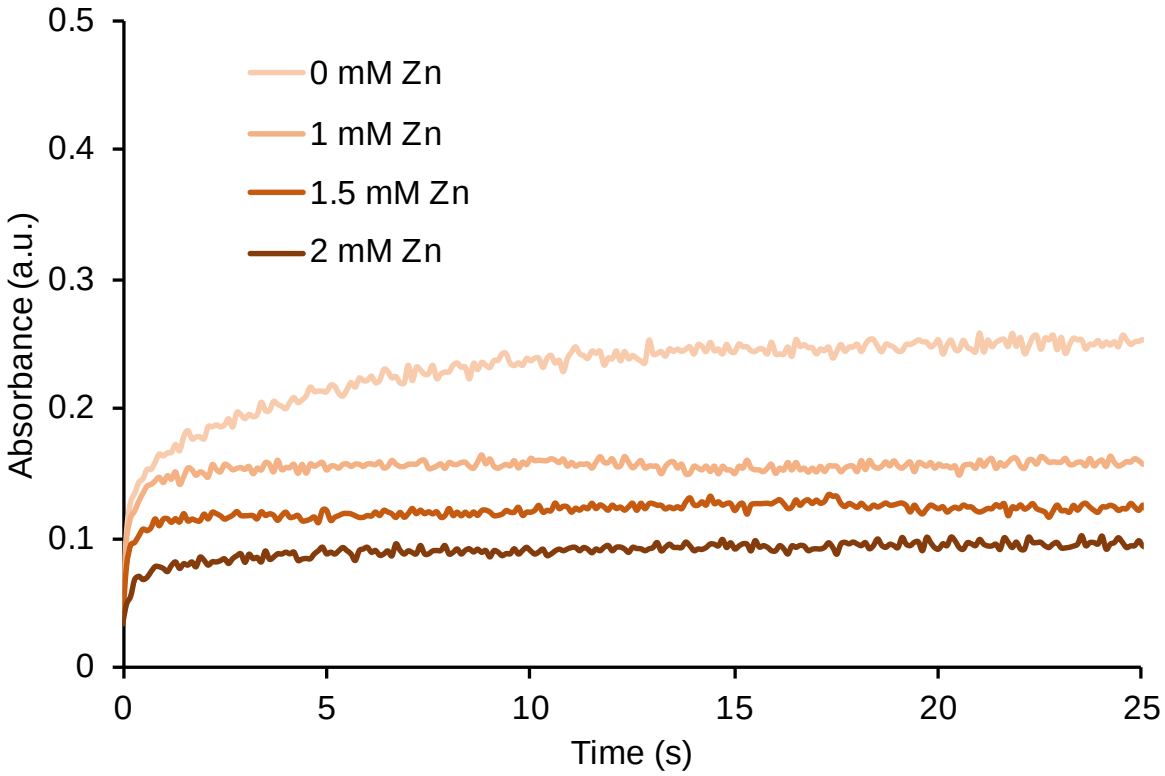

Figure 3.11. Stopped-flow UV-vis of Br^- oxidation to form Br_2/Br_3^-. Syringe 1: 20 mM *p*-TsOH, 10 mM TBA-NO_2 in acetonitrile (MeCN). Syringe 2: 10 mM TBA-Br, varied concentrations of $Zn(BF_4)_2$. Absorbance measurements taken at 446 nm.

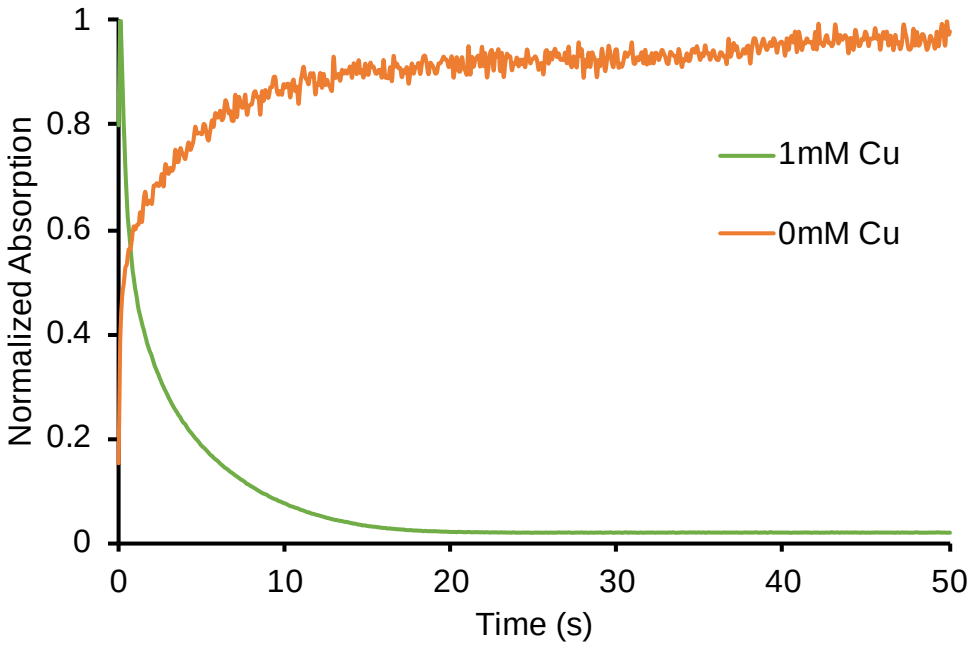

Figure 3.12. Stopped-flow kinetics of Br^- oxidation to form Br_2/Br_3^-. The reaction is followed by the increase of the Br_2/Br_3^- isosbestic absorption at 446 nm (orange) and the decrease of $CuBr_3^-$ absorption at 635 nm (green). Conditions: 5 mM TBABr, 5 mM $TBANO_2$, 10 mM *p*-TsOH, in MeCN at ambient temperature (~22 ^oC). Green curve = 1 mM $Cu(ClO_4)_2•6H_2O$; orange curve = 0 mM $Cu(ClO_4)_2•6H_2O$. Absorptions were normalized for ease of comparison.

In addition to markedly improving the rate of catalysis, the use of Cu(II) also enables the colorimetric detection of sulfides in the system. Immediately upon exposure to CEES, the catalytic solution undergoes a dramatic color change from pale yellow to dark green, attributable to the formation of $CuBr_3$ (Figure 3.13).[42, 43] Upon reaction completion, Br^- ions are no longer produced from the reaction between Br_2 and CEES allowing all of the Br^- ions to be oxidized re-establishing the original Br_3^- concentration (via Equations 3.6, 3.7 and 3.2). This returns the solution to its original yellow color and thereby indicates when the sulfide (HD or simulant CEES) has been fully decontaminated.

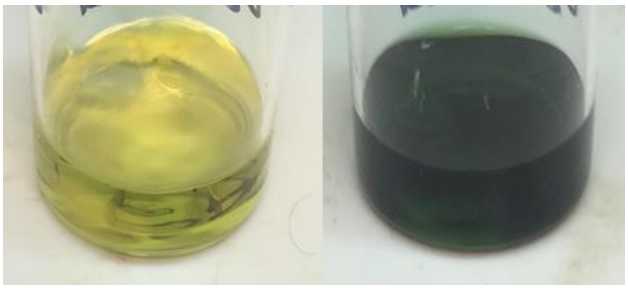

Figure 3.13. Responsive color change behavior in the homogeneous Br_x/NO_x/Cu(II) system. Left: solution containing 5.0 mM $TBABr_3$, 5.0 mM $TBANO_3$, 1.7 mM $Cu(ClO_4)_2 \cdot 6H_2O$, 10 mM *p*-TsOH, and 2% H_2O (v/v) in MeCN. Right: the same system immediately after addition of 100 mM CEES. Solutions were at ambient temperature (22±1 ºC) under 1 atm of air.

3.3.2 The solid, color-indicating, aerobic mustard (HD) oxidation catalyst

With the above solution catalytic studies in hand, we turned to formulating a solid version of this catalyst to enable the development of protective materials (garments, masks, coatings, etc.) for removal/colorimetric detection of HD. Informed by previous studies,[26, 27] and our own work with solution-phase reactions, we incorporated sources of acid and copper along with tribromide and nitrate. Nafion™ was chosen for the acid as it is a chemically robust perfluorinated polymer, and it is well tolerated by human skin. By utilizing $Cu(NO_3)_2 \cdot 3H_2O$, we were able to incorporate both a source of copper and nitrate. Through the use of quaternary ammonium salts of nitrate and tribromide, the active catalytic components are stable under ambient conditions and readily dissolve in the sulfide, providing a solid formulation that reacts directly with live agent in the absence of solvent. The end result is a fully selective, color-indicating solvent-free, solid catalyst (**SFC**) comprising a 5.0:3.3:1.7:2.3 mole ratio of $TBABr_3$, $TBANO_3$, $Cu(NO_3)_2 \cdot 3H_2O$ and Nafion™ polymer, respectively (moles of Nafion™ reported as equivalents of H^+).

To assess the effectiveness of **SFC** in the absence of additional solvent, liquid aliquots of sulfide were placed directly on this solid catalyst. Upon exposure to 22 equivalents of neat CEES (relative to the Br_3^- in **SFC**), **SFC** completely and selectively catalyzes production of the sulfoxide using only oxygen in ambient air as the terminal oxidant at ambient temperature (Figures 3.14 and 3.15). Exposure of **SFC** to two common battlefield contaminants, octane (as a surrogate for gasoline) and CO_2, did not show any measurable inhibition of the reaction rate (Figure 3.16). Significantly, selective aerobic sulfoxidation was also observed with 10 equivalents of live agent HD (Figures 3.17 and 3.18). This catalytic system thus represents a significant advance in the development of protective materials against HD, as it is capable of decontaminating HD selectively and catalytically upon contact. Finally, this system is also colorimetric, immediately revealing distinct color changes from light green to dark brown in the presence of the harmful agent/simulant (Figure 3.19).

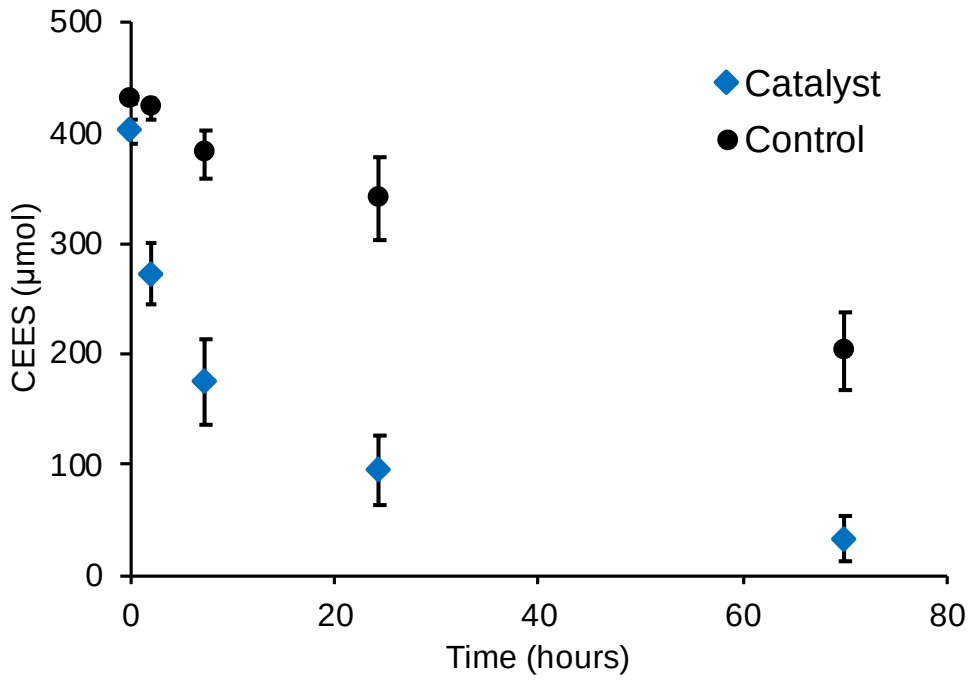

Figure 3.14. Kinetics of CEES oxidation catalyzed by **SFC**. Conditions: 50 µL (430 µmol) of neat CEES added directly to 25.3 mg of the **SFC** (9.6 mg $TBABr_3$, 4.1 mg $TBANO_3$, 1.6 mg $Cu(NO_3)_2 \cdot 3H_2O$, 10 mg Nafion^{TM}), under 1 atm of air at ambient temperature (22±1 ^oC). The control was done in the absence of **SFC**. For the control, CEES concentration falls as a result of evaporation, not oxidation. Measurements taken by GC in triplicate with standard deviation error shown.

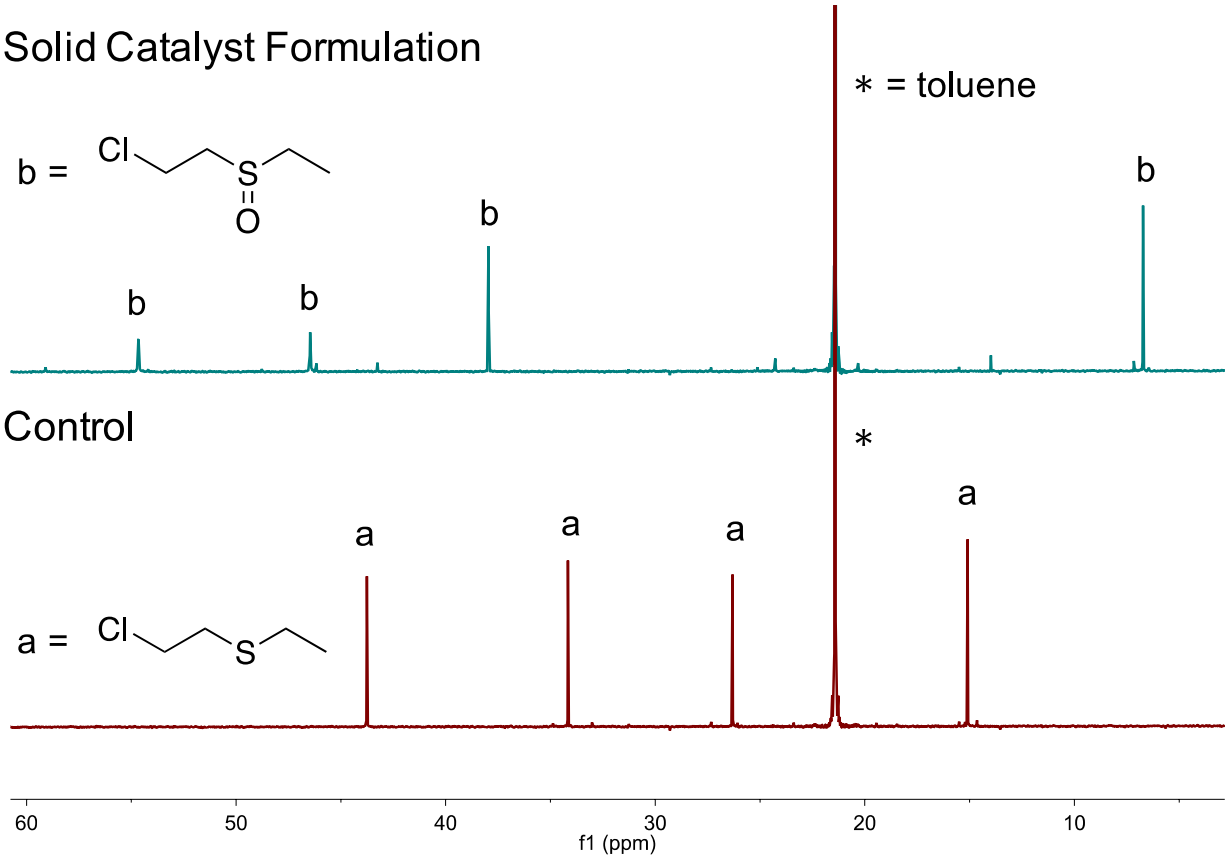

Figure 3.15. ^{13}C NMR of products of neat CEES reactions extracted into toluene (see above materials and methods). Conditions for catalytic trials prior to NMR analysis: 50 μL (430 μmol) of neat CEES, 25.3 mg of **SFC** = 9.6 mg $TBABr_3$, 4.1 mg $TBANO_3$, 1.6 mg $Cu(NO_3)_2 \cdot 3H_2O$, 10 mg Nafion^{TM}, under 1 atm of air. Coaxial inserts filled with D_2O were used to generate the lock signal.

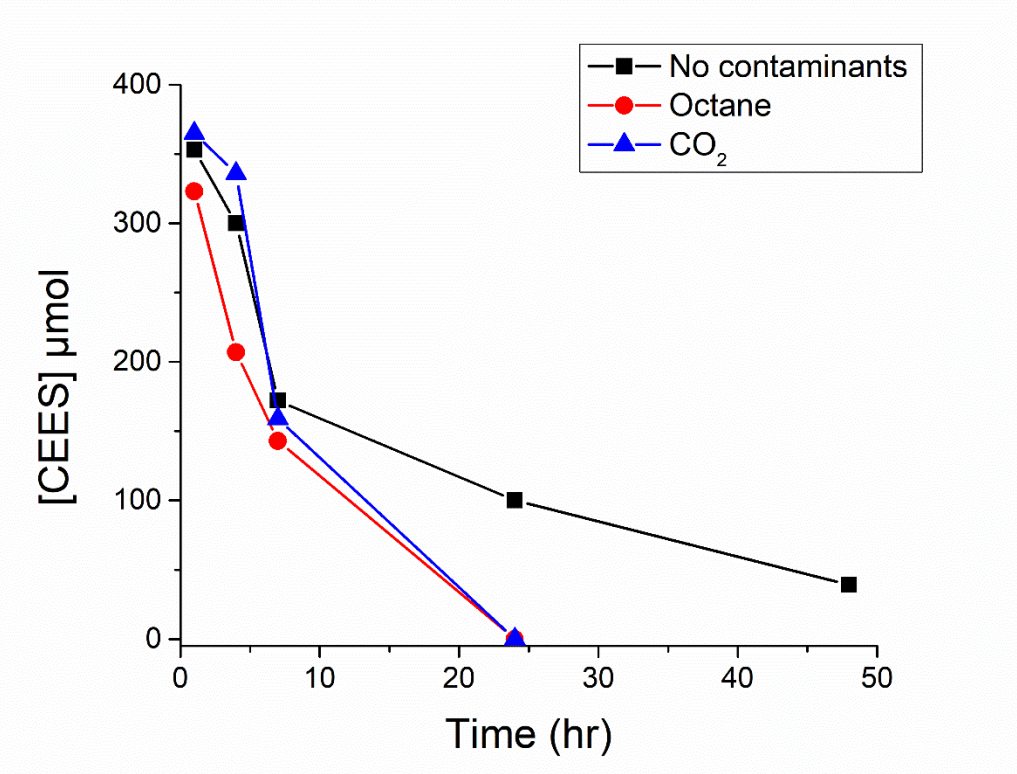

Figure 3.16. Kinetics of CEES oxidation with and without common battlefield contaminants. Conditions: 50 µL (430 µmol) of neat CEES was added directly to 25 mg of SFC (9.6 $TBABr_3$, 4.1 mg $TBANO_3$, 1.6 mg $Cu(NO_3)_2 \cdot 2H_2O$, 10 mg Nafion^{TM}), under 1 atm of air at ambient conditions. (Black) control with no battlefield contaminants; (red) in the presence of hydrocarbons, namely 40 µL (240 µmol) octane; and (blue) with 150 µL (6 µmol) CO_2 in a 1:1 ratio with Cu^{2+}.

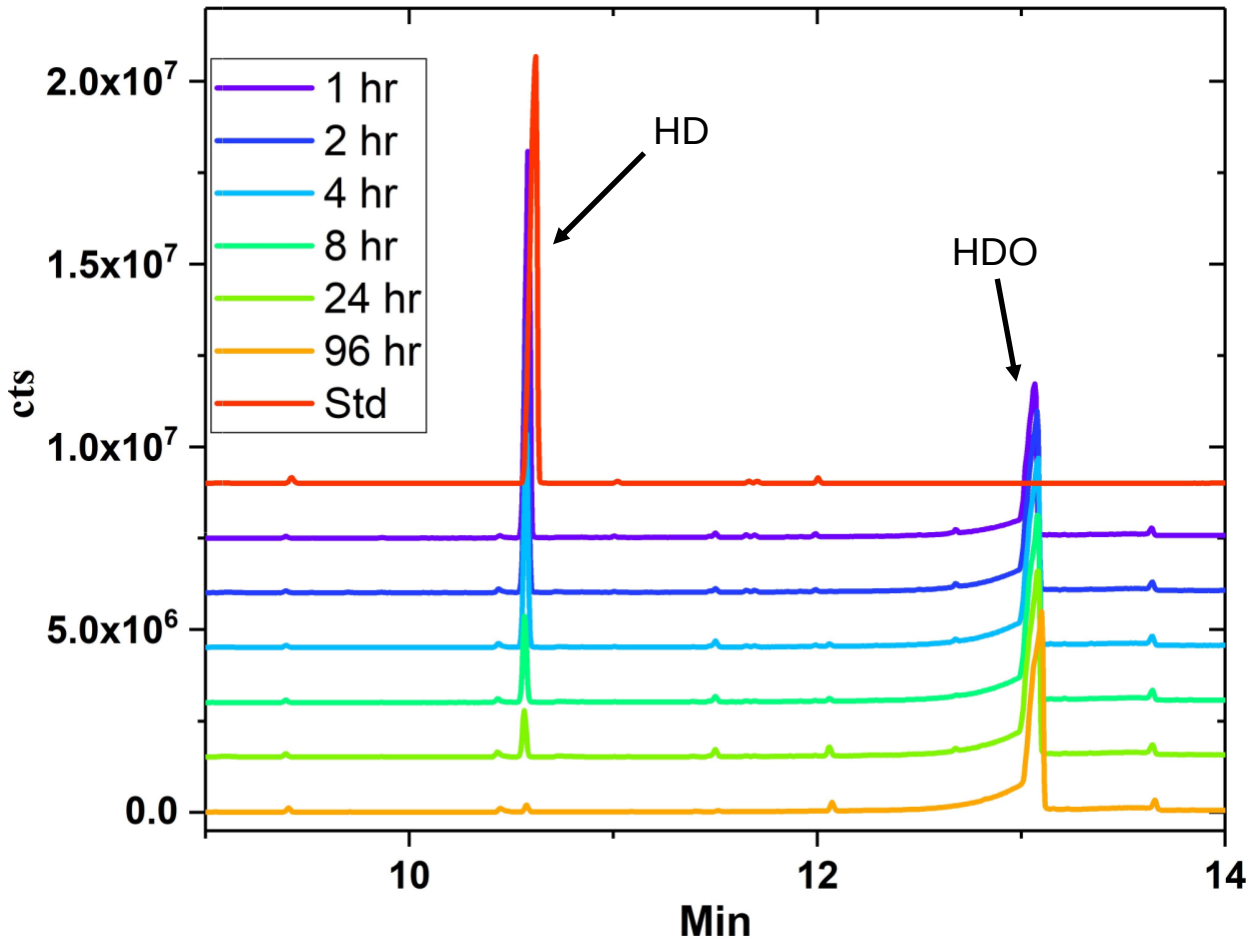

Figure 3.17. GC-MS spectra of live agent HD oxidation kinetics catalyzed by **SFC**. Conditions: 5 µL HD added directly to 5 mg **SFC** (10 turnovers based on Br_3^-). Reaction conducted in sealed vial with 20 mL syringe filled with O_2 as gas headspace at ambient temperature (~22 ºC). GC-MS measurements taken via 1.5 mL $CDCl_3$ extraction.

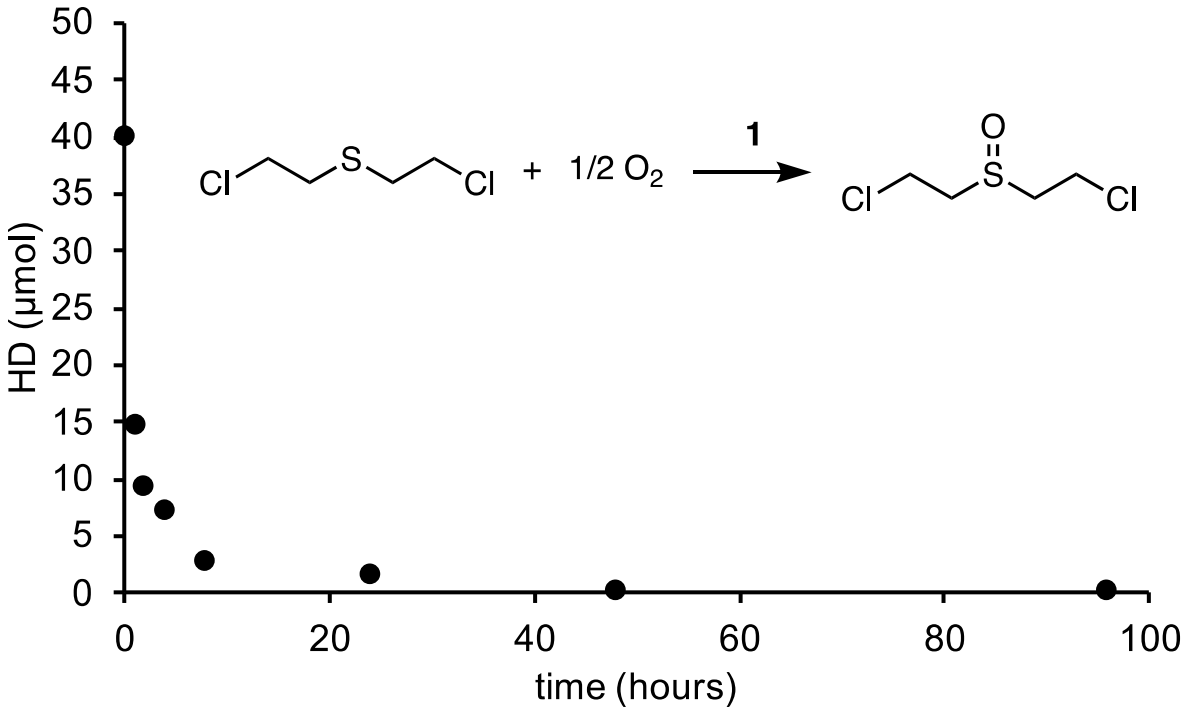

Figure 3.18. Kinetics of HD oxidation catalyzed by **SFC**. Conditions: 5 µL HD added directly to 5 mg of **SFC** at ambient temperature (22±1 ºC). Reaction conducted in sealed vial with a 20 mL syringe filled with O_2 as the headspace gas. GC-MS measurements were taken via 1.5 mL $CDCl_3$ extraction.

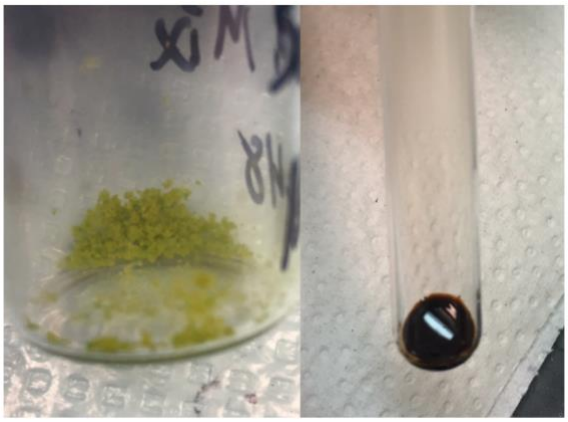

Figure 3.19. Responsive color change behavior in **SFC**. Left: **SFC** with Br_x/NO_x/Cu(II)/ Nafion^{TM} ratios of 5.0:3.3:1.7:2.3 respectively. Right: 25.3 mg of **SFC** exposed to 50 μL (430 μmol) of neat CEES.

Further evidence to support the catalytic nature of this material in neat agent/simulant was obtained using bromine X-ray absorption near edge structure (XANES) and extended X-ray absorption fine structure (EXAFS) spectroscopies. The bromine K-edge XANES shows that throughout the course of the reaction, the initial Br_3^- (characterized by a 1s-4p pre-edge peak at 13473 eV)[47-49] is consumed upon exposure to CEES and then reforms upon reaction completion (Figure 3.20) similar to what was observed for the studies done in acetonitrile. The EXAFS spectra (Figure 3.21) and quantitative analysis (Figure 3.22 and Table 3.1) also demonstrate regeneration of the tribromide, as evidenced by the preservation of the average Br-Br lengths of 2.55 ± 0.01 Å and 2.54 ± 0.01 Å before and after CEES exposure, respectively. Finally, copper K-edge EXAFS fitting indicates that, similar to the catalysis in acetonitrile, the coordination environment of the Cu centers switches from O to Br upon exposure to CEES (Figures 3.23, 3.24 and Table 3.2). This is consistent with Cu complexing bromide ions, which aides in the

formation of the reactive bromosulfonium intermediate. It also suggests that the role of copper for catalysis in acetonitrile remains the same in neat agent/simulant.

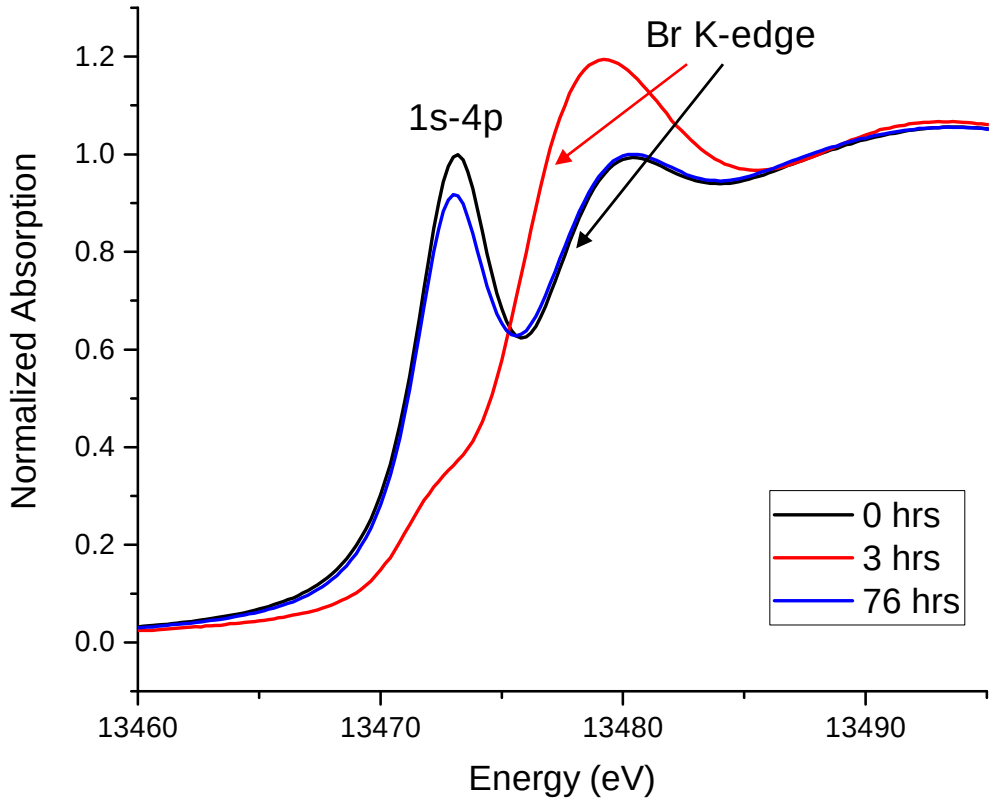

Figure 3.20. Bromine K-edge XANES on 30 mg of SFC exposed to 50 µL of liquid CEES placed directly on the surface of SFC (18 turnovers based on Br_3^-) under air in a closed glass vial at ambient temperature (~22 ºC). Aliquots of the slurry mixture were loaded in Kapton capillaries for XANES measurements after 0 (black), 3 (red), and 76 (blue) hours. Arrows indicate the Br K-edges (black arrow corresponds to both blue and black curves).

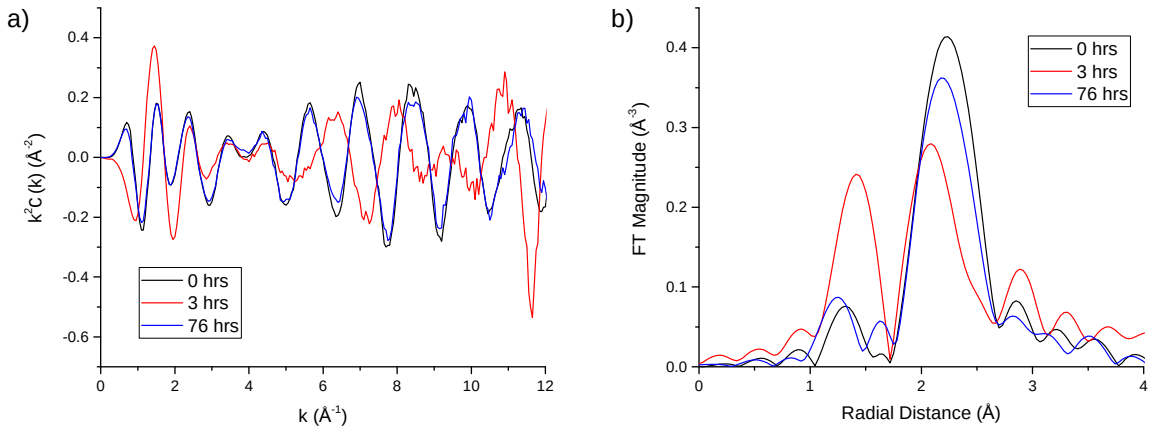

Figure 3.21. Bromine K-edge EXAFS on 30 mg of **SFC** exposed to 50 µL of liquid CEES under 1 atm of air in a closed glass vial at ambient temperature (22±1 ºC). Aliquots of the slurry mixture were loaded in Kapton capillaries for EXAFS measurements. Plots of both k-space (a) and r-space (b) data after 0 (black), 3 (red), and 76 (blue) hours. The r-space data was generated with a k-range from 3 $Å^{-1}$ to 12 $Å^{-1}$, with k^2-weighting in Fourier transforms.

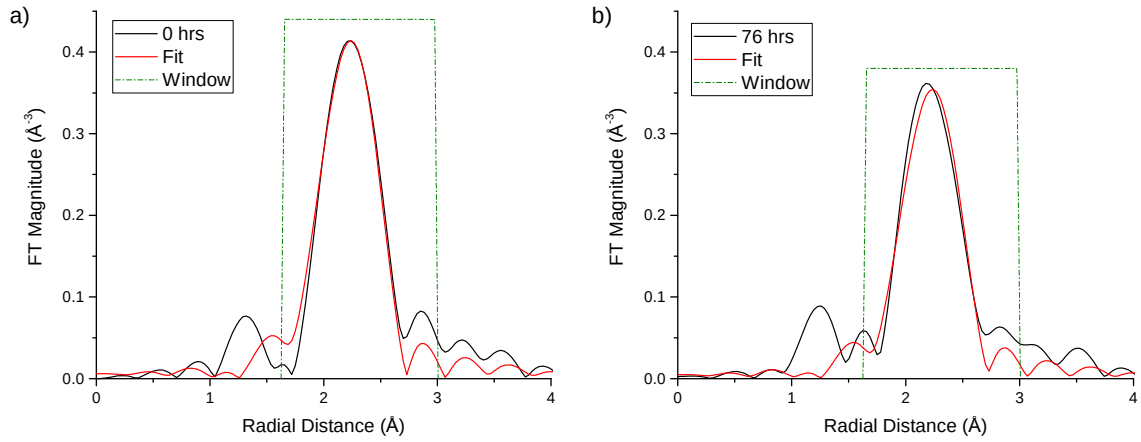

Figure 3.22. Fitting of bromine K-edge EXAFS data on 30 mg of **SFC** exposed to 50 µL of liquid CEES under ambient air in a closed glass vial. Aliquots of **SFC** were loaded in Kapton capillaries for EXAFS measurements both before CEES exposure (a) and after 76 hours (b).

	0-hour	**76-hour**
ΔE (eV)	9 ± 2	
N	1.3 ± 0.2	1.0 ± 0.2
R (Å)	2.55 ± 0.01	2.54 ± 0.01
σ^2 (Å^2)	0.006 ± 0.001	0.005 ± 0.002

Table 3.1. Values for Br-Br$_N$ coordination number (N), effective Br-Br interatomic distance (R), and mean squared bond length disorder (σ^2) based on analysis of bromine K-edge EXAFS on 30 mg of **SFC** exposed to 50 µL of liquid CEES under ambient air in a closed glass vial. The fitting was performed in r-space, using the k-range from 3 Å^{-1} to 12 Å^{-1}, with k^2-weighting in Fourier transforms. Aliquots of **SFC** were loaded in Kapton capillaries for EXAFS measurements both before CEES exposure and after 76 hours. The energy origin correction, ΔE, was constrained in the fit to be the same for the two data sets.

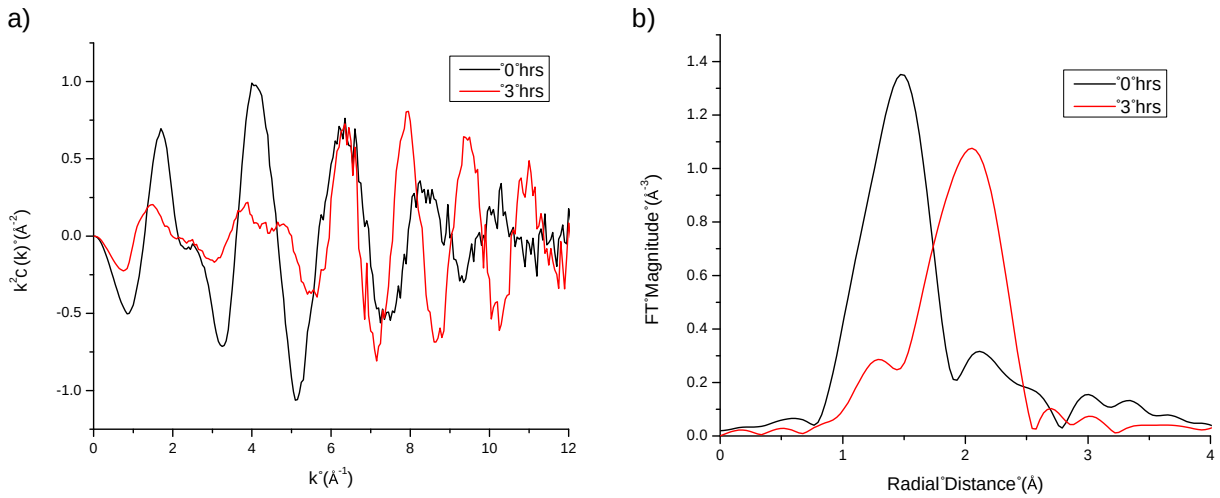

Figure 3.23. Copper K-edge EXAFS on 30 mg of **1** exposed to 50 µL of liquid CEES under 1 atm of air in a closed glass vial at ambient temperature (22±1 ºC). Aliquots of the slurry mixture were loaded in Kapton capillaries for EXAFS measurements. Plots of both k-space (a) and r-space (b) data after 0 (black) and 3 (red) hours. The r-space data was generated with a k-range from 2 $Å^{-1}$ to 12 $Å^{-1}$, with k^2-weighting in Fourier transforms.

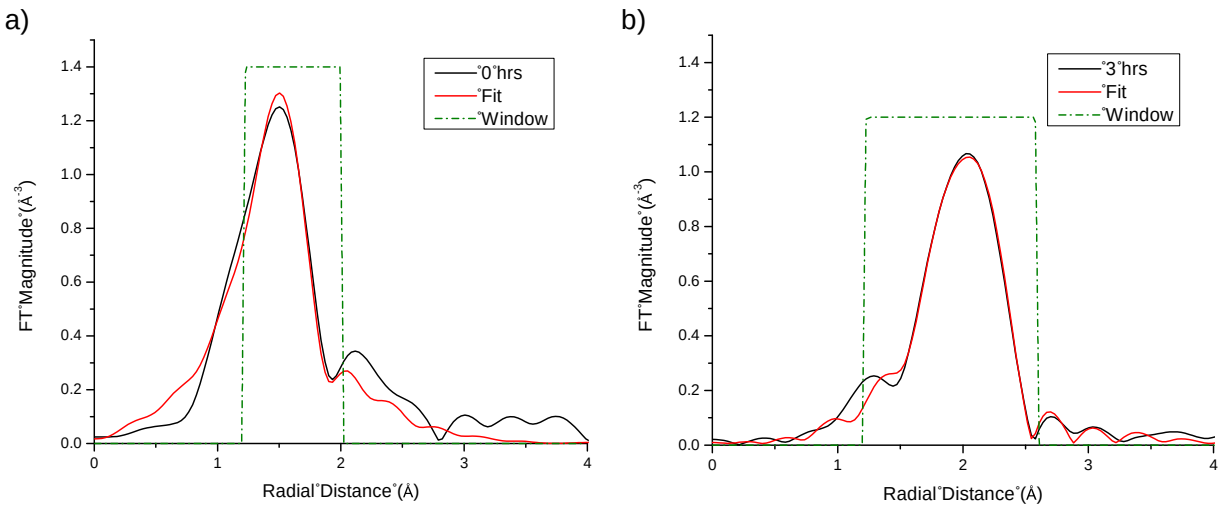

Figure 3.24. Fitting of copper K-edge EXAFS data on 30 mg of **1** exposed to 50 µL of liquid CEES under ambient air in a closed glass vial. Aliquots of **1** were loaded in Kapton capillaries for EXAFS measurements both before CEES exposure (a) and after 3 hours (b).

	0-hour	**3-hour**
N_O	4.8 ± 0.6	-
R_O (Å)	1.95 ± 0.01	-
σ^2_O (Å^2)	0.006 ± 0.001	-
N_{Br}	-	3.3 ± 0.7
R_{Br} (Å)	-	2.37 ± 0.01
σ^2_{Br} (Å^2)	-	0.007 ± 0.001
N_S	-	1.0 ± 0.4
R_S (Å)	-	2.33 ± 0.03
σ^2_S (Å^2)	-	0.007 ± 0.001

Table 3.2. Values for coordination number (N), effective interatomic distance (R), and mean squared bond length disorder (σ^2) for Cu-O/Br/S bonds based on analysis of bromine K-edge EXAFS on 30 mg of **1** exposed to 50 µL of liquid CEES under ambient air in a closed glass vial. The fitting was performed in r-space, using the k-range from 3 Å^{-1} to 12 Å^{-1}, with k^2-weighting in Fourier transforms. Aliquots of **1** were loaded in Kapton capillaries for EXAFS measurements both before CEES exposure and after 3 hours. The energy origin correction, ΔE, for Cu-O and Cu-Br/S bonds were different variables, which were 4.1 ± 1.5 and 0.2 ± 1.1, respectively. σ^2 was set to be same for Cu-Br and Cu-S bonds.

In addition to exhibiting catalytic turnover with liquid HD/CEES, a significant advantage of this system is that it retains this activity against vapor phase agent/simulant. When **SFC** is exposed to saturated CEES vapor, there is a loss of the tribromide peak in the Br K-edge XANES spectra (Figure 3.25) demonstrating reactivity with **SFC**. For live agent testing, we exposed

SFC to a vapor stream of HD, monitoring changes to the material by diffuse reflectance infrared Fourier transform spectroscopy (DRIFTS). As indicated by peaks such as the one at 1300 cm^{-1}, corresponding to the HD-based CH_2 wag, there is an initial physisorption of HD over time. The peaks at 1083 and 1041 cm^{-1}, which also increase with time, are consistent with an S=O bond providing evidence for sulfoxide (HDO) product formation (Figure 3.26). Immediately following the DRIFTS experiment, the HDO assignment was confirmed by GC-MS (Figure 3.27). Thus, the solid catalyst, **SFC**, clearly decontaminates both vapor and liquid HD in the ambient environment.

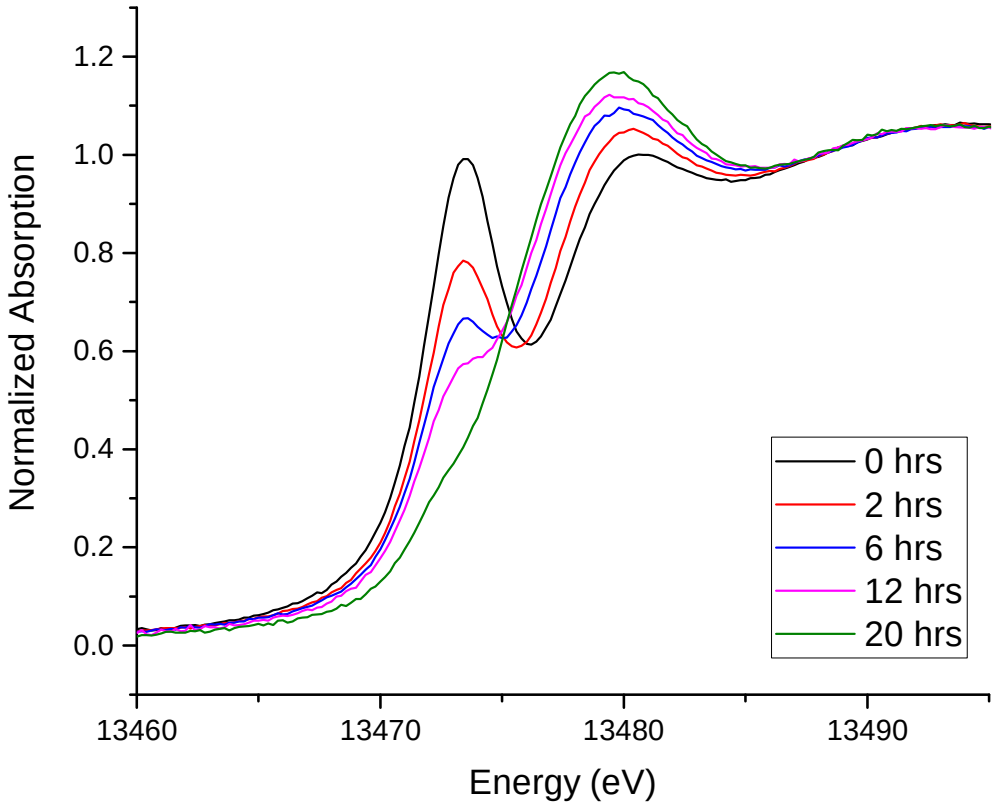

Figure 3.25. Bromine K-edge XANES of **SFC** exposed to saturated CEES vapor in a sealed jar. Measurements were taken at different time intervals following initial CEES exposure. The solid catalyst, **SFC**, was packed in Kapton capillaries (ID: 0.11049 cm). Grey arrows indicate the direction of change as a function of time.

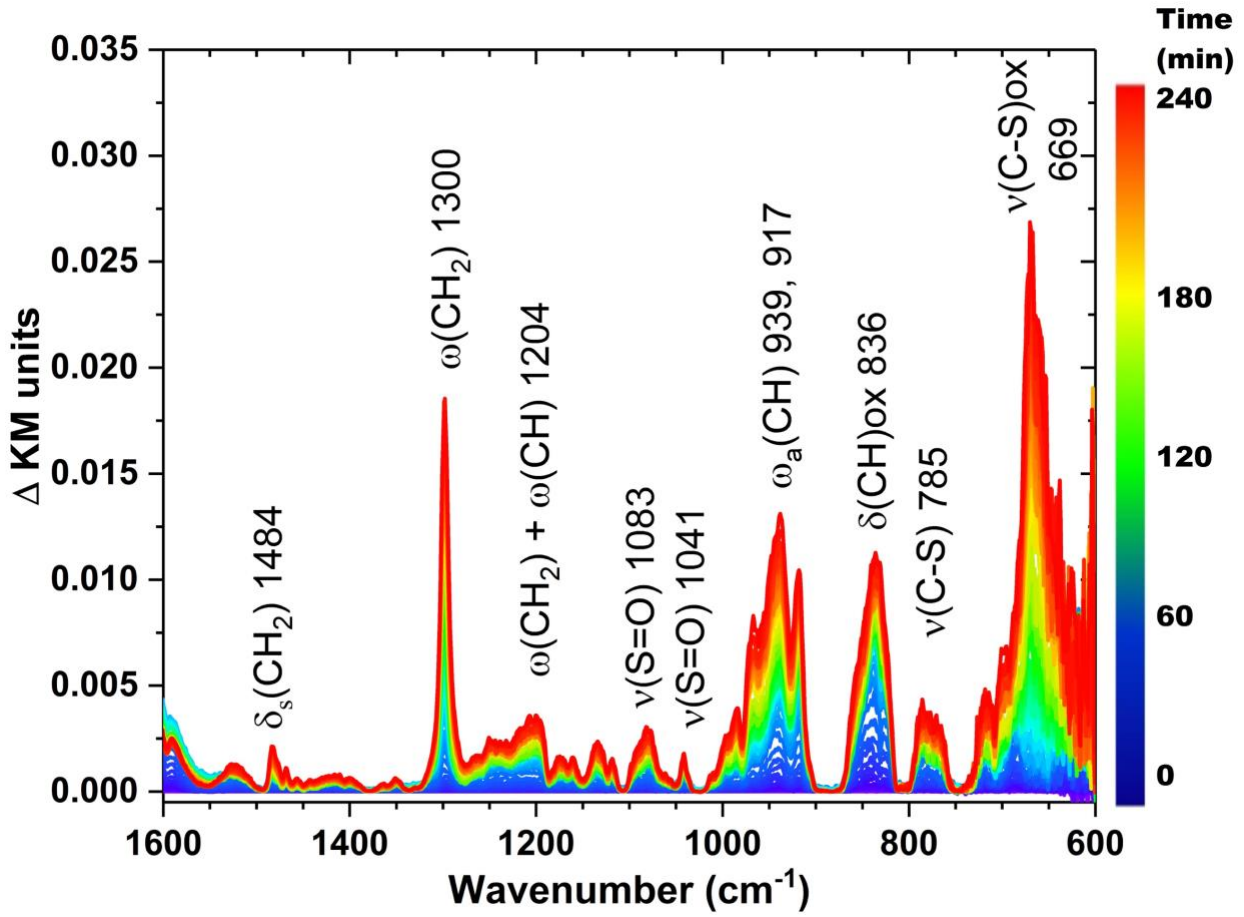

Figure 3.26. DRIFTS spectra of HD oxidation catalyzed by **SFC**. Conditions: **SFC** placed in a DRIFTS cup exposed to HD vapor in a gas stream of 2% relative humidity/Zero Air for 4 hours.

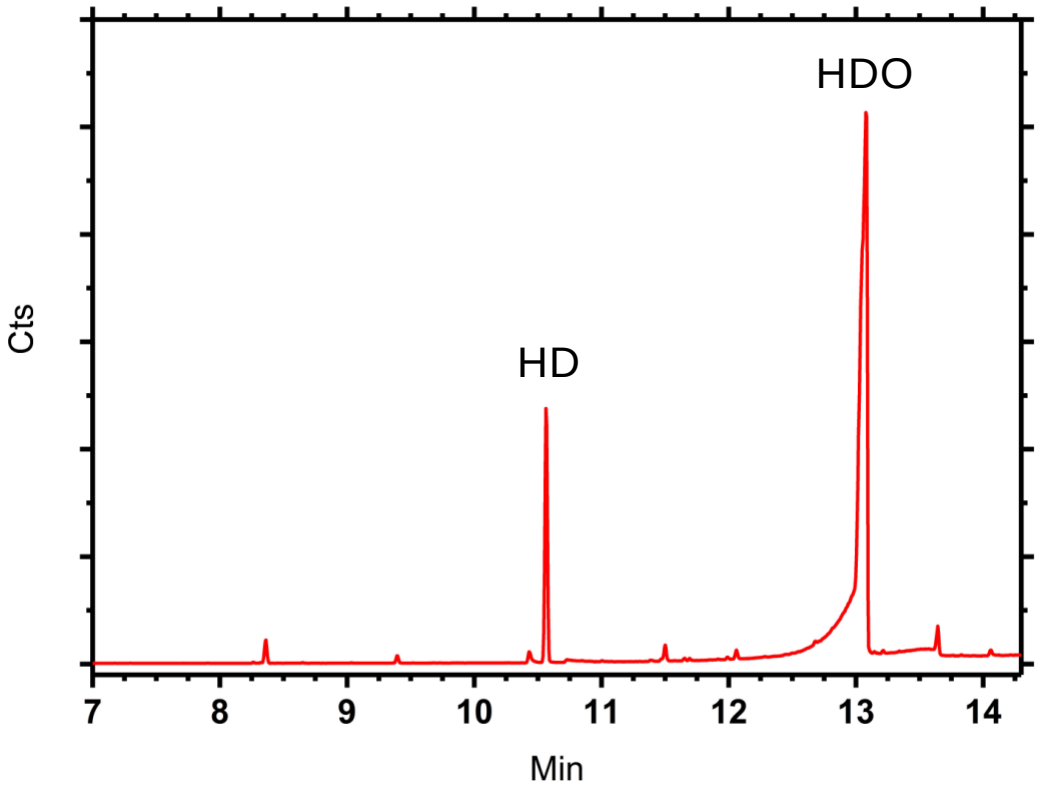

Figure 3.27. GC-MS spectra immediately following the DRIFTS experiment of HD oxidation catalyzed by **SFC** (Figure 3.26). Conditions: **SFC** placed in a DRIFTS cup exposed to HD vapor in a gas stream of 2% relative humidity/Zero Air for 4 hours. GC-MS measurement taken via a 1.5 mL $CDCl_3$ extraction.

3.4 Conclusion

In summary, we report the development of a highly reactive solid material for the selective, catalytic, air-based oxidation of HD to decontaminated HDO at ambient conditions. The design of this solvent-free catalyst was informed by mechanistic studies of the homogeneous catalytic system in solution. Cu(II) significantly increases the reaction rate and simultaneously facilitates a colorimetric detection of HD. Several experiments establish that the key intermediate in aerobic sulfoxidation, the bromosulfonium ion, is formed reversibly and that a central role of Cu(II) in acceleration this process is to increase the concentration of the

bromosulfonium during catalytic turnover. These insights resulted in the development of a solid formulation that is active against both liquid and vapor HD. For these solvent-free reactions, the use of XAFS and DRIFTS enabled monitoring of the reaction under turnover conditions along with comparisons to the mechanistic studies conducted in acetonitrile. Collectively, these findings mark substantial progress toward the effective decontamination of HD, as well as our understanding of sulfide oxidation using $Br_y/NO_x/O_2$ systems.

3.5 References

1. Mashkina, A. V., Catalytic Synthesis of Sulfoxides and Sulfones Via Oxidation of Sulfides by Molecular Oxygen. *Catalysis Reviews* **1990,** *32* (1-2), 105-161.

2. Uematsu, T.; Miyamoto, Y.; Ogasawara, Y.; Suzuki, K.; Yamaguchi, K.; Mizuno, N., Molybdenum-doped α-MnO2 as an efficient reusable heterogeneous catalyst for aerobic sulfide oxygenation. *Catalysis Science & Technology* **2016,** *6* (1), 222-233.

3. Carreno, M. C., Applications of Sulfoxides to Asymmetric Synthesis of Biologically Active Compounds. *Chem. Rev.* **1995,** *95* (6), 1717-1760.

4. Fernández, I.; Khiar, N., Recent Developments in the Synthesis and Utilization of Chiral Sulfoxides. *Chem. Rev.* **2003,** *103* (9), 3651-3706.

5. Kaczorowska, K.; Kolarska, Z.; Mitka, K.; Kowalski, P., Oxidation of sulfides to sulfoxides. Part 2: Oxidation by hydrogen peroxide. *Tetrahedron* **2005,** *61* (35), 8315-8327.

6. Kowalski, P.; Mitka, K.; Ossowska, K.; Kolarska, Z., Oxidation of sulfides to sulfoxides. Part 1: Oxidation using halogen derivatives. *Tetrahedron* **2005,** *61* (8), 1933-1953.

7. Yang, Y. C.; Baker, J. A.; Ward, J. R., Decontamination of Chemical Warfare Agents. *Chem. Rev.* **1992,** *92* (8), 1729-1743.

8. Szinicz, L., History of chemical and biological warfare agents. *Toxicology* **2005,** *214* (3), 167-181.

9. Ghabili, K.; Agutter, P. S.; Ghanei, M.; Ansarin, K.; Panahi, Y.; Shoja, M. M., Sulfur mustard toxicity: History, chemistry, pharmacokinetics, and pharmacodynamics. *Critical Reviews in Toxicology* **2011,** *41* (5), 384-403.

10. Talmage, S. S.; Watson, A. P.; Hauschild, V.; Munro, N. B.; King, J., Chemical Warfare Agent Degradation and Decontamination. *Curr. Org. Chem.* **2007,** *11* (3), 285-298.

11. Jang, Y. J.; Kim, K.; Tsay, O. G.; Atwood, D. A.; Churchill, D. G., Update 1 of: Destruction and Detection of Chemical Warfare Agents. *Chem. Rev.* **2015,** *115* (24), PR1-PR76.

12. Black, R., CHAPTER 1 Development, Historical Use and Properties of Chemical Warfare Agents. In *Chemical Warfare Toxicology: Volume 1: Fundamental Aspects*, The Royal Society of Chemistry: 2016; Vol. 1, pp 1-28.

13. Wagner, G. W.; Yang, Y.-C., Rapid Nucleophilic/Oxidative Decontamination of Chemical Warfare Agents. *Ind. Eng. Chem. Res.* **2002,** *41* (8), 1925-1928.

14. *Process Intensification for Green Chemistry*. John Wiley & Sons: 2013.

15. Anastas, P.; Eghbali, N., Green Chemistry: Principles and Practice. *Chem. Soc. Rev.* **2010,** *39* (1), 301-312.

16. Sullivan, K. P.; Neiwert, W. A.; Zeng, H.; Mehta, A. K.; Yin, Q.; Hillesheim, D. A.; Vivek, S.; Yin, P.; Collins-Wildman, D. L.; Weeks, E. R.; Liu, T.; Hill, C. L., Polyoxometalate-based gelating networks for entrapment and catalytic decontamination. *Chemical Communications* **2017,** *53* (83), 11480-11483.

17. Hiscock, J. R.; Bustone, G. P.; Clark, E. R., Decontamination and Remediation of the Sulfur Mustard Simulant CEES with "Off-the-Shelf" Reagents in Solution and Gel States: A Proof-of-Concept Study. *ChemistryOpen* **2017,** *6* (4), 497-500.

18. Liu, Y.; Buru, C. T.; Howarth, A. J.; Mahle, J. J.; Buchanan, J. H.; DeCoste, J. B.; Hupp, J. T.; Farha, O. K., Efficient and selective oxidation of sulfur mustard using singlet oxygen generated by a pyrene-based metal–organic framework. *J. Mater. Chem. A* **2016,** *4* (36), 13809-13813.

19. Punniyamurthy, T.; Velusamy, S.; Iqbal, J., Recent Advances in Transition Metal Catalyzed Oxidation of Organic Substrates with Molecular Oxygen. *Chem. Rev.* **2005,** *105* (6), 2329-2364.

20. Weinstock, I. A.; Schreiber, R. E.; Neumann, R., Dioxygen in Polyoxometalate Mediated Reactions. *Chem. Rev.* **2018,** *118* (5), 2680-2717.

21. Ghorbani-Choghamarani, A.; Azadi, G.; Tahmasbi, B.; Hadizadeh-Hafshejani, M.; Abdi, Z., Practical And Versatile Oxidation Of Sulfides Into Sulfoxides And Oxidative Coupling Of Thiols Using Polyvinylpolypyrrolidonium Tribromide. *Phosphorus, Sulfur, and Silicon and the Related Elements* **2014,** *189* (4), 433-439.

22. Gogoi, P.; Hazarika, S.; Barman, P., Tetrabutylammonium tribromide impregnated MCM-48 as a heterogeneous catalyst for selective oxidation of sulfides. *RSC Advances* **2015,** *5* (48), 38044-38047.

23. Otokesh, S.; Kolvari, E.; Amoozadeh, A.; Koukabi, N., Magnetic nanoparticle-supported imidazole tribromide: a green, mild, recyclable and metal-free catalyst for the oxidation of sulfides to sulfoxides in the presence of aqueous hydrogen peroxide. *RSC Advances* **2015,** *5* (66), 53749-53756.

24. Kar, G.; Saikia, A. K.; Bora, U.; Dehury, S. K.; Chaudhuri, M. K., Synthesis of cetyltrimethylammonium tribromide (CTMATB) and its application in the selective oxidation of sulfides to sulfoxides. *Tetrahedron Lett.* **2003,** *44* (24), 4503-4505.

25. Le, N. H.; Han, Y.-h.; Ryu, S. G.; Cho, J., Mechanistic reaction model for oxidation of sulfur mustard simulant by a catalytic system of nitrate and tribromide. *J. Hazard. Mater.* **2019,** *365*, 511-518.

26. Luo, Z.; Geletii, Y. V.; Hillesheim, D. A.; Wang, Y.; Hill, C. L., Mechanistic Studies of O2-Based Sulfoxidations Catalyzed by NOx/Br Systems. *ACS Catalysis* **2011,** *1* (10), 1364-1370.

27. Hong Le, N.; Han, Y.-h.; Jung, H.; Cho, J., Catalytic reaction system for rapid selective oxidation of alkyl sulphide. *J. Hazard. Mater.* **2019,** *379*, 120830.

28. Popiel, S.; Witkiewicz, Z.; Szewczuk, A., The GC/AED studies on the reactions of sulfur mustard with oxidants. *J. Hazard. Mater.* **2005,** *123* (1), 94-111.

29. Ravel, B.; Newville, M., ATHENA, ARTEMIS, HEPHAESTUS: data analysis for X-ray absorption spectroscopy using IFEFFIT. *Journal of Synchrotron Radiation* **2005,** *12* (Pt 4), 537-41.

30. Newville, M., IFEFFIT: interactive XAFS analysis and FEFF fitting. *Journal of Synchrotron Radiation* **2001,** *8*, 322-324.

31. Bryliakov, K. P., Catalytic Asymmetric Oxygenations with the Environmentally Benign Oxidants H2O2 and O2. *Chem. Rev.* **2017,** *117* (17), 11406-11459.

32. Allen, S. E.; Walvoord, R. R.; Padilla-Salinas, R.; Kozlowski, M. C., Aerobic Copper-Catalyzed Organic Reactions. *Chem. Rev.* **2013,** *113* (8), 6234-6458.

33. Martín, S. E.; Rossi, L. I., An efficient and selective aerobic oxidation of sulfides to sulfoxides catalyzed by $Fe(NO_3)_3$–$FeBr_3$. *Tetrahedron Lett.* **2001,** *42* (41), 7147-7151.

34. Kinen, C. O.; Rossi, L. I.; de Rossi, R. H., Mechanism of the Selective Sulfide Oxidation Promoted by HNO3/FeBr3. *The Journal of Organic Chemistry* **2009,** *74* (18), 7132-7139.

35. Rossi, L. I.; Martín, S. E., Possible role of nitrate/nitrite redox cycles in catalytic and selective sulfoxidation reaction: Metallic nitrates and bromides as redox mediators: a comparative study. *Applied Catalysis A: General* **2003,** *250* (2), 271-278.

36. Miotti, U.; Modena, G.; Sedea, L., Mechanism of formation of alkyl aryl sulphoxides by oxidation of alkyl aryl sulphides with bromine. *Journal of the Chemical Society B: Physical Organic* **1970,** (0), 802-805.

37. Ali, M. H.; Stricklin, S., Oxidation of Sulfides with Pyridinium Tribromide in the Presence of Hydrated Silica Gel. *Synth. Commun.* **2006,** *36* (12), 1779-1786.

38. Scaife, D. B.; Tyrrell, H. J. V., 71. Equilibrium constants for the reaction between bromine and bromide ions at 5°, 25°, and 35° in aqueous medium of constant ionic strength and acidity. *Journal of the Chemical Society (Resumed)* **1958,** (0), 386-392.

39. Allen, G. D.; Buzzeo, M. C.; Villagrán, C.; Hardacre, C.; Compton, R. G., A mechanistic study of the electro-oxidation of bromide in acetonitrile and the room temperature ionic liquid, 1-butyl-3-methylimidazolium bis(trifluoromethylsulfonyl)imide at platinum electrodes. *J. Electroanal. Chem.* **2005,** *575* (2), 311-320.

40. Iwasita, T.; Giordano, M. C., Kinetics of the bromine-tribromide-bromide redox processes on platinum electrodes in acetonitrile solutions. *Electrochim. Acta* **1969,** *14* (10), 1045-1059.

41. Côrtes, C. E. S.; Faria, R. B., Kinetics and Mechanism of Bromate−Bromide Reaction Catalyzed by Acetate. *Inorganic Chemistry* **2004,** *43* (4), 1395-1402.

42. Olshin, P. K.; Myasnikova, O. S.; Kashina, M. V.; Gorbunov, A. O.; Bogachev, N. A.; Kompanets, V. O.; Chekalin, S. V.; Pulkin, S. A.; Kochemirovsky, V. A.; Skripkin, M. Y.; Mereshchenko, A. S., The electronic spectra and the structures of the individual copper(II) chloride and bromide complexes in acetonitrile according to steady-state absorption spectroscopy and DFT/TD-DFT calculations. *Chem. Phys.* **2018,** *503*, 14-19.

43. Barnes, J. C.; Hume, D. N., Copper(II) Bromide Complexes. I. A Spectrophotometric Study. *Inorganic Chemistry* **1963,** *2* (3), 444-448.

44. Persson, I.; Dashi, K. C.; Kinjo, Y., Equilibrium and Enthalpy Measurements on the Zinc (II) Chloride, Bromide and Iodide Systems in Aoetonitrile and Pyridine, and on the Mercury (II) Chloride, Bromide and Iodide Systems in. *Acta Chemica Scandinaviea* **1990,** *44*, 433-442.

45. Feilchenfeld, H.; Manor, S.; Epstein, J. A., Kinetics of oxidation of hydrobromic acid by nitric acid in the presence of nitrous acid. *Journal of the Chemical Society, Dalton Transactions* **1972,** (23), 2675-2680.

46. Blair, C. M.; Brass, P. D.; Yost, D. M., The Equilibrium between Nitric Oxide, Bromine and Nitrosyl Bromide. *J. Am. Chem. Soc.* **1934,** *56* (9), 1916-1918.

47. El Nahhas, A.; van der Veen, R. M.; Penfold, T. J.; Pham, V. T.; Lima, F. A.; Abela, R.; Blanco-Rodriguez, A. M.; Záliš, S.; Vlček, A.; Tavernelli, I.; Rothlisberger, U.; Milne, C. J.; Chergui, M., X-ray Absorption Spectroscopy of Ground and Excited Rhenium–Carbonyl–Diimine Complexes: Evidence for a Two-Center Electron Transfer. *J. Phys. Chem. A* **2013,** *117* (2), 361-369.

48. Uno, K.; Notoya, Y.; Fujikawa, T.; Yoshikawa, H.; Nishikawa, K., Br K-Edge X-ray Absorption Near Edge Structure Analyses of Bromine Residue Carbon Compounds Using Full Multiple-Scattering Theory. *Japanese Journal of Applied Physics* **2005,** *44* (6A), 4073-4079.

49. Leri, A. C.; Hakala, J. A.; Marcus, M. A.; Lanzirotti, A.; Reddy, C. M.; Myneni, S. C. B., Natural organobromine in marine sediments: New evidence of biogeochemical Br cycling. *Global Biogeochem. Cycles* **2010,** *24* (4).

Chapter 4: A Dual-Purpose Atomic Layer Deposition Metal Oxide Coating for Photoelectrochemical Water Oxidation

with contributions from

Brandon Piercy, Yumin He, Dunwei Wang, Mark Losego, and Craig Hill

4.1 Introduction

One of the greatest scientific challenges facing our world today is how to keep pace with global energy demands without continuing to damage our environment through excessive greenhouse gas emissions. It is projected that global energy consumption will continue grow from its present value of 13.5 Terawatts (TW), to either 27 or 40.8 TW in 2050 depending on the model.[1] As of 2012, 81.7% of this energy was generated from the burning of fossil fuels.[2] Since the industrial revolution, this heavy reliance on the burning of fossil fuels has driven carbon dioxide levels from between 210-300 parts per million (ppm) over the last 420,000 years, to 412.55ppm as of September 2020.[3] Based on current rates of fossil fuel consumption, and accounting for increases in energy demand, atmospheric levels of CO_2 could reach 750ppm by the year 2050, a value probably not present on earth for the last 20 million years.[1] Data from the Vostok ice cores in Antarctica show the clear correlation between temperature and CO_2 levels[4] indicating that global temperatures will continue to rise over the next century resulting in numerous deleterious environmental effects. For this reason it is imperative that the scientific community find a solution that can provide clean energy for the world.

Of the possible carbon emission free energy sources, solar energy is the most promising. Nuclear energy, for example, is not a viable option because there is only sufficient uranium in the earth's crust to sustain our global energy budget for 30 years.[1] Energy sources such as geothermal and wind, while effective and helpful, are not widespread enough to completely replace the burning of fossil fuels. On the other hand, solar energy hits the earth with a power of 120,000 TW.[5] In just one hour enough energy from the sun hits the earth's surface to power the world for a year.[1]

Given that terrestrial sunlight is the obvious choice for a clean energy source, the next step is to determine the means of capturing and storing solar energy. In all cases given that solar energy is intermittent, the means of storing the energy will be a key consideration. One method involves the direct conversion of light energy to electrical energy through photovoltaic cells.[6] Here the energy is stored as a chemical potential in batteries, however, current battery technology is not yet sufficiently advanced to support the entire global energy demand, nor does it possess the energy density required to power vehicles such as airplanes and large cargo ships. Another method of solar energy capture converts light energy into thermal energy, which can be then used to drive a conventional steam turbine.[7] This process is hindered by the fact that it its difficult to store high temperature substances efficiently over long periods of time.

The last method is in theory the most promising as it uses the light energy to form new molecules storing the energy as chemical bonds rather than as thermal, mechanical, or electrical energy. The resulting compounds, stored under the proper conditions, are theoretically stable indefinitely. These new molecules or "solar fuels," can then be burned on demand to recapture the stored energy making this a very attractive strategy. This process of capturing light energy and storing it in the form of chemical bonds, is of course not new, as it was developed by Nature over three billion years ago.[8] Like the natural process of photosynthesis, synthetic methods require catalysts for both oxidation and reduction reactions. Study of both reactions is ongoing; however, the remainder of this work will focus on the oxidative process. As in photosynthesis, this is the oxidation of water.

To achieve photo-driven water oxidation, one of the components required is an efficient light absorber and charge separator with sufficient energy to overcome the 1.23V (pH = 0) water oxidation potential. Numerous different light absorbers have been reported including II-VI and

III-V semiconductors, as well as molecular dyes.[9, 10] The biggest problem facing such devices is stability. While under illumination, semiconductor-based photoelectrochemical cells (PEC) can undergo photocorrosion when in direct contact with an electrolyte solution.[11-13] In the case of molecular dyes used in dye-sensitized solar cells (DSSC), the dye can be desorbed from the surface it is on. This desorption can be caused by many conditions including temperature, light intensity, and pH of the electrolyte.[14-16]

Fortunately, in the recent literature there is growing interest in using conformal nm-scale metal oxide layers deposited by atomic layer deposition (ALD) as a means to stabilize photo-electrodes. Nate Lewis and co-workers at Cal Tech have shown examples of both II-VI and III-V semiconductors protected by ALD deposited TiO_2 driving water oxidation.[11-13] At UNC Chapel Hill, Thomas Meyer has demonstrated the use of Al_2O_3 ALD to stabilize ruthenium-based dyes on TiO_2 surfaces.[14-16]

In addition to a stable and efficient light absorber photo-driven water oxidation requires the use of an efficient catalyst. Polyoxometalates (POMs) are a class of molecular metal oxide compounds capable of coordinating a wide variety of redox active metal centers used for catalysis. As such, these clusters have been examined extensively for water oxidation catalysis due to their oxidative stability, and highly tunable properties.[17-23] Given that POMs are polyanions, they readily bind to positively charged surfaces. This phenomenon was first demonstrated by binding $[(Fe^{III}(OH_2)_2)_3(A\text{-}r\text{-}PW_9O_{34})_2]^{9-}$ to cationic silica/alumina nanoparticles.[24] Hill and co-workers have since developed several schemes binding POM WOCs to cationic organic ligands generating heterogeneous water oxidation systems.[25, 26] While these methods were effective, an entirely inorganic system would be preferable given the harsh oxidative conditions required for water oxidation.

A general material property of metal oxides is that they all exhibit surface charges that are pH dependent. Each one has a specific pH at which the surface charge is neutral known as the point of zero charge (PZC).[27] Below this pH the surface is protonated leaving it positively charged. In theory an anionic POM should bind directly to this positively charged surface at pH values below the PZC.

This work proposes the generation of a novel system that incorporates a dual functioning metal oxide coating to both mitigate the photocorrosion of a semiconductor light absorber while also providing a positively charged surface on which to bind a POM WOC at the proper pH. Scheme 4.1 shows the proposed system that incorporates a cadmium sulfide quantum dot film as the light absorber coated with a metal oxide layer. The metal oxides examine are TiO_2, Al_2O_3, and ZnO. To the metal oxide surface, the water oxidation catalyst, $Rb_8K_2[\{Ru_4(OH)_2(H_2O)_4\}(\gamma\text{-}SiW_{10}O_{34})_2]$, is bound. This particular POM WOC was selected because it has a very wide pH range of stability and wide pH range of catalytic water oxidation activity. Cadmium sulfide quantum dots (CdS QDs) are the target light absorber as they have extremely high molar absorptivities, the absorption band edge is tunable,[28] and the stability of the film can easily be monitored via UV-vis to determine the efficacy of the protective metal oxide coating.

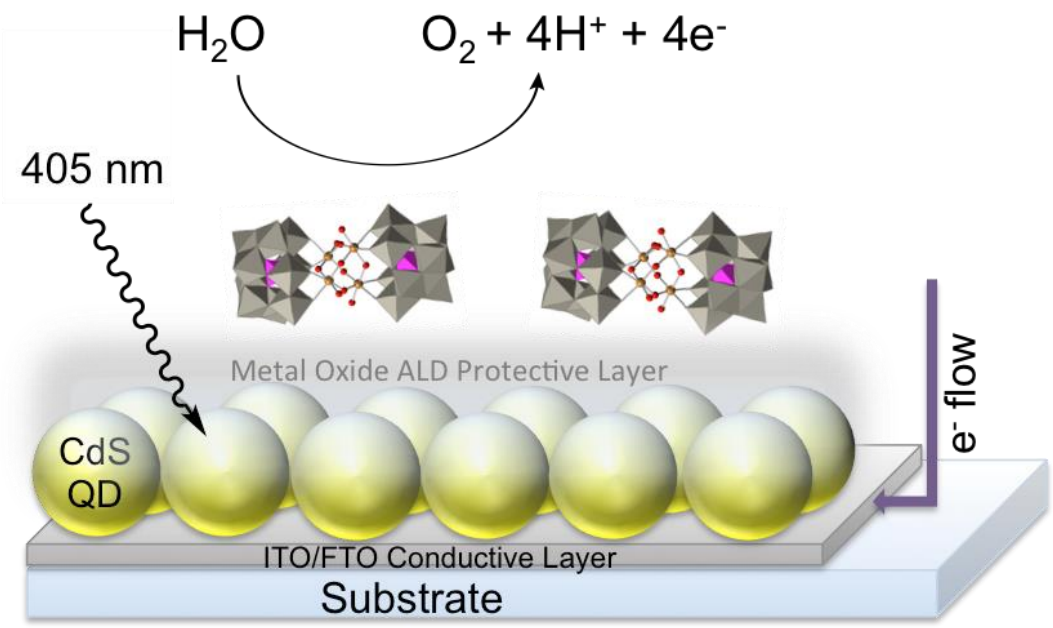

Scheme 4.1. The proposed electrode scheme depicted in a cross-sectional view. The gray shading represents the conformal metal oxide coating.

4.2 Experimental

4.2.1 Photoanode Film Preparation

Cadmium Sulfide (CdS) Colloidal Quantum Dot (QD) Synthesis: Cadmium oxide (0.1024 g) in octadecene (24 mL) and oleic acid (12 mL) was heated to 100 °C under vacuum for 10 minutes and then backfilled with argon. The solution was then heated to 250 °C at which point a mixture of sulfur (0.032 g) in octadecene (2 mL) was injected to initiate crystal growth. After 20 s, the reaction was quenched by injecting the solution with room temperature octadecene (15 mL) and subsequent placement in a water bath. The quantum dots were purified by precipitation in ethanol and then dissolved in chloroform.

Spin Coating of CdS QDs: The spin-coating was carried out at 2000 rpm by sequentially dripping 5% 1,2 ethanedithiol mixed in acetonitrile (2 drops), followed acetonitrile (1 drop), followed by the CdS quantum dots dispersed in chloroform (3 drops), followed by chloroform (1

drop) onto the center of the spinning FTO slide. These steps were repeated continuously for 20 min before placing the film in an oven at 130 °C for 1 hour.

4.2.2 Photoelectrochemical Measurements

Photoelectrochemical Cell Setup: All photoelectrochemical experiments were carried out in a 3-neck quartz flask with a flat optical window. The flask was filled with 50mL of pH 8.5 borate buffer with 0.5M Na_2SO_4 as the electrolyte. A platinum wire was used at the counter electrode. The reference electrode was a Ag/AgCl electrode stored in 1M KCl. A teflon coated stirbar was used to agitate the solution. The light source was a 405nm LED that was focused to an area larger than the films to insure complete illumination of the film using two confocal focusing lenses yielding a power density of 8.9 mW/cm^2. This value was measured with a power meter accounting for the aperture of the power meter. Electrochemical measurements were obtained with a wavedriver potentiostat.

Photoelectrochemistry Experiments: Each film was subjected to the following protocol. Between each test the cell was stirred to help remove any surface charging effects. An open circuit potential (OCP) was measured to determine the starting potential for cyclic voltammetry (CV). A CV scan was taken from the OCP out to 750mV vs. Ag/AgCl in the dark. The room lights were kept out using blackout curtain. Next a bulk electrolysis (BE) experiment was run holding the potential at 750mV for 10 minutes. This process of taking an OCP, CV and BE was repeated only this time under illumination from the LED.

4.3 Results and Discussion

CdS QDs were synthesized following the standard procedure developed by Peng and co-workers.[29] Figure 4.1 shows an ultraviolet-visible (UV-vis) spectrum with a band edge

absorption at 448nm. Based on a relationships developed by Peng and co-workers this corresponds to a nanocrystal diameter of 5.2nm.[30] The transmission electron microscopy image in Figure 4.2 confirms the accuracy of this calculation. It also shows the uniform particle size distribution. In order to maximize the absorption of visible light a balance was struck between growing the largest dots possible without sacrificing a uniform particle size distribution. This narrow particle size distribution ensures all quantum dots possess the same electronic characteristics.

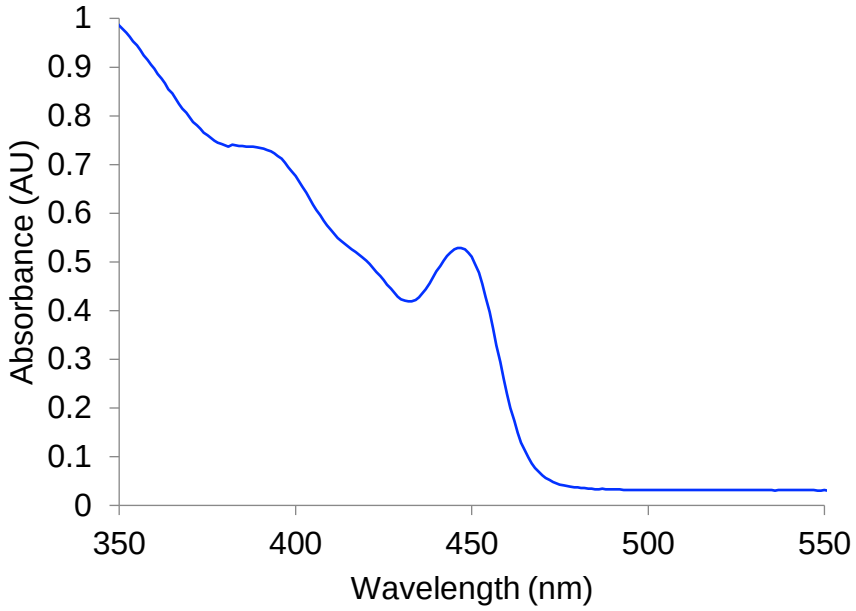

Figure 4.1. UV-vis spectra of colloidal CdS quantum dots with a peak absorption at 448nm.

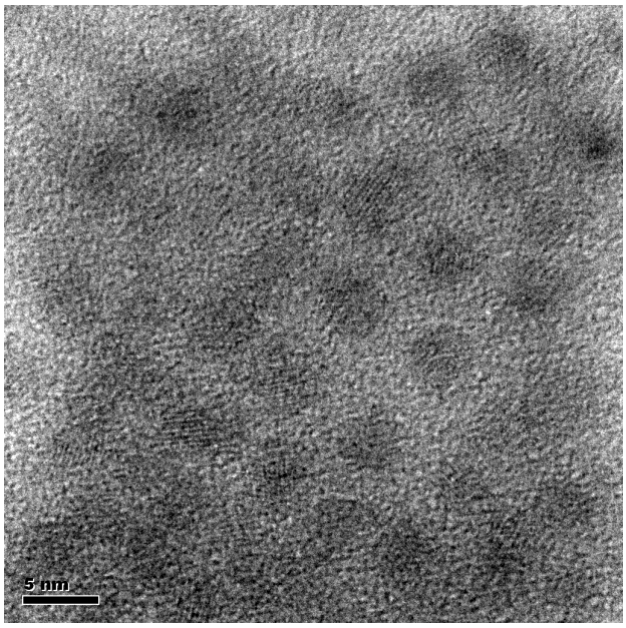

Figure 4.2. 300 keV Transmission electron microscope image of CdS quantum dots.

Films were fabricated via spin-coating the CdS QDs onto conductive fluorine doped tin oxide (FTO) glass slides. The spin coating was done while rotating the FTO slide at a speed of 2000 revolutions per minute (rpm). Spinning rates higher than 2000 rpm result in lower absorbance indicative of less adhesion of QDs to the FTO surface. A comparison of the UV-visible spectra of the CdS QD film with the solution shows a slight difference in the spectra as illustrated in Figure 4.3. The increase in the baseline comes as a result of the absorption from the FTO slide. The slight redshift in the band edge and a small change to the band structure, come as a result of changes in the organic capping ligands on the nanocrystal surface as documented in the literature.[31] The substitution of some oleic acid capping ligands with ethanedithiol effectively increases the radius of the QD slightly by adding extra sulfur surface sites resulting in a redshift of the band edge. This was confirmed by measuring the UV-vis of a QD solution to which ethanedithiol was added resulting in a band edge absorption (Figure 4.4) consistent with the redshift observed between QDs in solution and film form (Figure 4.3).

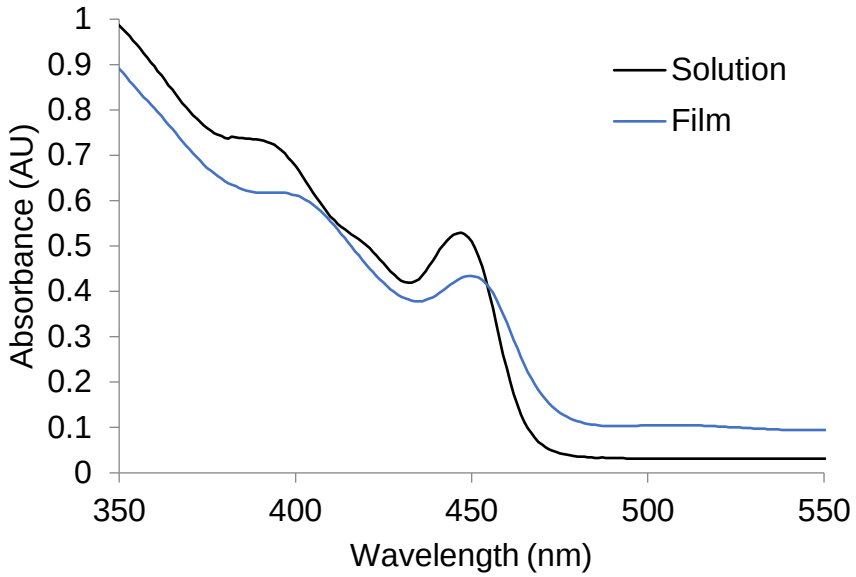

Figure 4.3. Comparison of the solution spectra (blue) and film bound (red) CdS quantum dots.

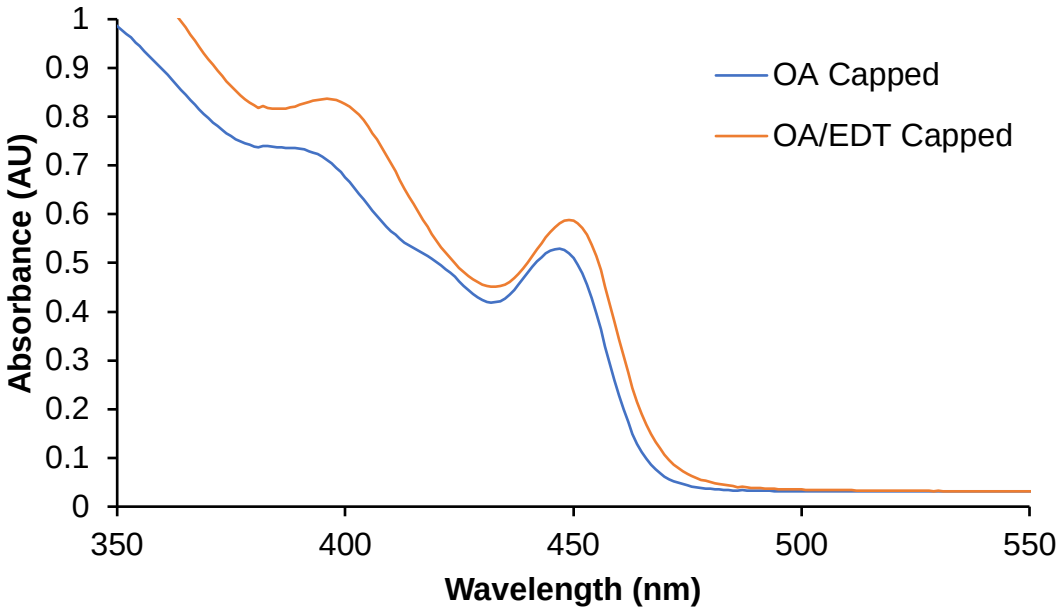

Figure 4.4. UV-vis spectra of CdS QDs with oleic acid as the capping ligand (blue) and a mixture of oleic and and ethanedithiol (red). The mixed ligand nanoparticles were generated by adding a 5% (v/v) ethanedithiol acetonitrile solution to colloidal CdS QDs capped with oleic acid.

Prior to protecting the QD films with a thin layer of metal oxide, a proof of concept experiment was carried out to demonstrate the viability of immobilizing a POM WOC on metal oxide surfaces via electrostatic attraction. Powdered TiO_2 nanoparticles were added to a solution of the robust POM WOC, $[\{Ru^{IV}_4(OH)_2(H_2O)_4\}(\gamma\text{-}SiW_{10}O_{34})_2]^{10-}$, at pH 3.3. This pH is below the TiO_2 PZC (pH = 5.6), thus the surface is protonated and positively charged. The positively charged surface should consequently bind the highly anionic POM. Figure 4.5 shows a comparison of filtered TiO_2 particles from solutions adjusted pH 3.3 and 7. The darker brown color on the filter paper from the pH 3.3 solution qualitatively confirms that the POM is electrostatically bound to the TiO_2 surface when the pH is below the PZC. The TiO_2 particles with the attached POM were then washed with a pH 7 solution, which is above the PZC of TiO_2,

and the POMs as predicted, to go back into solution. This demonstrates the reversible nature of the binding depending on the pH of the solution.

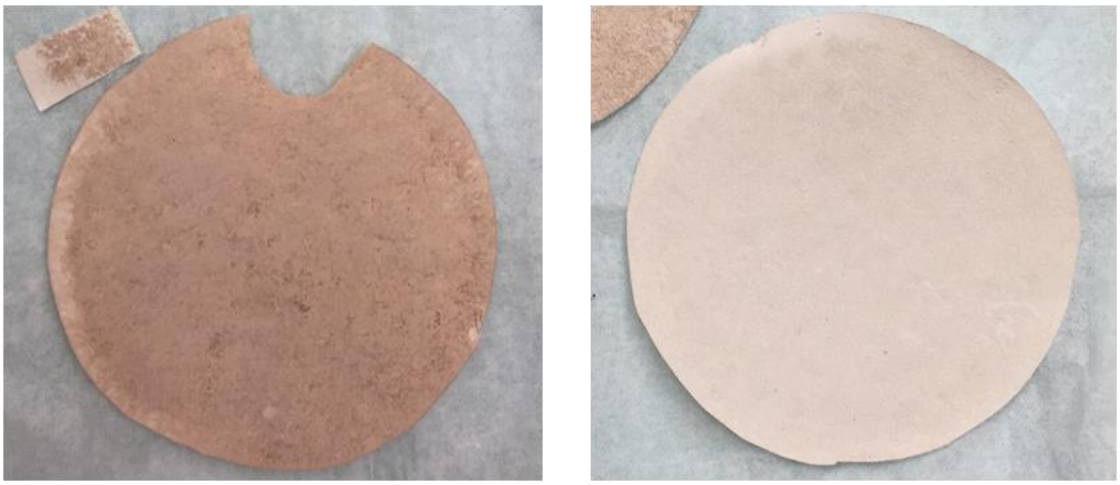

Figure 4.5. Powdered TiO_2 nanoparticles exposed to the POM WOC, $Rb_8K_2[\{Ru_4(OH)_2(H_2O)_4\}(\gamma\text{-}SiW_{10}O_{34})_2]$, at pH 3.3 (left) and pH 7 (right). The darker brown color on the left results from the electrostatic binding the POM at pH values below the PZC of TiO_2 which is 5.6.

Having successfully demonstrated the ability to bind POM WOCs on TiO_2, along with the fabrication of CdS QD films, atomic layer deposition was used to create a conformal metal oxide coating on the surface to protect the CdS QDs from photocorrosion. Initial samples were sent to Boston College where they were coated with 2nm, 10nm, and 50nm of TiO_2 at 275°C. The coating thickness for each film was determined by ellipsometry on silicon wafers placed in the ALD reactor with the films. Visual inspection of the films, confirmed by UV-vis, immediately showed that the coating had damaged the films and shifted the band edge absorption. The films, now

much darker in color and showed a much broader band edge shown in Figure 4.6. At 275°C where the temperature is high enough to produce crystalline TiO_2,[32] unfortunately, it is also high

enough to cause the CdS nanocrytals to begin merging into bulk CdS. A second set of films was coated with amorphous TiO_2 at 150 °C shown in Figure 4.7. Under these conditions the temperature was low enough to coat the QDs while keeping the band structure intact.

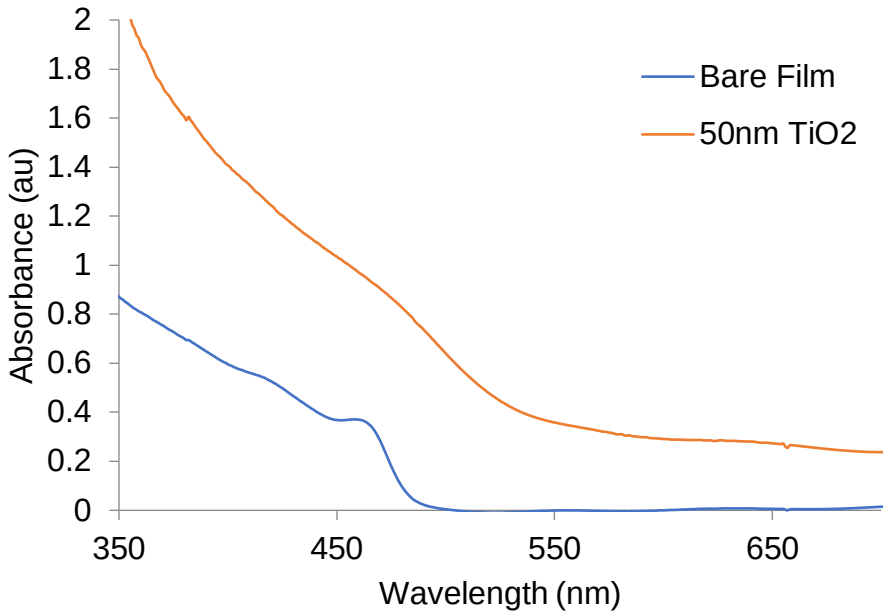

Figure 4.6. Before and after comparison of a CdS QD film subjected to high temperature (275 °C) TiO_2 ALD.

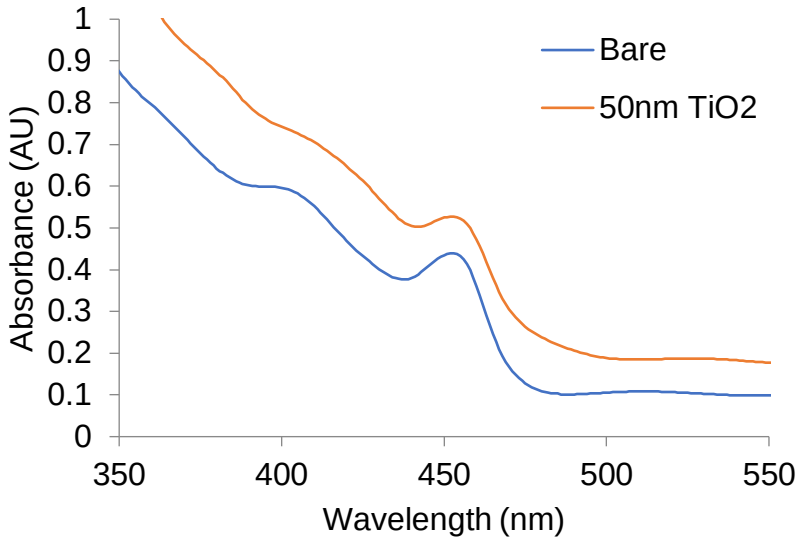

Figure 4.7. Before and after comparison of a CdS QD film subjected to low temperature (150 °C) TiO_2 ALD.

The coated films were then converted into electrodes and subjected to electrochemical experiments to assess their stability and photoelectrochemical performance. Cyclic voltammograms (CV) were run from the open circuit potential out to 1.49 V vs. RHE in pH 8.5 borate buffer. This value was chosen as it is significantly above the 1.23V required for water oxidation. The CV scans of the films show that the film with a 50nm coating of TiO_2 is stabilized and does not change over time whereas the films with thinner coatings degrade over time resulting in irreversible scans (Figure 4.8). This conclusion is also supported by a stable photocurrent present in the 50nm-coated film in contrast to photocurrents that decrease over time for the films with no coatings (Figure 4.9). Following the electrochemical experiments UV-visible spectra were taken providing additional evidence for the stability or the lack thereof by monitoring changes in absorption and the shape of the QD band edge (Figures 4.10). While the thickest coating best stabilized the QD films, it also acted as a barrier for hole transfer to the

surface which resulted in the lowest photocurrent when using sodium sulfite as a hole scavenger (Figure 4.11).

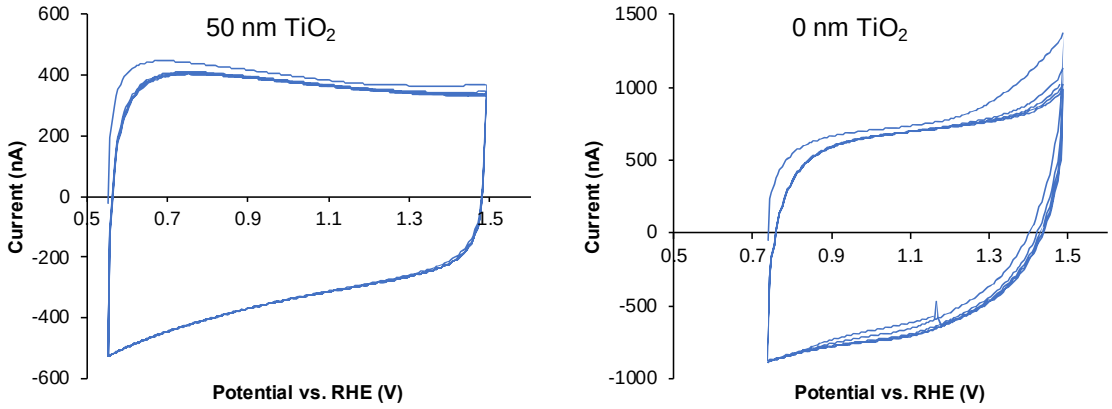

Figure 4.8. Cyclic voltammograms (CVs) of CdS QD films with and without a 50 nm TiO_2 coating. Conditions: 0.1M sodium borate buffer, pH 8.5, 0.5M Na_2SO_4, 405 nm LED light source, potential varied from OCP to 1.49 V vs. RHE.

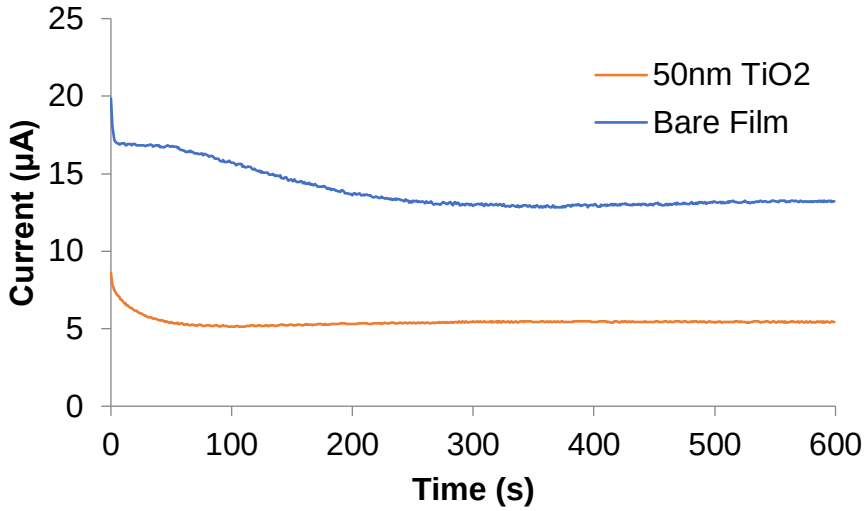

Figure 4.9. Photocurrents generated during bulk electrolysis showing that the 50nm coated film (red) is more stable than the uncoated film (blue). Conditions: 0.1M sodium borate buffer, pH 8.5, 0.5M Na_2SO_4, 405 nm LED light source, potential held at 1.49 V vs. RHE.

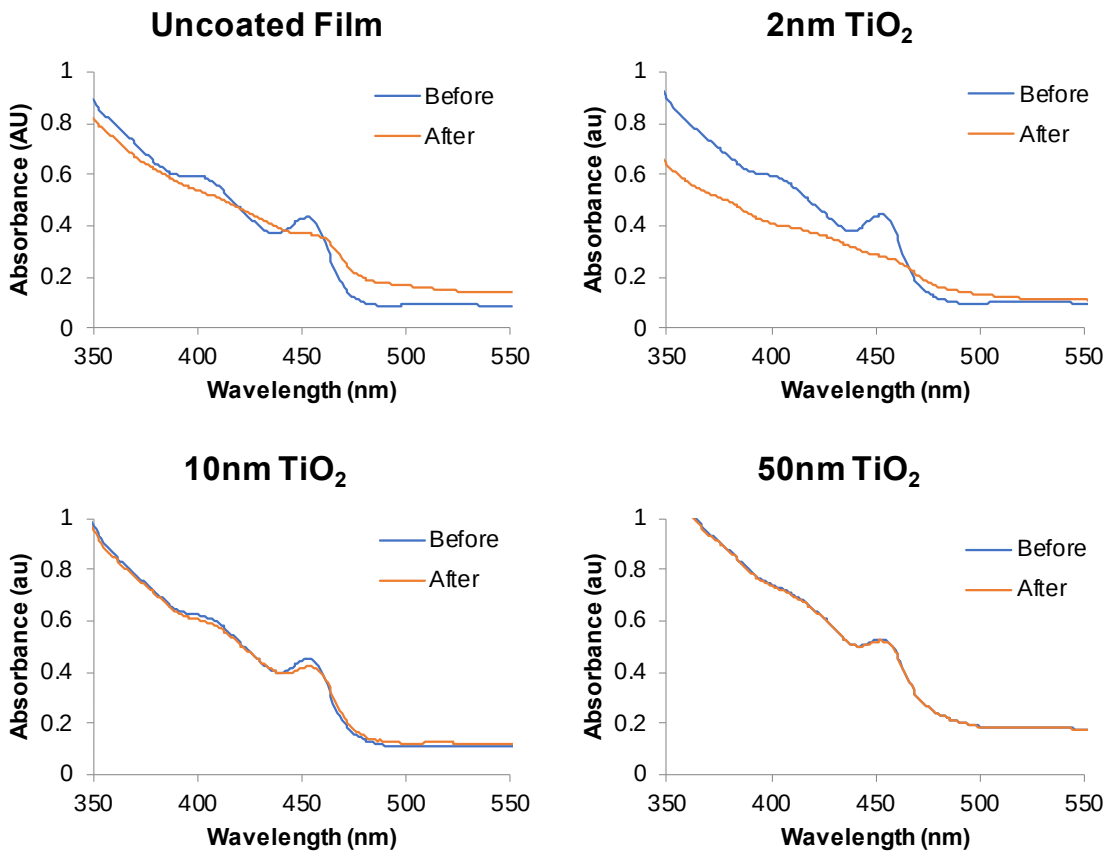

Figure 4.10. UV-vis spectra of CdS QD films with ALD TiO_2 coatings of varying thicknesses before (blue) and after (orange) 10-minute bulk electrolysis stability studies. Bulk electrolysis conditions: 0.1M sodium borate buffer, pH 8.5, 0.5M Na_2SO_4, 405 nm LED light source, potential held at 1.49 V vs. RHE.

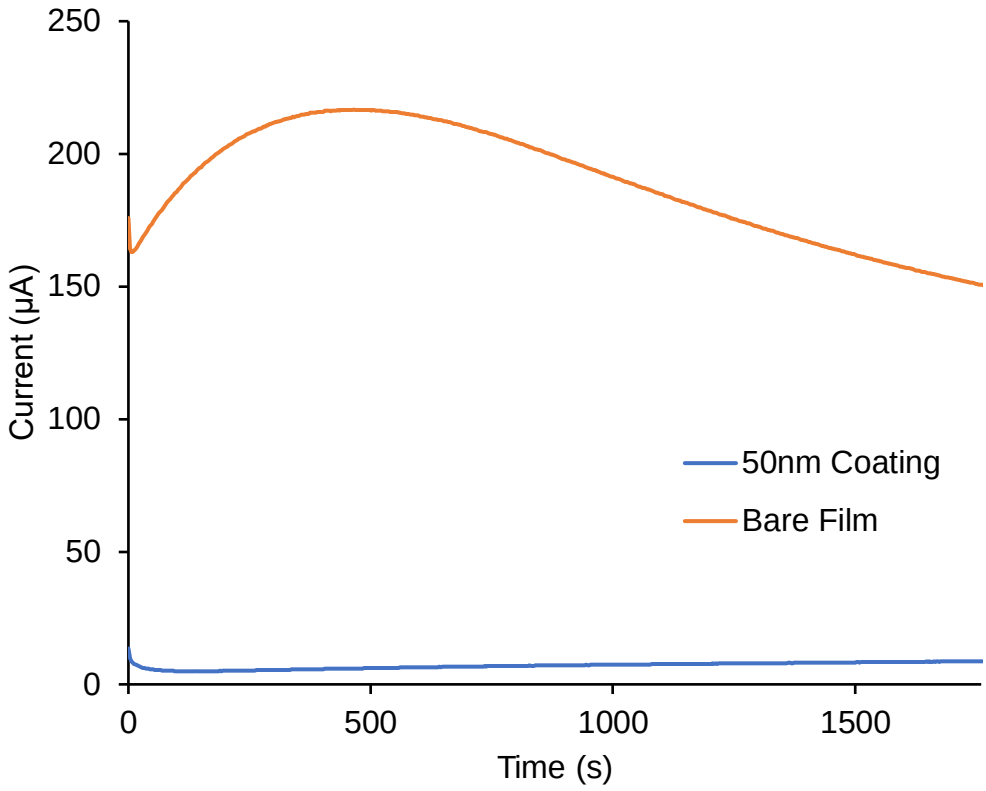

Figure 4.11. Bulk electrolysis of coated (blue: 50 nm TiO_2) and uncoated (red) CdS QD films. Conditions: 0.1M sodium borate buffer, pH 8.5, 0.5M Na_2SO_4, 0.1M Na_2SO_3, 405 nm LED light source, potential held at 1.49 V vs. RHE.

The same experiments were carried out using ALD coatings of Al_2O_3 and zinc ZnO instead of TiO_2. Similar trends were observed where the thickest coatings were the most stabilizing as monitored by UV-vis (Figures 4.12 and 4.13), but also created the largest resistance to hole transfer. In agreement with literature findings,[33] ZnO appeared to be the most conductive of the metal oxides based on the average photocurrent generated on films coated with 50nm of metal oxide during a 10-minute period of bulk electrolysis. However, unlike the case of TiO_2 where the photocurrent was stable, the photocurrent generated from the ZnO-coated film continued to decrease throughout the measurement (Figure 4.14). This suggests that while the

QDs were protected from photocorrosion, the surface of the film is still changing. As a result, it likely that some of the observed photocurrent originates from some sort of parasitic pathway.

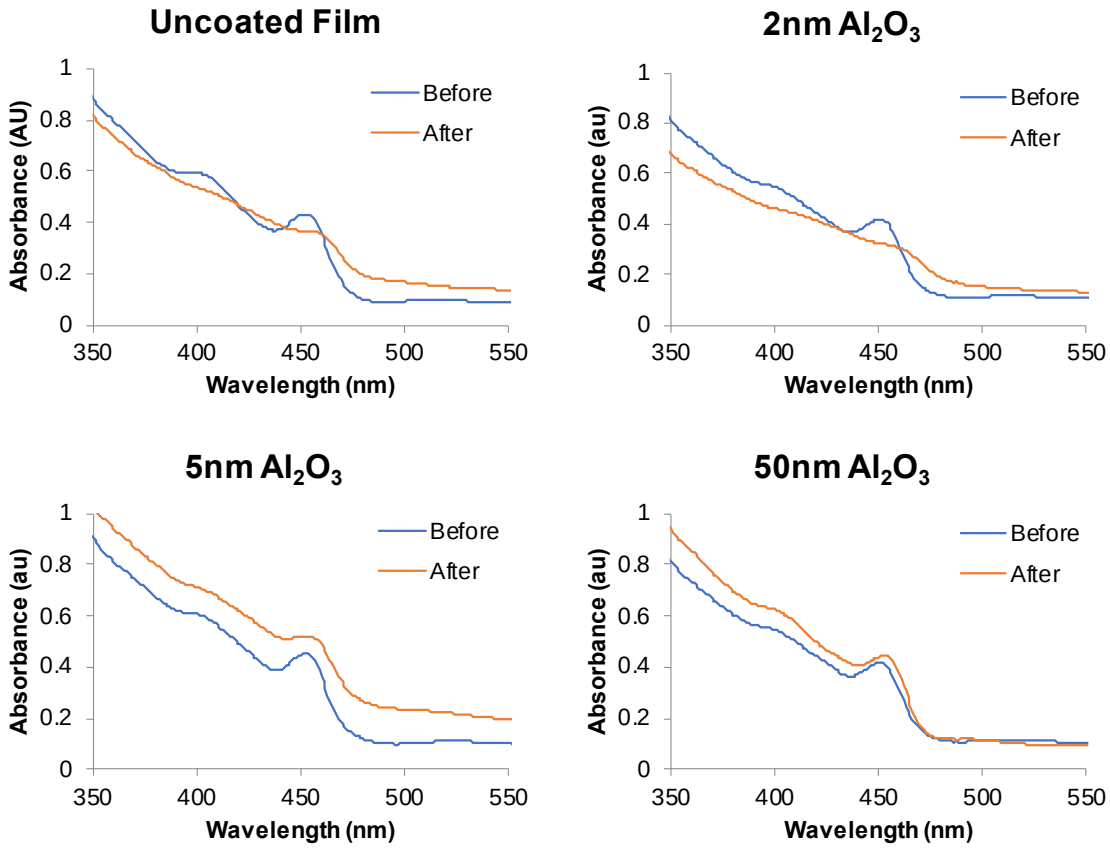

Figure 4.12. UV-vis spectra of CdS QD films with ALD Al_2O_3 coatings of varying thicknesses before (blue) and after (orange) 10-minute bulk electrolysis stability studies. Bulk electrolysis conditions: 0.1M sodium borate buffer, pH 8.5, 0.5M Na_2SO_4, 405 nm LED light source, potential held at 1.49 V vs. RHE.

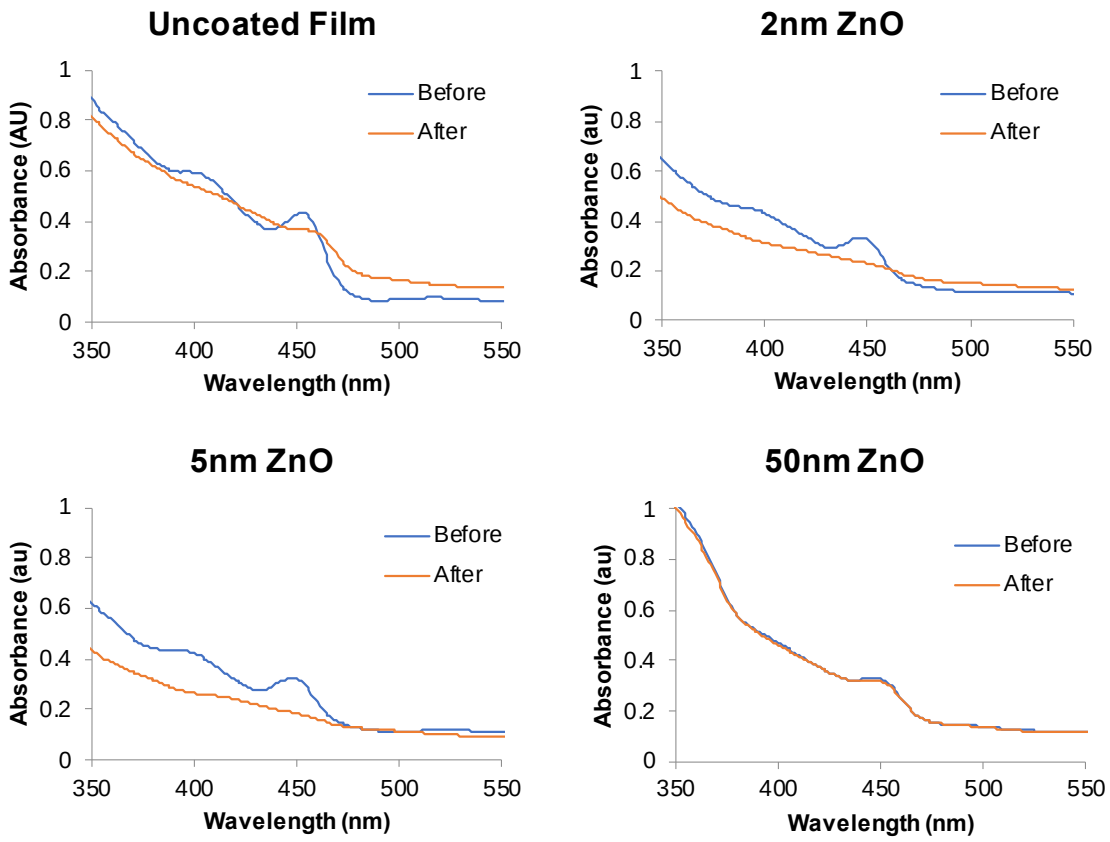

Figure 4.13. UV-vis spectra of CdS QD films with ALD ZnO coatings of varying thicknesses before (blue) and after (orange) 10-minute bulk electrolysis stability studies. Bulk electrolysis conditions: 0.1M sodium borate buffer, pH 8.5, 0.5M Na_2SO_4, 405 nm LED light source, potential held at 1.49 V vs. RHE.

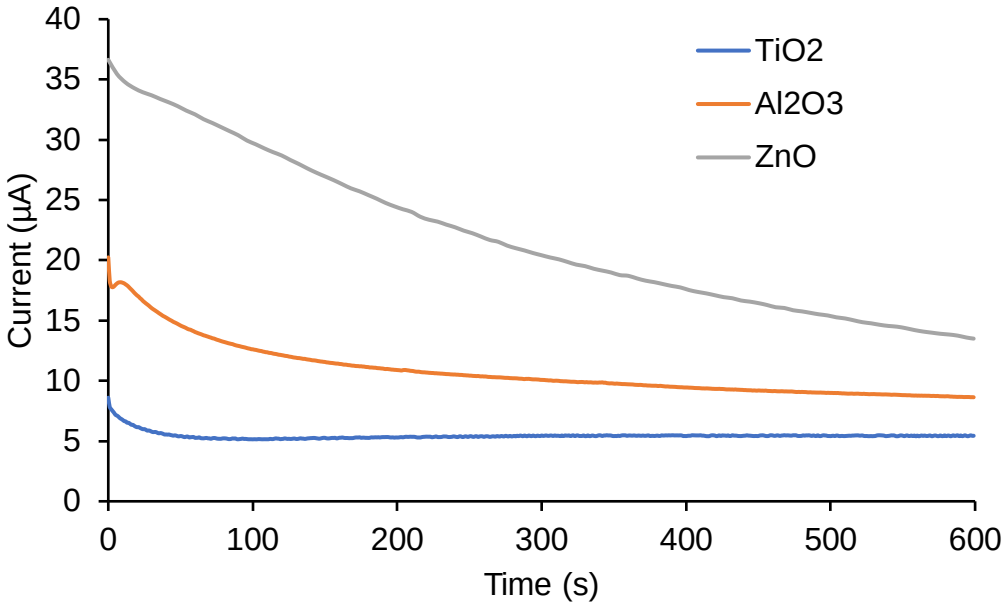

Figure 4.14. Bulk electrolysis stability studies of CdS QD films coated with 50 nm of TiO_2 (blue), Al_2O_3 (red), and ZnO (green). Conditions: 0.1M sodium borate buffer, pH 8.5, 0.5M Na_2SO_4, 405 nm LED light source, potential held at 1.49 V vs. RHE for 10 minutes.

4.4 Conclusion

The primary conclusion to be drawn at this stage is that atomic layer deposition (ALD) of at least 50 nm of metal oxide stabilizes cadmium sulfide quantum dot films against photocorrosion. In addition, the ALD procedure must be conducted at lower temperatures, such as 150 °C, as the CdS QDs in the film will be converted to bulk CdS at higher temperatures. The other major conclusion is that by adjusting the pH to below the PZC, POMs will electrostatically bind to protonated, and thus positively charged, metal oxide surfaces. While this study successfully demonstrates protection against photocorrosion, the thick metal oxide layer significantly inhibits electron transfer. As a result, the success limiting factor lies with improving carrier mobility within this layer or utilizing a more robust semiconductor light-absorber. Building off of these results, and the new collaborations to conduct atomic layer

deposition, a separate study examined the use of ALD to immobilize $Rb_8K_2[\{Ru_4(OH)_2(H_2O)_4\}(\gamma\text{-}SiW_{10}O_{34})_2]$ on the surface of hematite. This system proved efficient for water oxidation and is published in *ACS Applied Materials & Interfaces*.[34]

4.5 References

1. Lewis, N. S.; Nocera, D. G., Powering the planet: Chemical challenges in solar energy utilization. *Proc. Natl. Acad. Sci. U. S. A.* **2006,** *103* (43), 15729-15735.

2. *Key World Energy Statistics*; International Energy Agency: Paris, 2014.

3. Earth's CO_2 Home Page. https://www.co2.earth/ (accessed September 29, 2020).

4. Petit, J. R.; Jouzel, J.; Raynaud, D.; Barkov, N. I.; Barnola, J. M.; Basile, I.; Bender, M.; Chappellaz, J.; Davis, M.; Delaygue, G.; Delmotte, M.; Kotlyakov, V. M.; Legrand, M.; Lipenkov, V. Y.; Lorius, C.; Pepin, L.; Ritz, C.; Saltzman, E.; Stievenard, M., Climate and atmospheric history of the past 420,000 years from the Vostok ice core, Antarctica. *Nature* **1999,** *399* (6735), 429-436.

5. Hambourger, M.; Moore, G. F.; Kramer, D. M.; Gust, D.; Moore, A. L.; Moore, T. A., Biology and technology for photochemical fuel production. *Chem. Soc. Rev.* **2009,** *38* (1), 25-35.

6. Gregg, B. A.; Hanna, M. C., Comparing organic to inorganic photovoltaic cells: Theory, experiment, and simulation. *J. Appl. Phys.* **2003,** *93* (6), 3605-3614.

7. Kalogirou, S. A., Solar thermal collectors and applications. *Progr. Energy Combust. Sci.* **2004,** *30* (3), 231-295.

8. Buick, R., When did oxygenic photosynthesis evolve? *Philosophical Transactions of the Royal Society of London B: Biological Sciences* **2008,** *363* (1504), 2731-2743.

9. Gratzel, M., Photoelectrochemical cells. *Nature* **2001,** *414* (6861), 338-344.

10. Swierk, J. R.; Mallouk, T. E., Design and development of photoanodes for water-splitting dye-sensitized photoelectrochemical cells. *Chem. Soc. Rev.* **2013,** *42* (6), 2357-2387.

11. Verlage, E.; Hu, S.; Liu, R.; Jones, R. J. R.; Sun, K.; Xiang, C.; Lewis, N. S.; Atwater, H. A., A monolithically integrated, intrinsically safe, 10% efficient, solar-driven water-splitting system based on active, stable earth-abundant electrocatalysts in conjunction with tandem III-V light absorbers protected by amorphous TiO2 films. *Energy & Environmental Science* **2015,** *8* (11), 3166-3172.

12. Lichterman, M. F.; Carim, A. I.; McDowell, M. T.; Hu, S.; Gray, H. B.; Brunschwig, B. S.; Lewis, N. S., Stabilization of n-cadmium telluride photoanodes for water oxidation to O2(g) in aqueous alkaline electrolytes using amorphous TiO2 films formed by atomic-layer deposition. *Energy & Environmental Science* **2014,** *7* (10), 3334-3337.

13. Hu, S.; Shaner, M. R.; Beardslee, J. A.; Lichterman, M.; Brunschwig, B. S.; Lewis, N. S., Amorphous TiO_2 coatings stabilize Si, GaAs, and GaP photoanodes for efficient water oxidation. *Science* **2014,** *344* (6187), 1005-1009.

14. Kim, D. H.; Losego, M. D.; Hanson, K.; Alibabaei, L.; Lee, K.; Meyer, T. J.; Parsons, G. N., Stabilizing chromophore binding on TiO_2 for long-term stability of dye-sensitized solar cells using multicomponent atomic layer deposition. *Phys. Chem. Chem. Phys.* **2014,** *16* (18), 8615-8622.

15. Hanson, K.; Losego, M. D.; Kalanyan, B.; Parsons, G. N.; Meyer, T. J., Stabilizing Small Molecules on Metal Oxide Surfaces Using Atomic Layer Deposition. *Nano Lett.* **2013,** *13* (10), 4802-4809.

16. Hanson, K.; Losego, M. D.; Kalanyan, B.; Ashford, D. L.; Parsons, G. N.; Meyer, T. J., Stabilization of $[Ru(bpy)_2(4,4'-(PO_3H_2)bpy)]^{2+}$ on Mesoporous TiO_2 with Atomic Layer Deposition of Al2O3. *Chem. Mater.* **2012,** *25* (1), 3-5.

17. Geletii, Y. V.; Botar, B.; Kögerler, P.; Hillesheim, D. A.; Musaev, D. G.; Hill, C. L., An All-Inorganic, Stable, and Highly Active Tetraruthenium Homogeneous Catalyst for Water Oxidation. *Angew. Chem. Int. Ed.* **2008,** *47* (21), 3896-3899.

18. Yin, Q.; Tan, J. M.; Besson, C.; Geletii, Y. V.; Musaev, D. G.; Kuznetsov, A. E.; Luo, Z.; Hardcastle, K. I.; Hill, C. L., A Fast Soluble Carbon-Free Molecular Water Oxidation Catalyst Based on Abundant Metals. *Science* **2010,** *328* (5976), 342-345.

19. Vickers, J. W.; Lv, H.; Sumliner, J. M.; Zhu, G.; Luo, Z.; Musaev, D. G.; Geletii, Y. V.; Hill, C. L., Differentiating Homogeneous and Heterogeneous Water Oxidation Catalysis: Confirmation that $[Co_4(H_2O)_2(\alpha\text{-}PW_9O_{34})_2]^{10-}$ Is a Molecular Water Oxidation Catalyst. *J. Am. Chem. Soc.* **2013,** *135* (38), 14110-14118.

20. Lv, H.; Song, J.; Geletii, Y. V.; Vickers, J. W.; Sumliner, J. M.; Musaev, D. G.; Kögerler, P.; Zhuk, P. F.; Bacsa, J.; Zhu, G.; Hill, C. L., An Exceptionally Fast Homogeneous Carbon-Free Cobalt-Based Water Oxidation Catalyst. *J. Am. Chem. Soc.* **2014,** *136* (26), 9268-9271.

21. Lv, H.; Geletii, Y. V.; Zhao, C.; Vickers, J. W.; Zhu, G.; Luo, Z.; Song, J.; Lian, T.; Musaev, D. G.; Hill, C. L., Polyoxometalate water oxidation catalysts and the production of green fuel. *Chem. Soc. Rev.* **2012,** *41* (22), 7572-7589.

22. Sartorel, A.; Carraro, M.; Scorrano, G.; Zorzi, R. D.; Geremia, S.; McDaniel, N. D.; Bernhard, S.; Bonchio, M., Polyoxometalate Embedding of a Tetraruthenium(IV)-oxo-core by

Template-Directed Metalation of $[\gamma\text{-}SiW_{10}O_{36}]^{8-}$: A Totally Inorganic Oxygen-Evolving Catalyst. *J. Am. Chem. Soc.* **2008,** *130* (15), 5006-5007.

23. Blasco-Ahicart, M.; Soriano-López, J.; Carbó, J. J.; Poblet, J. M.; Galan-Mascaros, J. R., Polyoxometalate electrocatalysts based on earth-abundant metals for efficient water oxidation in acidic media. *Nature Chem.* **2018,** *10* (1), 24-30.

24. Okun, N. M.; Anderson, T. M.; Hill, C. L., $[(Fe^{III}(OH_2)_2)_3(A\text{-}\alpha\text{-}PW_9O_{34})_2]^{9-}$ on Cationic Silica Nanoparticles, a New Type of Material and Efficient Heterogeneous Catalyst for Aerobic Oxidations. *J. Am. Chem. Soc.* **2003,** *125* (11), 3194-3195.

25. Lauinger, S. M.; Sumliner, J. M.; Yin, Q.; Xu, Z.; Liang, G.; Glass, E. N.; Lian, T.; Hill, C. L., High Stability of Immobilized Polyoxometalates on TiO2 Nanoparticles and Nanoporous Films for Robust, Light-Induced Water Oxidation. *Chem. Mater.* **2015,** *27* (17), 5886-5891.

26. Fielden, J.; Sumliner, J. M.; Han, N.; Geletii, Y. V.; Xiang, X.; Musaev, D. G.; Lian, T.; Hill, C. L., Water splitting with polyoxometalate-treated photoanodes: enhancing performance through sensitizer design. *Chem. Sci.* **2015,** *6* (10), 5531-5543.

27. Kosmulski, M., The significance of the difference in the point of zero charge between rutile and anatase. *Adv. Colloid Interface Sci.* **2002,** *99* (3), 255-264.

28. Kamat, P. V., Quantum Dot Solar Cells. Semiconductor Nanocrystals as Light Harvesters†. *J. Phys. Chem. C* **2008,** *112* (48), 18737-18753.

29. Yu, W. W.; Peng, X., Formation of High-Quality CdS and Other II–VI Semiconductor Nanocrystals in Noncoordinating Solvents: Tunable Reactivity of Monomers. *Angew. Chem. Int. Ed.* **2002,** *41* (13), 2368-2371.

30. Yu, W. W.; Qu, L.; Guo, W.; Peng, X., Experimental Determination of the Extinction Coefficient of CdTe, CdSe, and CdS Nanocrystals. *Chem. Mater.* **2003,** *15* (14), 2854-2860.

31. Newton, J. C.; Ramasamy, K.; Mandal, M.; Joshi, G. K.; Kumbhar, A.; Sardar, R., Low-Temperature Synthesis of Magic-Sized CdSe Nanoclusters: Influence of Ligands on Nanocluster Growth and Photophysical Properties. *J. Phys. Chem. C* **2012,** *116* (7), 4380-4389.

32. Ponraj, J. S.; Attolini, G.; Bosi, M., Review on Atomic Layer Deposition and Applications of Oxide Thin Films. *Crit. Rev. Solid State Mater. Sci.* **2013,** *38* (3), 203-233.

33. Liu, Y.; Gibbs, M.; Perkins, C. L.; Tolentino, J.; Zarghami, M. H.; Bustamante, J.; Law, M., Robust, Functional Nanocrystal Solids by Infilling with Atomic Layer Deposition. *Nano Lett.* **2011,** *11* (12), 5349-5355.

34. Lauinger, S. M.; Piercy, B. D.; Li, W.; Yin, Q.; Collins-Wildman, D. L.; Glass, E. N.; Losego, M. D.; Wang, D.; Geletii, Y. V.; Hill, C. L., Stabilization of Polyoxometalate Water Oxidation Catalysts on Hematite by Atomic Layer Deposition. *ACS Appl. Mater. Interfaces* **2017,** *9* (40), 35048-35056.